POLITEKNIK NEGERI BALI

Journal of Engineering Design and Technology

logic

Vol. 24 No. 2 July 2024

p-ISSN. 1412-114X

e-ISSN. 2580-5649

LOGIC

Jurnal Rancang Bangun dan Teknologi

LOGIC
Journal of Engineering Design and Technology
Vol. 24 No.2 July 2024 ; p. 39-48

p-ISSN : 1412-114X
e-ISSN : 2580-5649
http://ojs2.pnb.ac.id/index.php/LOGIC

EFFECT OF STATIC THERMAL TENSIONING AND PREHEATING ON ANGULAR DISTORTION IN FCAW WELDED SS400 STEEL CORNER JOINTS

1,2,3,4,5,6) Department of Mechanical Engineering, Politeknik Negeri Malang, Jalan Soekarno-Hatta No 9, Jatimulyo, Lowokwaru, Malang, Indonesia

Correponding email 1)* :
Sugeng.hadi@polinema.ac.id

Sugeng Hadi Susilo 1)* , Eko Yudiyanto2), Agus Setiawan3), Khambali4), Suyanto5), Falih Alauddin6)

Abstract.
FCAW welding is an automated welding process that uses wire-wound electrodes to melt metal, using flux or powder inside the electrode core for protection. Common problems in FCAW welding are angular distortion and changes in length and width dimensions, especially in thin plate iron materials, due to residual stress from the welding process.

This research aims to examine the impact of static thermal stress, preheating, and their combination on corner distortion in SS400 steel corner joints during FCAW welding, taking into account the heat input during welding. An actual experimental research methodology was used, with varying preheating temperatures of 200°C, 250°C, 300°C, static thermal stress at 150°C, 200°C, 250°C, transient thermal stress at 150°C, 200° C, 250 °C, and an untreated reference method to determine the welding approach that minimizes corner distortion. The material used is 3mm thick SS400 steel.

The research results show that there is a significant influence of static thermal stress, preheating, and a combination of both on corner distortion. The optimal welding methods identified are preheating static thermal stress at 89°55', preheating transient thermal stress at 89°50', static thermal stress at 150°C at 89°45', transient thermal stress at 150°C at 89 '. °40', and preheating at 200°C at 89°35'.

Keywords : Angular Distortion, SS400 Steel, FCAW Welding

1. INTRODUCTION

Manufacturing requires welding to combine parts and construct structures. Metals can be joined locally with arc welding's high heat. Conduction cools a base metal after moving a molten wire to it in the consumable electrode method. Shrinkage owing to heat strain induces partial transition into tensile plastic strain in unbounded areas. This causes persistent deformation in the base material because compressive plastic strain during heating exceeds tensile strain during cooling. Uneven shrinkage and greater lattice spacing leave residual tensile stresses. Compressive stress remains in the surrounding environment [1]. Residual tensile stress affects fatigue life, stress corrosion cracking, weld cracking, and bending strength [2].

Welding distortions cause geometric misalignments and gaps between structures, which complicate assembly and reduce manufacturing quality and productivity. Due to their thickness, offshore platform and ship hull legs, nodes, major frames, and girders are multi-layer welded to handle enormous stresses. As a geometric flaw, welding's initial distortion might impair bending strength under compressive force. We know initial deflection reduces bending strength. Similar to the shear line formula with eccentric loading, the initial curvature in the deflection affects bending strength [3]. Welding distortion prediction and control are crucial.

Based on this notion, DNV GL standards [4] set structural design alignment and straightness tolerances. Product design and manufacturing in shipbuilding and heavy industries follow these guidelines to prevent buckling tragedies. In additive manufacturing (AM), multi-layer deposition has caused thermal deformation concerns as well as conventional industries. In AM parts, thermal deformation produces dimensional inaccuracies, and prediction equations developed from measured strain data advise changing laser power, layer thickness, and scanning speed to reduce thermal strain [5].

Clamping force matters most in thermal deformation, which is affected by material qualities, temperature, and cross-sectional area [6]. With layer deposition, displacement increased proportionately. Uneven thickness-direction transverse shrinkage distorts the welding angle in one pass [7]. This distortion depends on weld deposition, thickness temperature gradient, and limitations. The direction and amount of the angular distortion depend on the bead cross-sectional profile asymmetry, according to laser welding studies and theoretical models [8]. Cross-sectional bead deposition vary with methods and circumstances. Weld material, plastic strain distribution, and holes also affect angular distortion. Fluid flow deposited at groove joints, radiation, and convection cooling conditions, and material thermal characteristics determine temperature dispersion.

Temperature gradients dominate corner distortion in fillet welding simulations [9]. According to [10], the beginning temperature affects the thickness temperature gradient by angular distortion. Pre- and post-heating treatments affected temperature distribution, residual strains, and distortion [11]. Due to high-temperature stiffness loss, early setup and installation conditions dictate distortion. Many foundational studies have examined welding distortion in different situations and materials.

When penetration is less than 0.6 times thickness, [12] discovered that the angular distortion of bead-on-plate welding is linearly linked to heat input (H) to the square of thickness (t). As penetration rises, the non-fusion zone below the fusion zone becomes plastic owing to temperature increase and is difficult to use as a rotation point for bending.

Numerous tests examined how heat input, plate thickness, and materials affect deformation [13]. This formula predicts welding distortion using heat flow and thermal elastoplast theory. According to studies, welding distortion in the same material depends on H/t^2 (heat input divided by thickness squared). Regardless of the welding technique, mild steel distortion is proportionate to H/t^2 when H/t^2 is less than 2500 cal/cm^3.

Thermal elastoplasts' intrinsic strain mechanism was used to create an elastic model [14]. Their database shows that transverse angular distortion rises until H/t^2 reaches 10 kJ/mm^3 and then falls to 40. Deformation depends on heat and thickness. Angular distortion increases with heat input and decreases with thickness squared after a maximum. Since molten wire fills the groove between the plates, the number of passes depends on the metal deposit per length. The physics of arc welding has also been used to study wire melting.

Calculations determined SAW bead dimensions [15]. Travel speed and nozzle-to-plate distance decreased bead area, whereas wire feed rate and arc voltage increased HAZ. Wire feed rate increases bead size, whereas arc voltage widens but reduces penetration and gain. Weld bead size prediction methodology for 409 M stainless steel gas metal arc welding (GMAW) employing central composite rotating design [16]. During welding, current increased penetration, width, reinforcement, and thinning, while speed decreased bead dimensions and arc voltage increased all but reinforcement. SAW matches FCAW. Explored welding variables and bead shape/HAZ width [17]. Speed reduces weld metal cross-sectional area and HAZ width.

Response surface regression was used to estimate FCAW 317L cladding weld form [18]. Our welding current increases penetration, bead size, and area. Electric current dominates bead size because resistance melts electrode wire [19, 20]. Bead form and welding process factors affected fatigue life [21]. The bead aspect ratio between maximum height and joint width fluctuates with heat input, impacting fatigue life.

2. METHODS

Using SS 400 steel with a thickness of 3 mm. The welding machine used is an OTC brand FCAW welding machine, Japanese inventor model, with a current setting of 120 A, voltage 25 volts, straight polarity, AWS E71T1 electrode with a diameter of 1.2 mm, flat position and corner joint welding type.

2.1 Welding Process

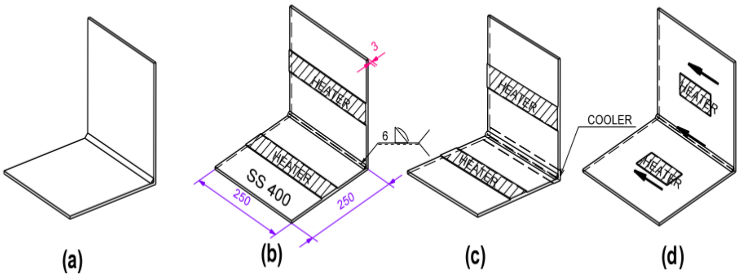

Figure 1 Welding Method

Description
(a) Without treatment
(b) Preheating
(c) Static Thermal Tensioning
(d) Transient Thermal Tensioning

2.1.1 Welding Process Without Treatment

This welding process aims to determine the initial results of distortion data whether later after the welding process with various methods can minimize the occurrence of distortion or increase the amount of distortion. Welding is done without additional heating in the base metal.

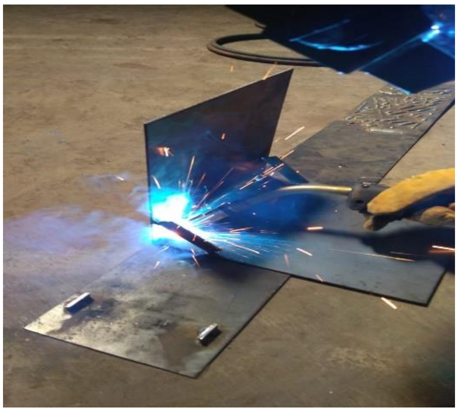

Figure 2 Welding process without treatment

The results of distortion measurements using a universal bevel protractor can be seen in Figure 3.

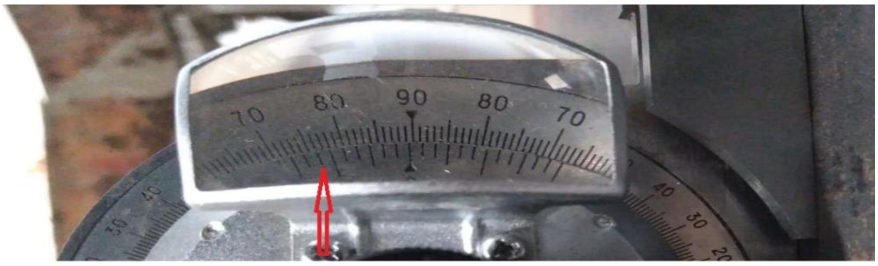

Figure 3 Distortion measurement results of the welding method without treatment

2.1.2 Preheating Process

Welding with preheating is carried out before the welding process, the heating is directed evenly in the base metal to be welded with the aim of minimizing angular distortion with heating temperature variations of 200°, 250° and 300°. Heating is done with an additional heating device in the form of oxy gas. The measurement results with the universal bevel protractor are as shown in Figure 4.

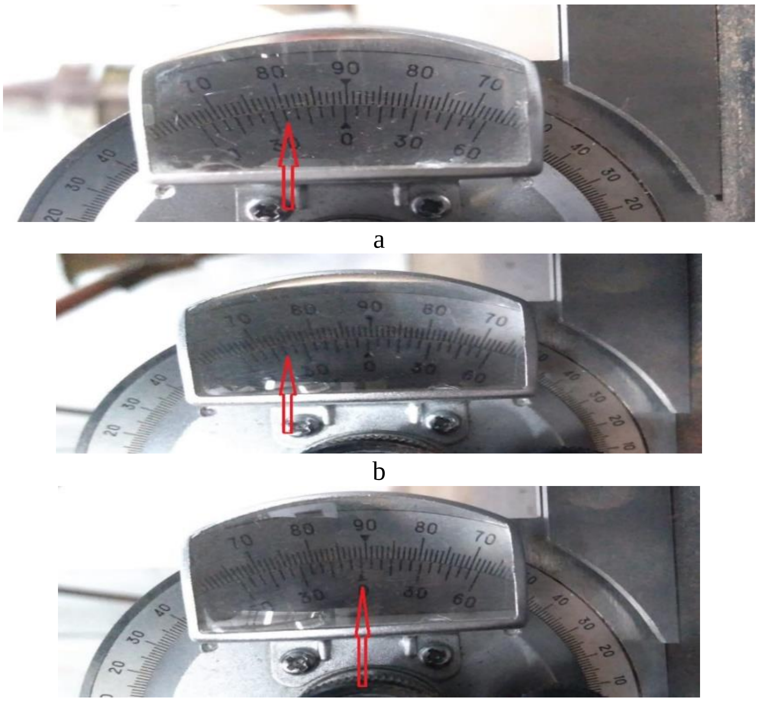

a

b

c

Figure 4 Measurement results using the preheating process: a. Temperature 200°C, b. Temperature 250°C, c. Temperature 300°C.

2.1.3 Static Thermal Tensioning Process

Welding with static thermal tensioning is carried out during the welding process with heat output and also a cooler. Heating is carried out with oxy gas and cooling with water during welding with heating temperature variations of 150°, 200° and 250°. The results of welding gauge measurements on the static thermal tensioning process are as shown in Figure 5.

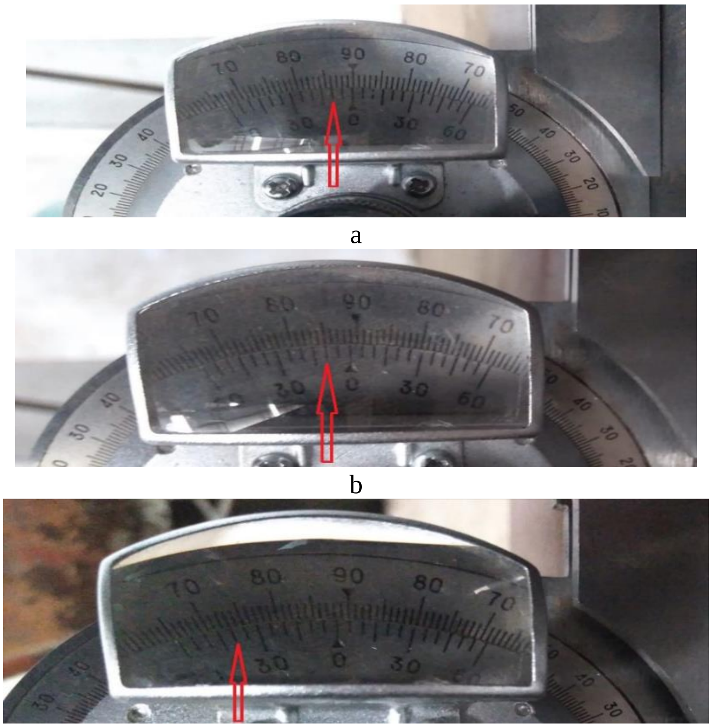

a

b

c

Figure 5 Results of static thermal tensioning distortion measurements: a. temperature 150°C, b. temperature 200°C, c. temperature 250°C.

2.1.4 Transient Thermal Tensioning Process

Welding using a transient thermal tensioning process is carried out during the welding process with a heat output and cooler. Heating is carried out with oxy gas and is directed behind the welding arc and cooler together, with heating temperature variations of 150°, 200°, 250°. The results of welding gauge measurements in the transient thermal tensioning process are as shown in Figure 6.

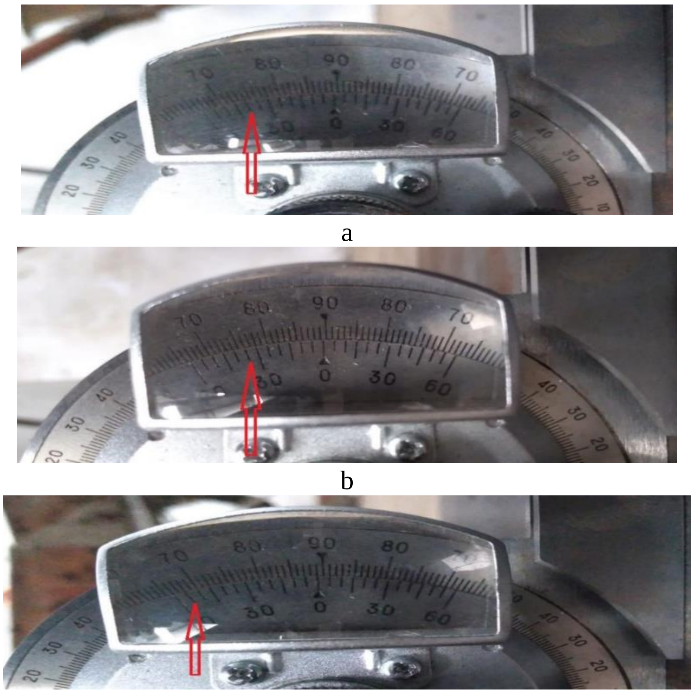

a

b

c

Figure 6 Distortion results of the transient thermal tensioning process: a. temperature 150°C, b. temperature 200°C, c. Temperature 250°C.

2.1.5 Preheating-Static Thermal Tensioning Process

Welding with this process is carried out through two heat treatments, heating the base metal before welding (preheating) and heating the base metal during the welding process with constant heat with a preheat heating temperature of 200°C and static thermal tensioning 150°C. The results of distortion measurements using a welding gauge in the preheating-static thermal tensioning process are as shown in Figure 7.

Figure 7 Results of measuring distortion data for the preheating-Static thermal tensioning process

2.1.6 Preheating-Transient Thermal Tensioning Process

Welding with this process is carried out two heat treatments, heating the base metal before welding (preheating) and heating the base metal during the welding process, the position of the heater and coolant following behind the welding arc with a preheat temperature of 200°C and transient thermal tensioning of 150°C .

The results of distortion measurements using a welding gauge are as shown in Figure 8.

Figure 8 Results of measuring distortion data from the preheating-transient thermal tensioning process

3. RESULTS AND DISCUSSION

3.1 Results

The data obtained in this research comes from the results of distortion measurements with a bavel universal protractor. So that the results of the welding method are obtained to minimize distortion. The measurement results are as in Figure 9.

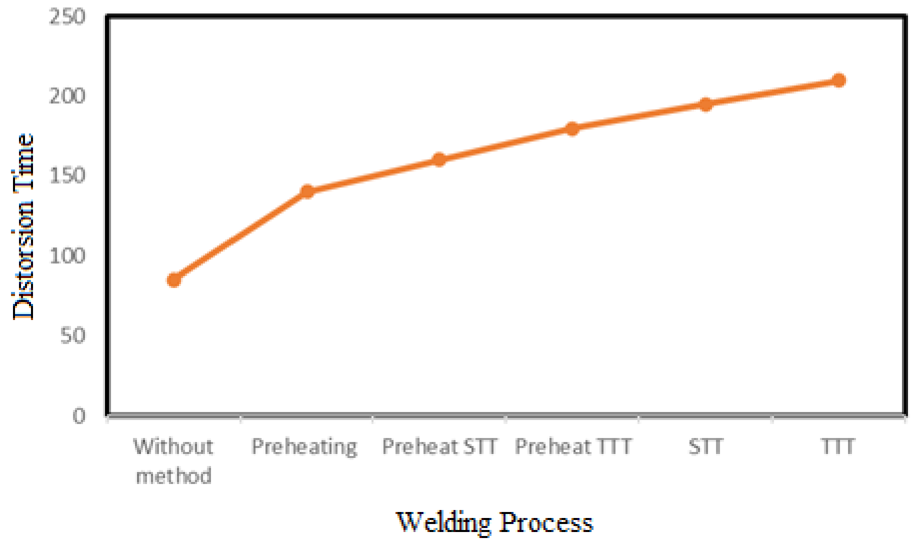

Figure 9 Welding Process

Figure 9 provides experimental data on the various welding processes used, measured in degrees. welding processes include untreated processes, preheating processes, STT preheating, TTT preheating, STT static thermal stress, and TTT transient thermal stress. The research results show the maximum temperature achieved in the welding process with each method. This temperature is an important indication of the energy level applied to the welding process and has a major influence on corner distortion in SS400 steel corner joints.

Data processing used Minitab 18 software, using the One Way Anova method, based on analysis with Minitab 18 software as shown in table 1-5.

Distortion Data versus Welding Process

Process

Null hypothesis	All means are equal
Alternative hypothesis	Not all means are equal
Significance level α	= 0.05

Table 1 Equal variances were assumed for the analysis.

Factor	Levels	Values
Welding Process	12	Preheating + STT; Preheating + TTT; Preheating 200°C; Preheating 250°C; Preheating 300°C; Static Thermal Tensioning 150°C; Static Thermal Tensioning 200°C; Static Thermal Tensioning 250°C; without threatment; Transient Thermal Tensioning 150°C; Transient Thermal Tensioning 200°C; Transient Thermal Tensioning 250°C

Table 2 Analysis of Variance Combination Preheating, Static-transient Thermal Tensioning

Source	DF	Adj SS	Adj MS	F-Value	P-Value
Welding Process	11	4,460	0,40547	9,62	0,000
Error	24	1,012	0,04215		
Total	35	5,472			

Where,

Reject H_0 if P value < 0.05

P value 0.000 < 0.05 So H_0 is rejected

This means that not all of them are the same, meaning that not all welding processes are the same or that there are significant differences between the three processes used.

Tabel 3 Analysis of Variance Preheating

Source	DF	Seq SS	Contribution	Adj SS	Adj MS	F-Value	P-Value
Welding Process	2	0,3289	68,92%	0,3289	0,16444	6,65	0,030
Error	6	0,1483	31,08%	0,1483	0,02472		
Total	8	0,4772	100,00%				

Where,
Reject H_0 if P value < 0.05
P value 0.030 < 0.05 So H_0 is rejected
This means that the preheating welding process is not the same or there are significant differences in the preheating process used.

Table 4 Analysis of Variance Static Thermal Tensioning

Source	DF	Seq SS	Contribution	Adj SS	Adj MS	F-Value	P-Value
Welding Process	2	2,0339	88,60%	2,0339	1,01694	23,32	0,001
Error	6	0,2617	11,40%	0,2617	0,04361		
Total	8	2,2956	100,00%				

Where,
Reject H_0 if P value < 0.05
P value 0.001 < 0.05 So H_0 is rejected
This means that the Static Thermal Tensioning welding process is not the same or there are significant differences in the Static Thermal Tensioning process used.

Table 5 Analysis of Variance Transient Thermal Tensioning

Source	DF	Seq SS	Contribution	Adj SS	Adj MS	F-Value	P-Value
Welding Process	2	0,4289	41,82%	0,4289	0,21444	2,16	0,197
Error	6	0,5967	58,18%	0,5967	0,09944		
Total	8	1,0256	100,00%				

Where
Reject H_0 if P value < 0.05
P value 0.197 < 0.05 So H_0 is accepted
The conclusion is that the same means the Transient Thermal Tensioning welding process or there is no significant difference in the Transient Thermal Tensioning process used. Figure 3 shows the results of measuring distortion with a universal protractor, with each re-welding process 3 times.

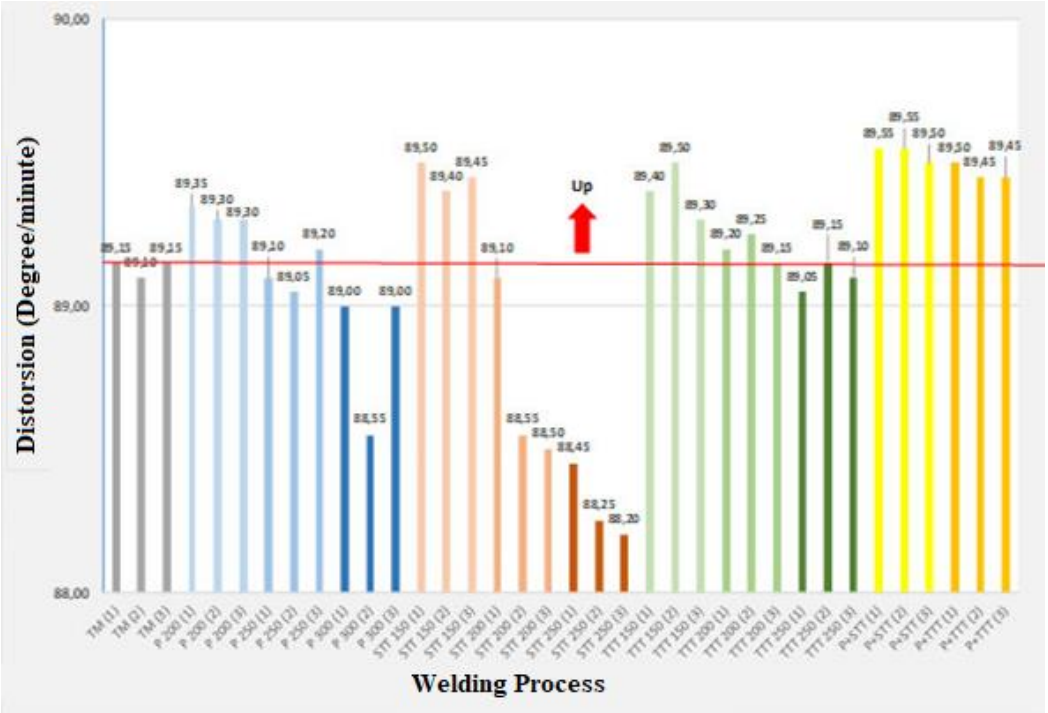

Figure 3 Distortion Data

Where,

● : Without Methods
● : Preheating 200°C
● : Preheating 250°C
● : Preheating 300°C
● : Static Thermal Tensioning 150°C
● : Static Thermal Tensioning 200°C
● : Static Thermal Tensioning 250°C
● : Transient Thermal Tensioning 150°C
● : Transient Thermal Tensioning 200°C
● : Transient Thermal Tensioning 250°C
● : Preheating + Static Thermal Tensioning
● : Preheating + Transient Thermal Tensioning

The welding process without treatment (red line) is a reference point for whether there is a change in the distortion results after several welding processes. A good welding process is above the red line. The process with good results is above the reference point, namely 89°15'. From the results of the distortion data in Figure 3, it is stated that the good results are:

- Preheating + Static Thermal Tensioning, 89°55’
- Preheating + Transient Thermal Tensioning, 89°50’
- Static Thermal Tensioning 150°C, 89°45’
- Transient Thermal Tensioning150°C, 89°40’
- Preheating 200°C, 89°35’

The results of the welding process data are no better for minimizing distortion, namely:

- Preheating 250°C, 89°10’
- Preheating 300°C, 89°
- Static Thermal Tensioning 200°C, 88°55’
- Static Thermal Tensioning 250°C, 88°25’
- Transient Thermal Tensioning250°C, 89°05’

4. CONCLUSION

The smallest distortion was obtained from a temperature variation of 150°C of 89°45', and the largest distortion was obtained with a temperature variation of 250°C of 88°20'. And there is no significant influence of the transient thermal tensioning welding method on the distortion results. The smallest distortion results were obtained from a temperature variation of 150°C of 89°40', and the largest distortion was obtained with a temperature variation of

250°C of 89°10'. Meanwhile, there is a significant influence of the preheating welding method on the distortion results. The smallest distortion results were obtained from a temperature variation of 200°C of 89°35', and the largest distortion was obtained with a temperature variation of 300°C of 89°. There is a significant influence of the combination of preheating and static-transient thermal tensioning welding methods on the distortion results. The smallest distortion result was 89°55', and the largest distortion was 89°45'.

6. REFERENCES

[1] A. Aggarwal, D. Adlakha, and P. Khanna, "Development of a mathematical model to predict angular distortion in FCA welded stainless steel 301 plates," *Mater. Today Proc.*, vol. 78, 2023, doi: 10.1016/j.matpr.2022.11.478.

[2] H. Alipooramirabad, A. Paradowska, R. Ghomashchi, and M. Reid, "Investigating the effects of welding process on residual stresses, microstructure and mechanical properties in HSLA steel welds," *J. Manuf. Process.*, vol. 28, 2017, doi: 10.1016/j.jmapro.2017.04.030.

[3] C. P. Alvarães, F. C. A. Madalena, L. F. G. De Souza, J. C. F. Jorge, L. S. Araújo, and M. C. Mendes, "Performance of the INCONEL 625 alloy weld overlay obtained by FCAW process," *Rev. Mater.*, vol. 24, no. 1, 2019, doi: 10.1590/s1517-707620190001.0627.

[4] A. V. Balan, T. Kannan, and N. Shivasankaran, "Effect of FCAW process parameters on bead geometry in super duplex stainless steel claddings," *Int. J. Appl. Eng. Res.*, vol. 9, no. 24, 2014.

[5] G. Bansal Rajkumar and N. Murugan, "Prediction of Flux cored arc welding process parameters effect on 2205 duplex stainless steel," *Weld. Cut.*, vol. 12, no. 1, 2013.

[6] A. Burgos, H. Svoboda, Z. Zhang, and E. Surian, "Alternative PWHT to Improve High-Temperature Mechanical Properties of Advanced 9Cr Steel Welds," *J. Mater. Eng. Perform.*, vol. 27, no. 12, 2018, doi: 10.1007/s11665-018-3736-5.

[7] E. Dogan, M. Ay, M. Kurtulmus, A. I. Yukler, and A. Etyemez, "Effects of welding parameters on the angular distortion of welded steel plates," *Open Chem.*, vol. 20, no. 1, 2022, doi: 10.1515/chem-2022-0152.

[8] W. A. R. Harahap, "Studi Awal Pengelasan Kombinasi GMAW-FCAW Dengan Variasi Arus Weld Metal Menggunakan Proses Wire Arc Additive Manufacturing (WAAM) Terhadap Nilai Kekuatan Tarik Dan Struktur Mikro," *Teknologi*, 2021.

[9] C. Hwang *et al.*, "Evaluation and Prediction of Formation of Heat-Affected Zone and Mechanical Properties According to Welding Method of STS 316L/A516-70N Clad Plates," *J. Korean Inst. Met. Mater.*, vol. 60, no. 12, 2022, doi: 10.3365/KJMM.2022.60.12.873.

[10] J. Jiang, J. Zhang, J. Liu, S. P. Chiew, and C. K. Lee, "Effect of welding and heat treatment on strength of high-strength steel columns," *J. Constr. Steel Res.*, vol. 151, 2018, doi: 10.1016/j.jcsr.2018.09.027.

[11] S. C. Juang and Y. S. Tarng, "Process parameter selection for optimizing the weld pool geometry in the tungsten inert gas welding of stainless steel," *J. Mater. Process. Technol.*, vol. 122, no. 1, 2002, doi: 10.1016/S0924-0136(02)00021-3.

[12] J. Kim and J. Kim, "Laser welding of astm a553-1 (9% nickel steel) (part ii: Comparison of mechanical properties with fcaw)," *Metals (Basel).*, vol. 10, no. 8, 2020, doi: 10.3390/met10080999.

[13] V. V. Kumar and N. Murugan, "Effect of FCAW Process Parameters on Weld Bead Geometry in Stainless Steel Cladding," *J. Miner. Mater. Charact. Eng.*, vol. 10, no. 09, 2011, doi: 10.4236/jmmce.2011.109064.

[14] K. H. Ling, Y. K. Fuh, T. C. Kuo, and S. Xun-Tu, "Effect of welding sequence of a multi-pass temper bead in gas-shielded flux-cored arc welding process: hardness, microstructure, and impact toughness analysis," *Int. J. Adv. Manuf. Technol.*, vol. 81, no. 5–8, 2015, doi: 10.1007/s00170-015-7277-x.

[15] M. Malhotra, Kashish, Samridhi, and P. Khanna, "Prediction of angular distortion in flux-cored arc welding of stainless steel 301 plates by mathematical modelling," *Mater. Today Proc.*, vol. 62, 2022, doi: 10.1016/j.matpr.2022.04.426.

[16] J. L. Meseguer-Valdenebro, J. Serna, A. Portoles, M. Estrems, V. Miguel, and E. Martínez-Conesa, "Experimental Validation of a Numerical Method that Predicts the Size of the Heat Affected Zone. Optimization of the Welding Parameters by the Taguchi's Method," *Trans. Indian Inst. Met.*, vol. 69, no. 3, 2016, doi: 10.1007/s12666-015-0554-4.

[17] P. K. Palani and N. Murugan, "Optimization of weld bead geometry for stainless steel claddings deposited by FCAW," *J. Mater. Process. Technol.*, vol. 190, no. 1–3, 2007, doi: 10.1016/j.jmatprotec.2007.02.035.

[18] P. K. Palani, N. Murugan, and B. Karthikeyan, "Process parameter selection for optimising weld bead geometry in stainless steel cladding using Taguchi's approach," *Mater. Sci. Technol.*, vol. 22, no. 10, 2006, doi: 10.1179/174328406X118294.

[19] M. Palpandi, G. Magudeeswaran, and N. Harikannan, "Optimization of pulsed current flux cored arc welding parameters for ferrite phase in duplex stainless steel welds," *J. Balk. Tribol. Assoc.*, vol. 26, no. 2, 2020.

[20] M. Palpandi, G. Magudeeswaran, and N. Harikannan, "Optimization of pulsed current flux cored arc

welding parameters for ferrite phase in duplex stainless steel welds," *J. Balk. Tribol. Assoc.*, vol. 25, no. 4, 2019.
[21] A. Sehrawat, "Mathematical Modelling for Prediction of Angular Distortion in MIG Welding of Stainless Steel 301," *Int. J. Res. Appl. Sci. Eng. Technol.*, vol. 8, no. 7, 2020, doi: 10.22214/ijraset.2020.30372.

LOGIC
Journal of Engineering Design and Technology
Vol. 24 No.2 July 2024 ; p. 49 - 62

p-ISSN : 1412-114X
e-ISSN : 2580-5649
http://ojs2.pnb.ac.id/index.php/LOGIC

DESIGN & IMPLEMENTATION OF MPPT SOLAR PHOTOVOLTAIC - ELECTRIC VEHICLES IN FAST VARYING PARTIAL SHADING CONDITIONS USING SERVAL OPTIMIZATION ALGORITHM

Hendry C. Saputra, SST.1), Dr. Isdawimah, MT.2), Dr. Belyamin, Msc. 3)

1) Electrical Engineering Department, Politeknik Negeri Jakarta, Jl. Prof. Dr. G.A. Siwabessy, Depok, Indonesia
2) Electrical Engineering Department, Polytechnic Negeri Jakarta, Jl. Prof. Dr. G.A. Siwabessy, Depok, Indonesia
3) Mechanical Engineering Department, Polytechnic Negeri Jakarta, Jl. Prof. Dr. G.A. Siwabessy, Depok, Indonesia

Corresponding email 1) :
hendry.christiansaputra.te19@mhsw.pnj.ac.id

Abstract. Solar panels are used to convert solar energy into electrical energy. In this study it was applied to electric vehicles which have a very large potential for being constrained by shadows. In fast varying partial shading conditions, the position of the maximum power point is divided into two, namely GMPP and LMPP. This condition makes the MPPT process stuck in LMPP. Therefore, this research proposes the application of Serval Optimization Algorithm (SOA) in MPPT. This method refers to the natural behavior of the serval in nature. The fundamental inspiration of SOA is the serval hunting strategy in two stages of exploration and exploitation. The SOA is implemented in MPPT to change (duty cycle) so that it gets the best value and produces maximum solar panel output power. This SOA method was chosen to complete the partial shading conditions so that MPPT can optimally reach GMPP without going through LMPP. The solar panels used in this system are 2 units with specifications of 25 Wp with a 24V battery load and a 120W BLDC Motor compact in Electric Vehicle - Two Wheeler Scooter. MPPT SOA was tested in a simulation using PSIM and actual Software in 6 variations of normal and partial shading conditions. In the Simulation Test of Partial Shading Conditions, an average accuracy of 99.958% and an average tracking time of 0.492 seconds were obtained. SOA has a higher accuracy than PSO and GWO, which is 99.95%. And it has a faster tracking time of 0.55 seconds. In the SOC Integration Test, the SOA Method obtained an error value of 6.48% better than the GWO Method. On the Road Test with 6 condition, it can slow down the value of the decrease in battery capacity by 16.24%. The application of Single Source on the PV-MPPT-Converter can be implemented with an efficiency value of 76.86%. In previous research where SOA is a new method in Optimizing Problem Solving which has quite good accuracy performance, and in this research it can be implemented in Solar PV Optimization to track MPPT electric vehicles with varied and fluctuating partial shading conditions.

Keywords : Serval Optimization Algorithm (SOA), Fast-varying Partial Shading, Maximum Power Point Tracking (MPPT), State of Charge (SOC), Electric Vehicle.

1. INTRODUCTION

The emergence of EV (electric vehicles) is inevitable. In Indonesia, EV has been introduced in various forms. In Indonesia, battery BEV (electric vehicles) have been introduced by several well-known manufacturers. However, their adoption is still limited to a handful of people, considering that vehicle prices are still very high and unaffordable for most car drivers. In addition, the availability of public infrastructure for battery charging stations is still minimal and limited. This ecosystem will include charging station infrastructure, nickel raw material providers, battery manufacturers, component makers, and EV assemblers/manufacturers. Several foreign investors have expressed their interest in becoming an important player in the electric vehicle business ecosystem in Indonesia [1].

There are several problems that affect BEV performance:

1. Behavior of BEV drivers regarding duration of use, charging and idle conditions;
2. Unbalancing Power Flow Control on the Grid;
3. Battery performance (Battery Aging, Unbalance condition, Battery Degradation, SOC SOH measurement accuracy);
4. The results of the aggregation of purchasing intentions from all sources are 0.77 to buy and 0.23 not to buy or buying is preferred to not buying with a ratio scale of 3.35. It should be noted that these results do not mean that 77% of target customers will buy a BEV and 23% will not. [1].

There are several problems that affect the performance of Solar PV (details can be seen in Table 1.):

1. Tracking Duration, Oscillation, and MPPT Control Efficiency of Solar PV;
2. The accuracy of the implementation of the MPPT Algorithm.

Table 1. The Comparison of MPPT Algorithm

Reff	Method	Category	Criteria Parameter		
			Time Tracking	Oscillation Level	Efficiency
1	P & O	Conventional	0,4 – 3 s	High	70,77 – 99,99 %
2	P & O	Conventional	0,11 – 0,153 s	High	84,71 – 99,98 %
3	P & O	Conventional	0,08 s	High	99,28 %
4	IC	Conventional	0,3 s	High	61,89 %
5	IC	Conventional	0,434 – 0,479 s	High	100 %
6	PSO	Metaheuristic	0,11 – 0,172 s	Low	99,84 – 99,98 %
7	PSO	Metaheuristic	0,8 s	Low	91,42 %
8	ANN	Metaheuristic	0,063 s	Low	99,97 %
9	ANN	Metaheuristic	0,065 – 0,083 s	Low	90,6 – 99,25 %
10	DE	Metaheuristic	0,309 s	Low	99,9 %
11	DE	Metaheuristic	0,075 – 0,014 s	Low	98,6 – 99,1 %

Based on literature studies related to the application of Conventional-Metaheuristic algorithms in MPPT Solar PV where each method has advantages and disadvantages [2]. This research will carry out development by considering changes in partial shading conditions which are quite fast due to mobile conditions. On the DC Converter side, to be able to balance Pick differences in Solar PV irradiance conditions, the combined Buck-Boost converter is considered more optimal than just Boost/Buck [3] [4], or those using High Freq Inverters [5].

The advantage of this research is optimizing the performance of Solar PV as a Mobile Source so that it supports more optimal battery lifetime performance. Application of MPPT Buck-Boost Converter Combination on Solar PV output [3]. So that it is expected to further stabilize the output voltage and current due to Partial Shading and Variations of Rapid Changes in irradiance conditions and Implementation of the Serval Optimization (SOA) Algorithm where the algorithm scheme is a hunting strategy to attack the selected prey and then hunt the prey. SOA implementation steps in two stages of exploration and exploitation. As well as the implementation of PV & Battery monitoring conditions that can be monitored.

2. METHODS

This research was conducted through the Process of Design, Testing and Data Analysis. Monitoring the characteristics of the voltage and current originating from Solar PV until a power optimization setting is obtained which is then gradually sent through the converter to the battery for storage and then transferred to the BLDC Motor as a load. In this research, MPPT Control and Buck-Boost Converter function as regulators to obtain the most optimal power level due to drop voltage and load disturbance. Caused by the Partial Shading Condition, the System Flow can be seen in the image below.

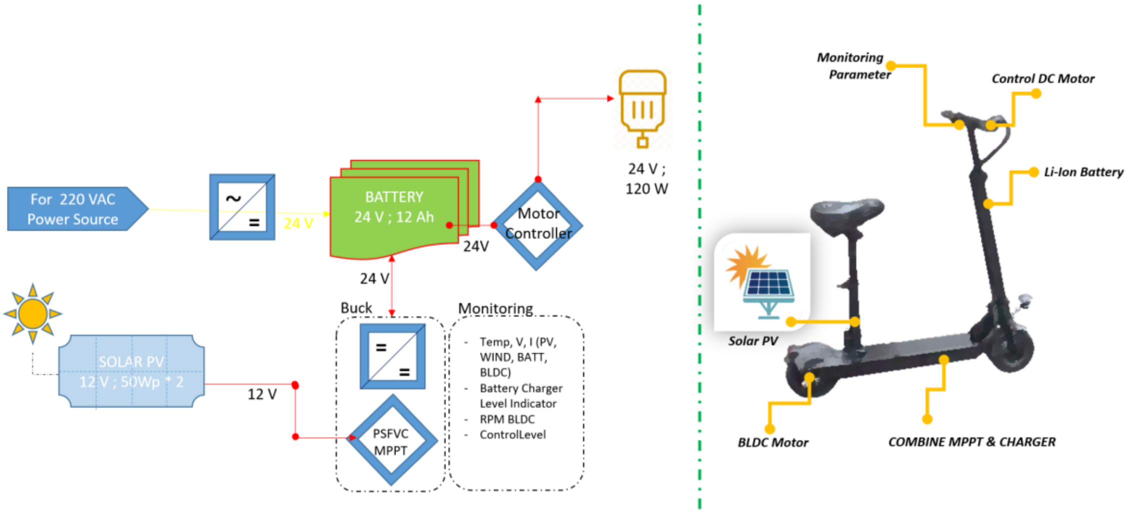

Figure 1. General Design System

2.1 System Design Simulation & Algoritma MPPT

First step of design for this research are by simulating system in PSIM software for knowing the working system properly. The circuit diagram as below :

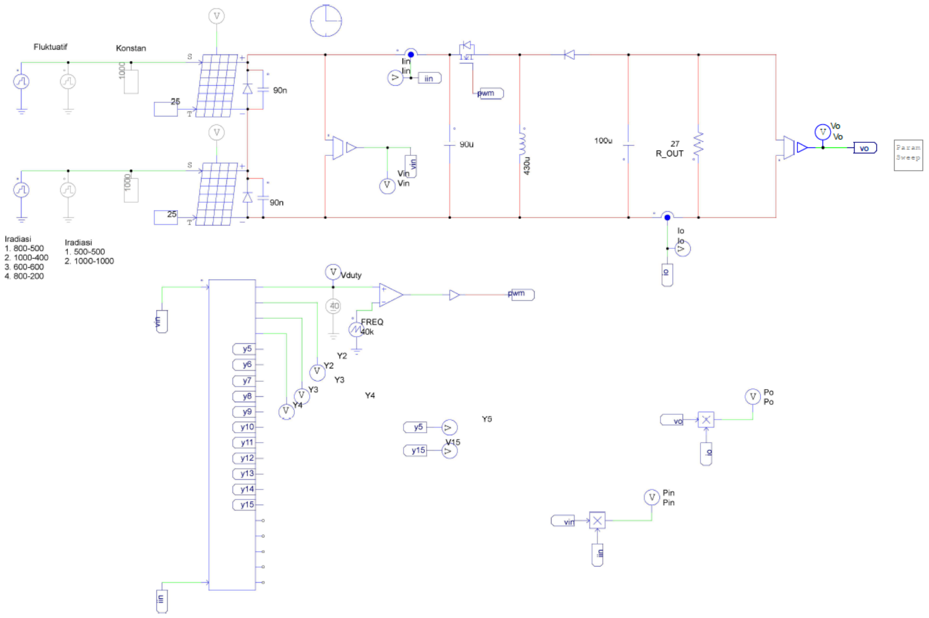

Figure 2. Electrical Design by PSIM Simulator

The next step is uploading the MPPT SOA Algorithm for measurement, compare & Analyze before hardware implementation. Flow chart algorithm as below :

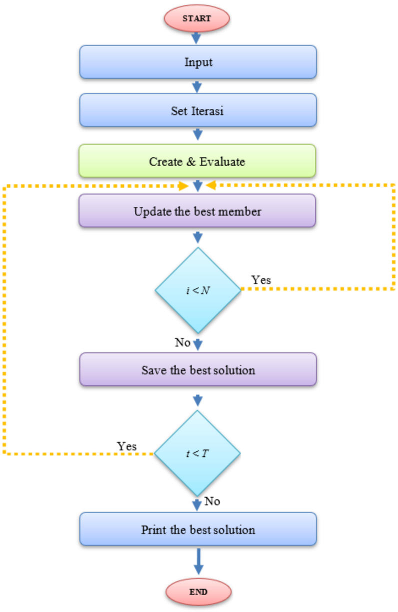

Figure 3. Flow Chart SOA Algorithm

2.2 Iteration Calculation SOA Algorithm

Calculations are performed as baseline parameters. The conditions implemented are partial shading with a reference value of irradiation of:

a. Solar PV I = 1000 W/m2
b. Solar PV II = 400 W/m2
c. With T 1 up to 5 using equation

$$d[T] = d[T] + r1 * (d_{best} - r3 * d[T]) \tag{1}$$

The number of sampling iterations calculated is 3 iterations in the following table:

Table 2. Iteration Calculation

Iteration 0	**Iteration 1**	**Iteration 2**	**Iteration 3**
$d_1^0 = 22$	$d_1^0 = 34.54$	$d_1^0 = 50.96$	$d_1^0 = 64.8$
$d_2^0 = 33$	$d_2^0 = 41.6$	$d_2^0 = 50.28$	$d_2^0 = 65$
$d_3^0 = 44$	$d_3^0 = 65$	$d_3^0 = 65$	$d_3^0 = 65$
$d_4^0 = 55$	$d_4^0 = 61.6$	$d_4^0 = 65$	$d_4^0 = 65$
$d_5^0 = 65$	$d_5^0 = 65$	$d_5^0 = 63.6$	$d_5^0 = 62.2$
d_{best}= 55	d_{best}= 55	d_{best}= 55	d_{best}= 55
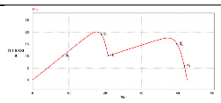	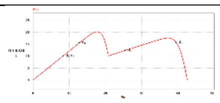	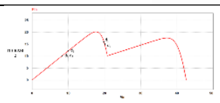	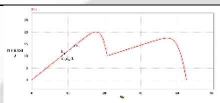

2.3 Hardware Design

For Making circuit Hardware connection must starting by PCB Design and continuing make a port of hardware semiconductor, microprocessor, sensor, etc.

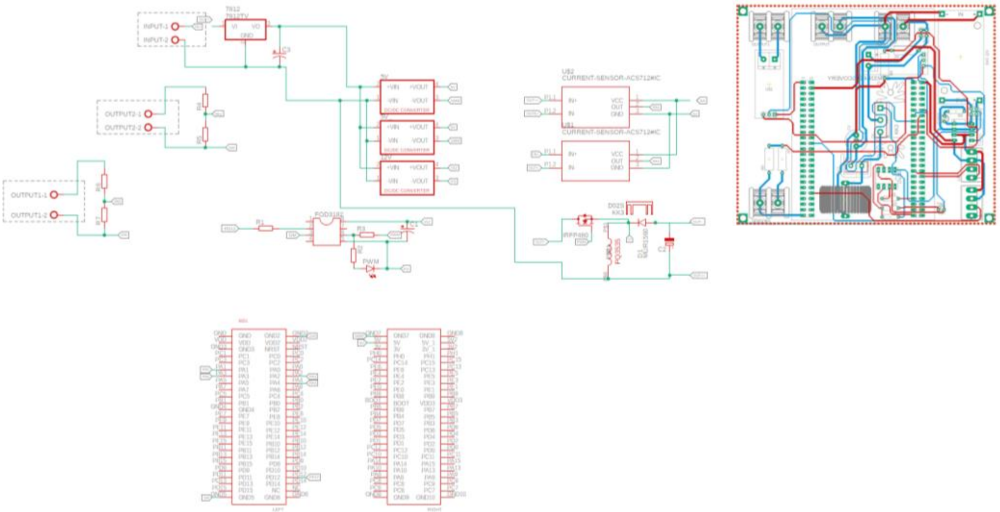

Figure 4. MPPT Diagram Block – Buck Boos Converter & PCB Design

2.4 Hardware Integration

Hardware Integration are connecting between Microcontroller, Solar PV, Battery & BLDC Motor with the mechanical wheeling system. The Design of Hardware starting when the simulation by software simulator (Eagle & PSIM) already firm & works by SOA MPPT method.

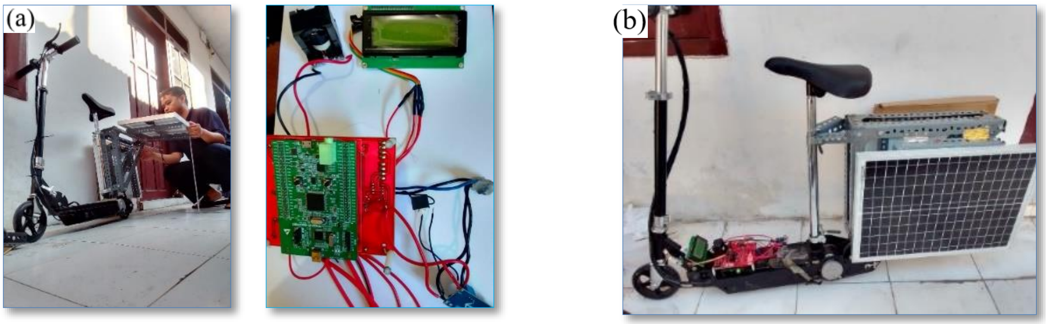

Figure 5. Hardware Integration: (a) Solar PV & MPPT Installation & (b) Microcontroller, LCD, Converter, Battery & BLDC Installation

2.5 Data collection, observation, measurement & analysis techniques

Data collection, observation, measurement & analysis techniques consist of:

(a) MPPT SOA Characteristic Test:
  - i. Characteristic Test Solar PV
  - ii. SOA Simulation Test (Uniform & Partial Shading Condition)
  - iii. SOA Simulation Test (Fluctuation Shading Condition)

(b) MPPT SOA System Test
  - i. Sub System Real Condition Test
    - Sub System Buck Boost Converter Test
    - MPPT System Test with Variable Condition (Non Shading and Partial Shading)
  - ii. Integration Test Real Condition & Comparation MPPT Method
    - SOA Algorithm Comparation with other Method
    - MPPT System Integration Test

3. RESULTS AND DISCUSSION

3.1 MPPT SOA Characteristic Test

a. Characteristic Test Solar PV

Table 3. PV Characteristic Test

Condition	No.	Irradiation (W/m^2)		GMPP	LMPP	Best Graphics
		PV 1	PV 2			
Uniform Condition	**1**	**1000**	**1000**	**40.4**	**-**	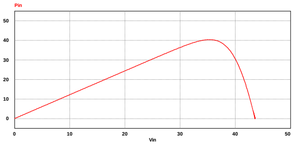
	2	800	800	32.24	-	
	3	500	500	19.90	-	
	4	400	400	15.74	-	
PSC	**5**	**1000**	**600**	**26.41**	**20.19**	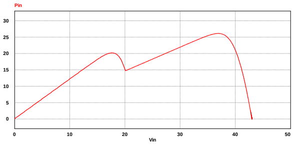
	6	1000	400	20.19	17.6	
	7	800	600	25.63	16.11	
	8	800	200	16.11	8.71	

The result of characteristic test of solar PV above are in Uniform Condition just get one pick of GMPP, beside in partial shading condition when there are have a different irradiance condition on each PV Panel. So that the output will be potentially decrease because of the LMPP result.

b. SOA Simulation Test (Uniform & Partial Shading Condition)

Table 4. SOA Simulation Test Uniform & PSC

No.	P_Ideal (W)	P_SOA (W)	Duty Cycle (%)	Converter mode	Accuracy (%)	Tracking time (second)
1	**40.4**	**40.38**	**48.26**	**Buck**	**99.95**	**0.31**
2	32.24	32.24	45.53	Buck	100.00	0.43
3	19.90	19.79	40.10	Buck	99.45	0.4
4	15.74	15.42	38.57	Buck	97.97	0.6
5	**26.41**	**26.13**	**41.79**	**Buck**	**98.94**	**0.55**
6	20.19	20.18	56.89	Boost	99.95	0.55
7	25.63	25.60	42.12	Buck	99.88	0.53
8	16.11	16.1	54.02	Boost	99.94	0.55

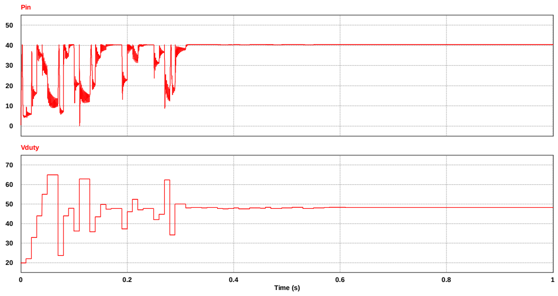

Figure 6. Graphics Simulation PV I 1000–PV II 1000

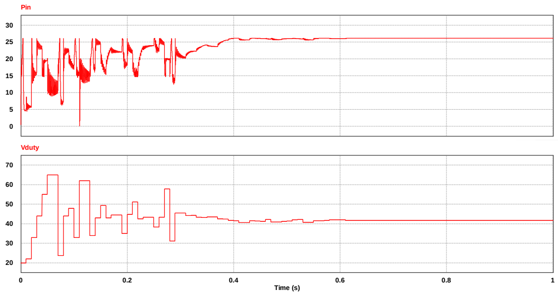

Figure 7. Graphics Simulation PV I 1000–PV II 600

After Characteristic PV Test and knowing the GMPP and LMPP, next is simulation SOA algorithm test for knowing how accurate and how fast the tracking time. With result as below :

Ideal Condition = Theory = based on Irradiance Condition by location
Accuracy = (P_SOA)/(P_ideal)×100%

The Simulation Test of SOA MPPT Algorithm in ideal condition , with accurate above 97% dan tracking time between 0,3s - 0,6s.

c. SOA Simulation Test (Fluctuation Shading Condition)

Table 5. Simulation SOA Fluctuation

Detik	**Iradiasi**		**P_Ideal**	**P_SOA**	**Duty Cycle**	**Accuracy**	**Tracking**
	PV1	**PV2**	**(W)**	**(W)**	**(%)**	**(%)**	**time (detik)**
1	500	500	19.90	19.88	40.12	99.90	0.52
2	1000	1000	40.4	40.38	48.09	99.95	0.37

Detik	**Iradiasi**		**P_Ideal**	**P_SOA**	**Duty Cycle**	**Accuracy**	**Tracking**
	PV1	**PV2**	**(W)**	**(W)**	**(%)**	**(%)**	**time (detik)**
1	800	800	32.24	32.23	45.4	99.97	0.55
2	1000	400	20.19	20.18	56.83	99.95	0.41
3	800	200	16.11	16.11	54.01	100.00	0.5
4	1000	1000	40.4	40.39	48.07	99.98	0.6

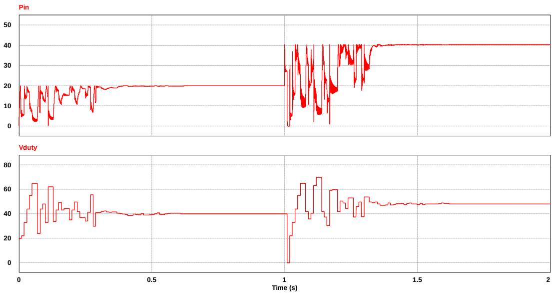

Figure 8. Graphics Simulation 2 s

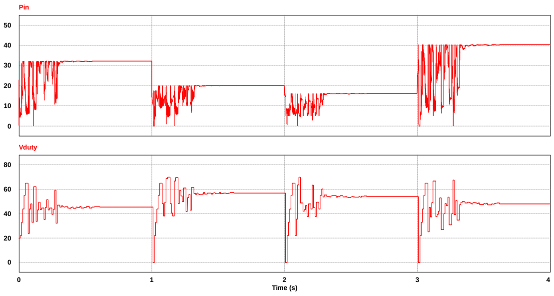

Figure 9. Graphics Simulation 4 s

The purposes of This testing is want to simulate a various partial shading condition it could be happened when the electric vehicle on movement situation with many shading condition by tree, other vehicle, etc. The result of MPPT SOA Algorithm in fluctuation condition when 2 second uniform and 4 second PSC with accurate result above 99% dan tracking time between 0,4s – 0,6s.

3.2 MPPT SOA System Test

a. Sub System Real Condition Test

i. Sub System Buck Boost Converter Test

Table 6. Sub System Buck Boost Converter Test

D	**Vin**	**In**	**Vout**	**Iout**	**Pin**	**Pout**	**Eff**
30	15	0,18	5,76	0,2	2,7	1,152	42,67

	20	0,193	7,89	0,26	3,86	2,0514	53,15
	25	0,22	10,04	0,34	5,5	3,4136	62,07
	30	0,251	12,2	0,4	7,53	4,88	64,81
	35	0,279	14,36	0,46	9,765	6,6056	67,65
	40	0,313	16,52	0,53	12,52	8,7556	69,93
40	15	0,314	9,07	0,32	4,71	2,9024	61,62
	20	0,385	12,35	0,42	7,7	5,187	67,36
	25	0,46	15,64	0,52	11,5	8,1328	70,72
	30	0,54	18,94	0,62	16,2	11,7428	72,49
	35	0,622	22,25	0,72	21,77	16,02	73,59
	40	0,704	25,55	0,81	28,16	20,6955	73,49
50	15	0,726	14,9	0,5	10,89	7,45	68,41
	20	0,93	20,12	0,68	18,6	13,6816	73,56
	25	1,15	25,33	0,82	28,75	20,7706	72,25
	30	1,37	30,61	0,98	41,1	29,9978	72,99
	35	1,592	35,87	1,12	55,72	40,1744	72,10
	40	1,82	41,04	1,26	72,8	51,7104	71,03
60	15	1,25	19,79	0,66	18,75	13,0614	69,66
	20	1,63	26,56	0,87	32,6	23,1072	70,88
	25	2,034	33,47	1,12	50,85	37,4864	73,72
	30	2,42	40,04	1,3	72,6	52,052	71,70
	35	2,8	46,18	1,47	98	67,8846	69,27
65	15	1,8	23,45	0,82	27	19,229	71,22
	20	2,39	31,79	1,08	47,8	34,3332	71,83

Optimal

D	Vin	In	Vout	Iout	Pin	Pout	Eff
43	35,6	0,784	25,54	0,84	27,9104	21,4536	76,86597

ii. MPPT System Test with Variable Condition (Non Shading and Partial Shading)

Test with real irradiance condition: PV Case 1 - Non PSC PV Case 2 – PSC PV I (variable load) PV Case 3 – PSC PV I (variable duty cycle) PV Case 4 – PSC PV II (variable load) PV Case 5 – PSC PV II (variable duty cycle)	Case 1 
Case 2 	Case 3 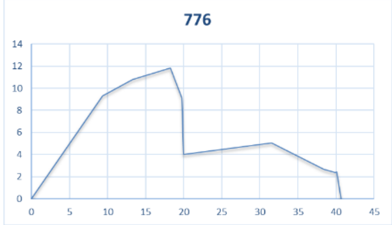
Case 4 	Case 5 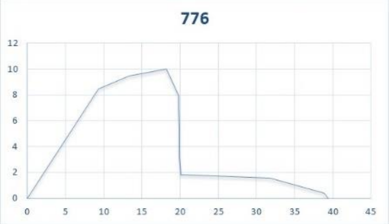

Figure10. MPPT sub system Test

b. Integration Test Real Condition & Comparation MPPT Method
   i. SOA Algorithm Comparation with other Method

Table 7. Uniform Condition

ALGORITMA	P_IDEAL	P_MPP	ACC	TRACKING TIME
SOA	20,19 1000 1000	20,18	**99,95**	**0,55**
PSO		20,11	99,60	0,57
GWO		20,1	99,55	0,6
ALGORITMA	P_IDEAL	P_MPP	ACC	TRACKING TIME
SOA	32,24 800 800	32,236	**99,99**	**0,43**
PSO		32,04	99,38	0,6
GWO		32,23	99,97	0,6

Table 8. Fluctiation Condition

Detik	**Iradiasi**		**P_Ideal (W)**	**P_SOA (W)**	**Duty Cycle (%)**	**Accuracy (%)**	**Tracking time (detik)**
	PV1	PV2					
1	500	500	19,9	19,88	40,12	99,90	0,52
2	1000	1000	40,4	40,38	48,09	99,95	0,37
					Average	99,92	0,45

Detik	**Iradiasi**		**P_Ideal (W)**	**P_ PSO (W)**	**Duty Cycle (%)**	**Accuracy (%)**	**Tracking time (detik)**
	PV1	PV2					
1	500	500	19,9	19,22	39,9	96,58	0,55
2	1000	1000	40,4	40,02	48,25	99,06	0,5
					Average	97,82	0,53

Detik	Iradiasi		P_Ideal (W)	P_GWO (W)	Duty Cycle (%)	Accuracy (%)	Tracking time (detik)
	PV1	PV2					
1	500	500	19,9	19,85	39,55	99,75	0,6
2	1000	1000	40,4	40,3	48,48	99,75	0,6
					Average	99,75	0,60

Table 9. Fast Varying Partial Shading

Detik	Iradiasi		P_Ideal (W)	P_SOA (W)	Duty Cycle (%)	Accuracy (%)	Tracking time (detik)
	PV1	PV2					
1	800	800	32,24	32,23	45,4	99,97	0,55
2	1000	400	20,19	20,18	56,83	99,95	0,41
3	800	200	16,11	16,11	54,01	100,00	0,5
4	1000	1000	40,4	40,39	48,07	99,98	0,6
					Average	99,97	0,52

Detik	Iradiasi		P_Ideal (W)	P_PSO (W)	Duty Cycle (%)	Accuracy (%)	Tracking time (detik)
	PV1	PV2					
1	800	800	32,24	32,04	45,47	99,38	0,6
2	1000	400	20,19	20,18	56,76	99,95	0,58
3	800	200	16,11	16,1	54,15	99,94	0,6
4	1000	1000	40,4	39,4	48,16	97,52	0,58
					Average	99,20	0,59

Detik	Iradiasi		P_Ideal (W)	P_GWO (W)	Duty Cycle (%)	Accuracy (%)	Tracking time (detik)
	PV1	PV2					
1	800	800	32,24	32,22	45,49	99,94	0,6
2	1000	400	20,19	20,12	56,77	99,65	0,6
3	800	200	16,11	16,1	53,93	99,94	0,6
4	1000	1000	40,4	-	-	0,00	-
					Average	74,88	0,6

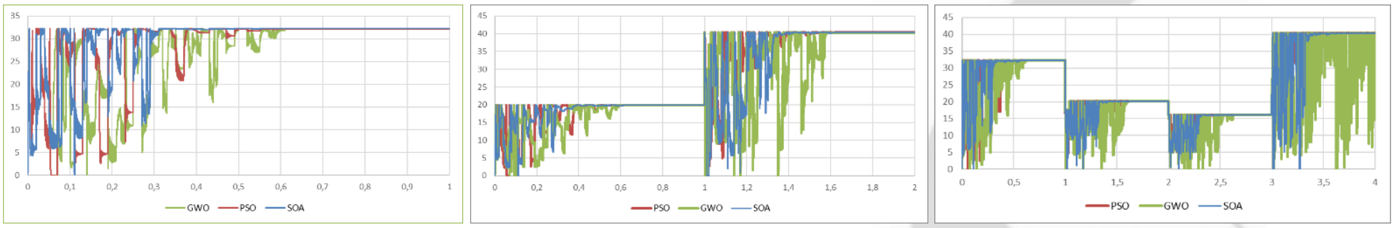

Figure 11. Graphics of Uniform 800 – 800, Fluctuation, Fast Varying Partial Shading Condition

ii. MPPT System Integration Test (13 Test Condition)

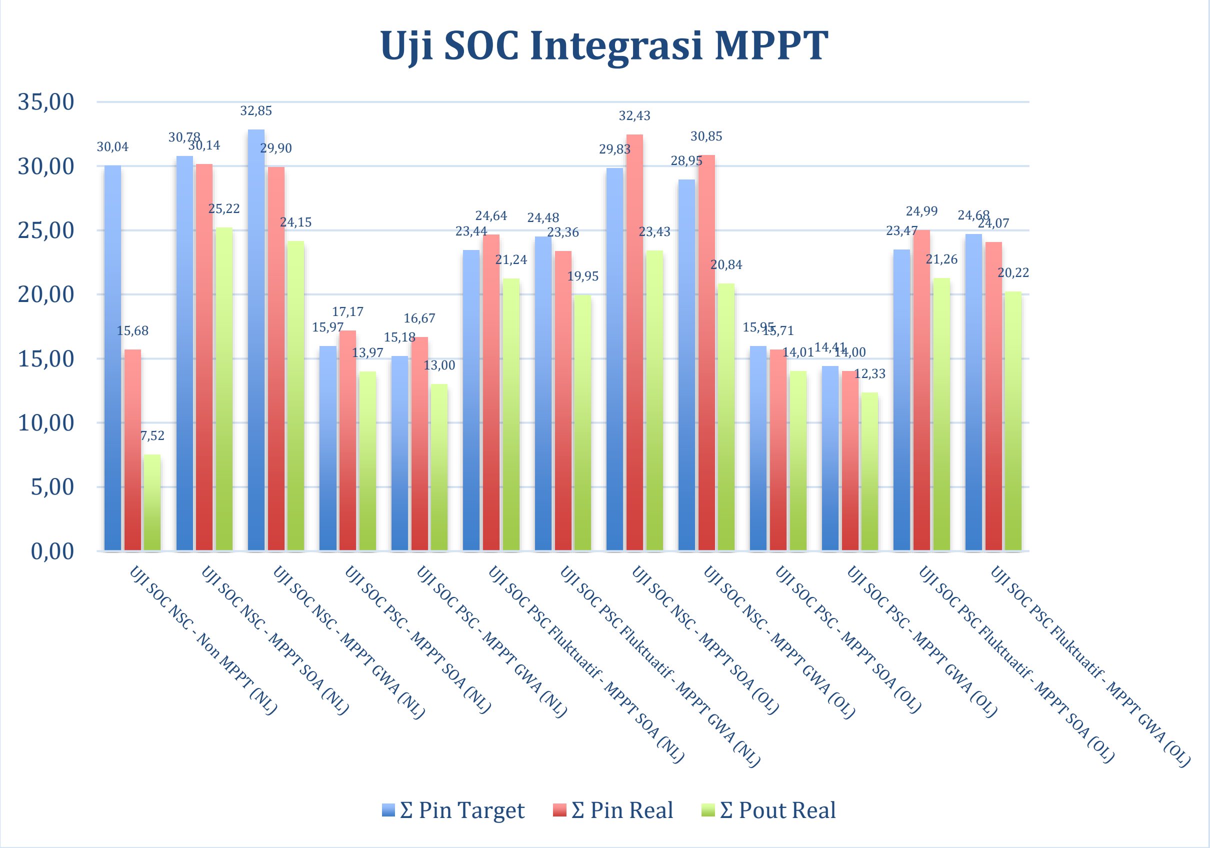

Figure 12. MPPT System Integration Test

The Result of comparison of MPPT System integration test as below :

- In No Load Testing with Fluctuation PSC, the best result is SOA (output 21,24 by 23,44) ; GWA (output 19,95 by 24,48)
- In On Load Testing with Fluctuation PSC, the best result is SOA (output 21,26 by 23,47) ; GWA (output 20,22 by 24,68)

3.3 Citation and References

a. Electric Vehicle

An electric bicycle that will be driven with the help of a battery and thus provide the necessary voltage to the motor. This bicycle can be driven with the help of electricity or also with the help of solar energy. An electric bicycle is a bicycle that is powered by a battery coupled to an electric motor [6] [17].

b. Battery System

The Thevenin topology for a lithium-ion battery is shown in Figure 13, where Vocv is the electric motor power of the battery, R1 and R2 are defined as the internal resistor and ohmic polarization resistor, and C is the polarization capacitor, which is connected in parallel with the polarization resistance R2 [7] [13] [14] [15] [16].

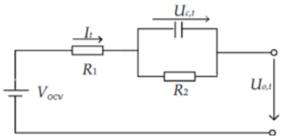

Figure 13. Battery Thevenin Topology

c. Solar Photovoltaic

Solar panels are semiconductor components that function to convert solar energy into electrical energy. The energy conversion is carried out by releasing electrons when receiving stimulation from sunlight. The semiconductor material used in solar panels to convert this energy is silicon. This material consists of two layers, namely a negatively charged layer (N) and a positively charged layer (P), as shown in the following figure [8].

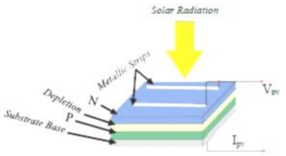

Figure 14. Solar Photovoltaic

Solar panels have an ideal equivalent circuit which functions to obtain an I-V characteristic curve. The circuit consists of 1 diode and 1 current source so it can be seen in the following picture.

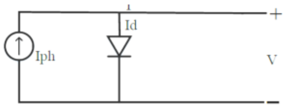

Figure 14. Solar PV Equivalent Circuit

d. Partial Shading Solar PV

Partial shading is a condition where some parts of the solar panel surface are covered from exposure to sunlight. This condition is caused by the presence of an object that blocks the solar cell. This can make the power generated by solar cells decrease. This decrease is also affected by the solar radiation received by the solar panels, thereby reducing the value of the resulting output current, as shown in the figure below [8] [9] [10]. Below is the equation for solar panel efficiency on the effects of partial shading.

$$I = I_{ph} - I_d\left(e^{\frac{qV}{k_B T}} - 1\right)$$

$$V = \frac{k_B T}{q}\ln\left(1 + \frac{I_{ph}}{I_d}\right)$$

$$P_{IN} = Radiance \cdot A$$

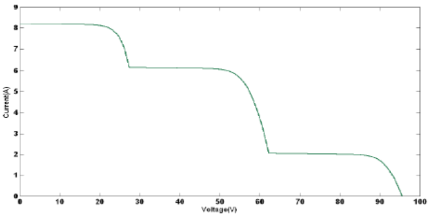

Figure 15. Equation and Partial Shading Curve

e. MPPT System

MPPT or Maximum Power Point Tracking is a technique for finding the maximum or highest power point. MPPT requires a DC-DC converter to work, because the way MPPT works is by changing the duty cycle to achieve MPP. There are many DC-DC converters that can be used, such as buck converters, boost converters, buck-boost converters, flyback converters, and others, depending on the needs of the users. The switch component on the DC-DC converter is set for the ON-OFF switching process using MPPT algorithms. MPPT requires a current sensor and a voltage sensor on the input side which are used as data for algorithm processing to obtain the duty cycle value [11].

f. Implementation of MPPT Serval Optimization Algorithm

This research introduces a new metaheuristic algorithm called Serval Optimization Algorithm (SOA), which mimics the natural behavior of servals in nature. The fundamental inspiration of SOA is the serval's hunting strategy, namely attacking selected prey and then hunting the prey by chasing. SOA implementation steps in two stages of exploration and exploitation. The proposed SOA approach is compared with the performance of twelve well-known metaheuristic algorithms to further evaluate it. The optimization results show that the SOA implementation of the CEC 2011 test suite and four engineering design challenges demonstrate the high efficiency of the proposed approach in handling real-world optimization applications. The proposed SOA approach is a population-based optimizer that is capable of providing suitable solutions to optimization problems by using the search power of its search agents. Servant prowling in nature has a similar approach to the agent-seeking mechanism of identifying optimal solutions. For this reason, from a mathematical point of view. Formation of the SOA population trying to reach the optimal solution [12].

$$X = \begin{bmatrix} X_1 \\ \vdots \\ X_i \\ \vdots \\ X_N \end{bmatrix}_{N\times d} = \begin{bmatrix} x_{1,1} & \cdots & x_{1,j} & \cdots & x_{1,d} \\ \vdots & \ddots & \vdots & ⋰ & \vdots \\ x_{i,1} & \cdots & x_{i,j} & \cdots & x_{i,d} \\ \vdots & ⋰ & \vdots & \ddots & \vdots \\ x_{N,1} & \cdots & x_{N,j} & \cdots & x_{N,d} \end{bmatrix}_{N\times d}, \qquad (1)$$

$$x_{i,j} = lb_j + r_{i,j}\cdot\left(ub_j - lb_j\right),\ i = 1, 2, \ldots, N \text{ and } j = 1, 2, \ldots, d, \qquad (2)$$

Step SOA Algorithm :

1. Input Information of Problem
2. Set a Population and amount of iteration
3. Calculation population matrix
4. Evaluation Object Function
5. Do Phase 1 (Exploration)

$$x_{i,j}^{P1} = x_{i,j} + r_{i,j} \cdot (P_j - I_{i,j} \cdot x_{i,j}),\ i = 1,2,\ \ldots,\ N \text{ and } j = 1,2,\ \ldots, d,$$

$$X_i = \begin{cases} X_i^{P1},\ F_i^{P1} < F_i \\ X_i,\ else \end{cases}$$

6. Do Phase 2 (Exploitation)

$$x_{i,j}^{P2} = x_{i,j} + \frac{r_{i,j} \cdot (ub_j - lb_j)}{t},\ i = 1,2,\ \ldots,\ N,\ j = 1,2,\ \ldots, d, \text{ and } t = 1,2,\ \ldots,\ T,$$

$$X_i = \begin{cases} X_i^{P2},\ F_i^{P2} < F_i, \\ X_i,\ else, \end{cases}$$

7. Repeat as set iteration, until find the best output

g. DC-DC Converter

The DC–DC converter can be seen in the picture below. Where Uin is the output voltage. D1 is a reversed blocking diode, and also functions to withstand/anticipate reverse current. Consists of L1, D2, L2, C1, C2. The capacitor switch consists of D3, D4, D5, C3, C4 and C5. R is the load resistance and uo is the output voltage of the converter. Q is Power Switch. This converter is an inverting DC-to-DC converter i.e. the polarity of the output voltage is reversed compared to the input supply. So, it is a negative output buck-boost converter [3] [4].

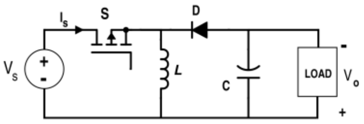

Figure 16. Buck Boost Converter Sequence

4. CONCLUSION

After carrying out testing and analysis in research on the design and implementation of MPPT solar panels - electric vehicles in fast varying partial shading conditions using the Serval Optimization algorithm, it can be concluded as follows:

1. Perform Quality of MPPT
   a. In the Non-Shading Condition Simulation Test, an average accuracy of 99,510% and an average tracking time of 0.490 seconds are obtained.
   b. In Partial Shading Condition Simulation Testing, Shading achieved an average accuracy of 99.958% and an average tracking time of 0.492 seconds.
   c. Comparison of the MPPT SOA method in the PSIM Comparison Test has a higher accuracy than the MPPT PSO and GWA methods, which is 99.95%. And has a faster tracking time of 0.55 seconds.
   d. In previous research, SOA is a new method for Optimizing Problem Solving which has quite good accuracy performance, which in this thesis research can be implemented in Solar PV Optimization to track MPPT.
2. Perform Quality of Converter & Battery
   a. In the State of Charge (SOC) Integration Test, with 12 test conditions, the Serval Optimization Algorithm (SOA) Method obtained an error value of 6.48% better than the GWO Method, so this method can be implemented in Battery and Solar PV based electric vehicles which has the potential for variations in partial shading to occur, due to mobile conditions.
   b. On Road Testing through 6 test conditions, using MPPT SOA can slow down the decrease in battery capacity by 16.24%.
   c. The application of Single Source on PV - MPPT - Converter can be implemented with an efficiency value of 76.86%, so it does not require 2 (two) sources.

6. REFERENCES

[1] Ade Febransyah,. “Predicting Purchase Intention towards Battery Electric Vehicles : A Case of Indonesian Market”, MDPI. World Electr. Veh. J. 2021, 12, 240, 2021

[2] Gede W., Rukmi H., Ida M "Metode Maximum Power Point Tracking pada Panel Surya: Sebuah Tinjauan Literatur", Techné Jurnal Ilmiah Elektroteknika Vol. 21 No. 2 Okt 2022 Hal 211 – 224, 2022
[3] Sreekumar, Arun R., "Maximum Power Point Tracking Of Pv Arrays Under Partial Shading Condition Using Sepic Converter"; IJRET eISSN: 2319-1163 pISSN: 2321-7308, 2014
[4] Masatosi U., Yasuke S., "PWM boost converter integrating differential power processing converter to enhance energy yield of photovoltaic panels under characteristic mismatch condition', IEEJ : Journal of Industry Application, 2020
[5] Geetha P,, Usha S, "Design and Analysis of Partial shading of the PV System Integrated with High-Frequency Inverter and Rectifier Operation for the Electric Vehicle", Journal of Physics: Conference Series ; IOP Publishing, 2022
[6] Kunjan Shinde, "Literature Review on Electric Bike", IJRMET, Vol. 7, Issue 1, 2017
[7] Qiang, Wang, Gao , Haiying, Liu, Wang, Du and Wei, "A State of Charge Estimation Approach for Lithium-Ion Batteries Based on the Optimized Metabolic EGM(1,1) Algorithm', MDPI, 2022
[8] Arfittariah, Wisyahyadi, "Efisiensi dari Solar panel terhadap Efek Partial shading di Wilayah Karang Joang", ELEMENTER Vol. 8, No. 1, 2022
[9] Dhamodhara S., Dhanalakshmi R., "Electric vehicle charging using roof top photovoltaic controlled with new hybrid optimization technique", IJEECS Vol. 26, No. 3, pp. 1227~1234, 2022
[10] Habib, Flah , Lobna , Alicia, Mosleh, Sherif, "A Comparison between Particle Swarm and GreyWolf Optimization Algorithms for Improving the Battery Autonomy in a Photovoltaic System", MDPI, Appl. Sci. 2021, 11, 7732, 2021
[11] Alamsyah Achmad, "Desain MPPT Pada Solar Cell Kondisi Partial Shading Berbasis Perturb and Observe (P&O)", Jurnal Ilmiah d'Computare Volume 6, 2016
[12] Mohammad D, Pavel T, "Serval Optimization Algorithm: A New Bio-Inspired Approach for Solving Optimization Problems", MDPI- Biomimeti, 2022
[13] Markus, Bernhard, Andreas, "Context-aware recommendations for extended electric vehicle battery lifetime", ELSEVIER, 2022
[14] Woongchul, "A Study on State of Charge and State of Health Estimation in Consideration of Lithium-Ion Battery Aging", MDPI, 2020
[15] Xiaosong, Le Xu, Xianke, and Michael Pecht3 "Battery Lifetime Prognostics", JOULE, 2020
[16] Qingxin, Zhuo, Jie, Yali, Lingzhi and Changming, "Closed-Loop Modeling to Evaluate the Performance of a Scaled-Up Lithium–Sulfur Battery in Electric Vehicle Applications", MDPI, 2021
[17] Karam, Murali, Member IAENG "Design, Analysis and Development of Solar Powered Electric Bi Cycle for domestic use", EJERS, 2019

LOGIC
Journal of Engineering Design and Technology
Vol. 24 No.2 July 2024 ; p. 63 - 68

p-ISSN : 1412-114X
e-ISSN : 2580-5649
http://ojs2.pnb.ac.id/index.php/LOGIC

EXPERIMENTAL STUDY OF THE UTILIZATION OF PINEAPPLE LEAF FIBER WITH THE ADDITION OF EPOXY RESIN TO THE TENSILE STRENGTH BREAK OF THE CONCRETE

Miftahul Hasanah[1], **Sartika Nisumanti**[2*], **Febryandi**[3]

1) Department of Civil Engineering, Faculty of Engineering, Indo Global Mandiri University, South Sumatra.

Corresponding email [1]:
sartika.nisumanti@uigm.ac.id

Abstract. In its development, many new concrete modifications were found, such as lightweight concrete, fiber concrete, polymer concrete, high-strength concrete and ultra-high-strength concrete. Epoxy resin can accelerate the hardening process of concrete because epoxy itself generates heat so that it helps accelerate hardening. In previous studies, the addition of areca nut shell fiber and 0.8% epoxy resin can increase the split tensile strength of concrete. Based on the description above, it is necessary to conduct research on the split tensile strength of concrete that combines a mixture of pineapple leaf fiber and epoxy resin. So this research uses pineapple leaf fiber and epoxy resin. Pineapple leaf fiber and epoxy resin are expected to be strength-enhancing materials that can produce concrete with more optimal split tensile strength. The purpose of this study was to determine the effect of the addition of epoxy resin and the percentage variation of pineapple leaf fiber on the split tensile strength of concrete and its comparison with normal concrete and to determine the percentage level of the addition of the most optimum pineapple leaf fiber to produce the maximum concrete split tensile strength test value among the planned variations. The method used in this research is experimental. From the results of the average split tensile strength test at 28 days, the epoxy resin variation of 0.8% achieved a strength of 2.87 MPa, the 0.15% variation achieved 2.37 MPa, and the 0.5% variation achieved 2.47 MPa

Keywords: Tensile Strength,Epoxy Resin, Pineapple Fiber

1. INTRODUCTION

Concrete has become a staple in infrastructure development in Indonesia [1]. Concrete is a basic form of life in modern society that has a function for development and construction components that have sturdy and durable properties whose mixture consists of aggregate (fine and coarse), water and cement which form a solid mass [2], [3]. The quality of concrete constituent materials affects the results of the concrete [4]. With good quality concrete, advantages are obtained, including being able to withstand compressive forces optimally. In addition, concrete also has many advantages, namely being able to withstand heavy loads, easy to shape as desired, and concrete stages against temperature [5], [6]. Concrete has weak tensile strength properties that result in concrete crumbling easily and breaking freely against changes in shape when the maximum stress has been reached [7].

In its development, many new concrete modifications have been found, such as lightweight concrete, fiber concrete, polymer concrete, high-strength concrete and ultra-high-strength concrete. One of the concrete that has been researched is polymer concrete. Polymer concrete is produced by reducing cement by adding an additive in the form of epoxy resin. Epoxy resin can accelerate the hardening process of concrete because epoxy itself generates heat so that it helps accelerate hardening [8]. In previous research, the addition of areca nutshell fiber and 0.8% epoxy resin can increase the split tensile strength of concrete [9]. The use of waste materials as additives in concrete has now been widely practiced in the world of construction industry. This aims to improve the mechanical properties of the concrete itself and reduce the amount of waste disposed of into the environment such as the use of pineapple leaf fibers. The use of pineapple leaf fibers can generally improve the quality and durability of concrete. However, the addition of pineapple leaf fiber must be added in the right percentage so that the desired concrete properties can be achieved [10].

Fiber is an additive that can be used to improve the brittle nature of concrete to become more ductile [11]. Fiber is a strong, stiff, and brittle material. The addition of fiber aims to increase tensile strength, increase resistance to cracking, and increase durability in concrete [12]. To obtain strong, smooth and soft fibers, it is necessary to select pineapple leaves that are mature enough and their growth is partially protected from sunlight [13]. Epoxy resin or generally in the market known as epoxy material is one of the most important type of polymer that comes from the thermoset group. Thermoset resin is a liquid polymer which is converted into a solid material by crosslink polymerization and also chemically, forming three-dimensional polymer chain formations. Epoxy resins are widely used for structural materials, so in concrete the use of epoxy resin can speed up the drying process, because epoxy generates heat and can help accelerate hardening [8]. Based on the description above, it is necessary to conduct research on the split tensile strength of concrete that combines a mixture of pineapple leaf fiber and epoxy resin. So this research uses pineapple leaf fiber and epoxy resin. Pineapple leaf fiber and epoxy resin are expected to be strength-enhancing materials that can produce concrete with more optimal split tensile strength.

2. METHODS

This research was conducted at the Laboratory of the Faculty of Engineering, Indo Global Mandiri University. This type of research is experimental research in the laboratory in the form of an experimental study on the use of pineapple leaf fiber with the addition of epoxy resin on the split tensile strength of concrete.

2.1. Materials

The materials used in this research were: fine aggregate, coarse aggregate, portland cement, water, pineapple leaf fiber and epoxy resin and hardener. Pineapple leaf fiber variation 0.15%, 0.5% and 1%, Variation of epoxy resin 0.8% to the volume of material weight.

2.2. Materials Testing

Material testing aims to obtain aggregate characteristic data so that it can be mixed in making concrete. Testing of this material consists of gradation analysis testing, mud content testing, water content testing and Specific Gravity and Absorption testing. In this case, the material testing reference refers to the National Standard Indonesia (SNI) and equipped with the American Society For Testing and Materials (ASTM).

2.3. Mix Design

This mix planning refers to SNI [14]. In this research, cylindrical test objects were used with dimensions of 10 cm x 20 cm. The mixture proportions for 1 cylinder in this study are in Table 1.

Tabel 1. Concrete Mix Proportion

Sample	Composition (kg)
Cement	0.963
Fine aggregate	0.999
Coarse aggregate	1.960
Water	0.424
0,15% Pineapple leaf fiber	0.006
0,5% Pineapple leaf fiber	0.021
1% Pineapple leaf fiber	0.043
Epoxy	0.026
Hardener	0.008

2.4. Concrete Compressive Strength

Testing the split tensile strength of concrete is carried out after curing using a Compression Testing Machine. In this study, testing the split tensile strength of concrete was carried out at the Indo Global Mandiri University Laboratory using SNI [15].

$$Fct = \frac{2P}{\pi.L.D} \qquad (1)$$

3. RESULTS AND DISCUSSION

The results discussed in this research are material testing, analysis of concrete characteristics such as cement water factor, slump test, and concrete split tensile strength test.

3.1 Material Testing Results

To analyze the characteristics of the fine aggregate, various tests were conducted, as shown below:

Table 2. Results of material testing

Material	Composition (Kg)	Spesifications	Test Results
Sieve Analysis	Coarse aggregate	≤ 8.5 %	4.29
	Fine aggregate	2.2- 3.2	2.26
Specific gravity	Coarse aggregate	≥ 2.5	2.64
	Fine aggregate	≥ 2.5	2.54
Absorption	Coarse aggregate	≤ 3%	1.84%
	Fine aggregate	≤ 3%	2.26%
Weight of contents	Coarse aggregate	≥ 1.4 Kg/m^3	1.462 Kg/m^3
	Fine aggregate	≥ 1.4 Kg/m^3	1.495 Kg/m^3
Sludge content	Fine aggregate	≤ 5.0 %	1.25 %
Organic matter content	Fine aggregate	Maks No. 3	No.3

3.2. Slump Test Result

Slump testing is done to be able to see the water in the concrete mixture either less, more or enough in this case the essence of this test is to know the consistency in the fresh concrete mixture [21]. from this study the results of testing the slump value can be seen in table 3.

Table 3. Slump Test

Sample	Slump value (cm)
Normal Concrete	12
BN ER 0,8%	12
BN ER 0,8% + SDN 0,15%	11,97
BN ER 0,8% + SDN 0,5%	11,95
BN ER 0,8% + SDN 1%	11,80

Table 4.9 can be concluded that the slump test obtained there are differences in the results of the slump value in each variation. The results of the slump test can be seen in graphical form in Figure 4.13.

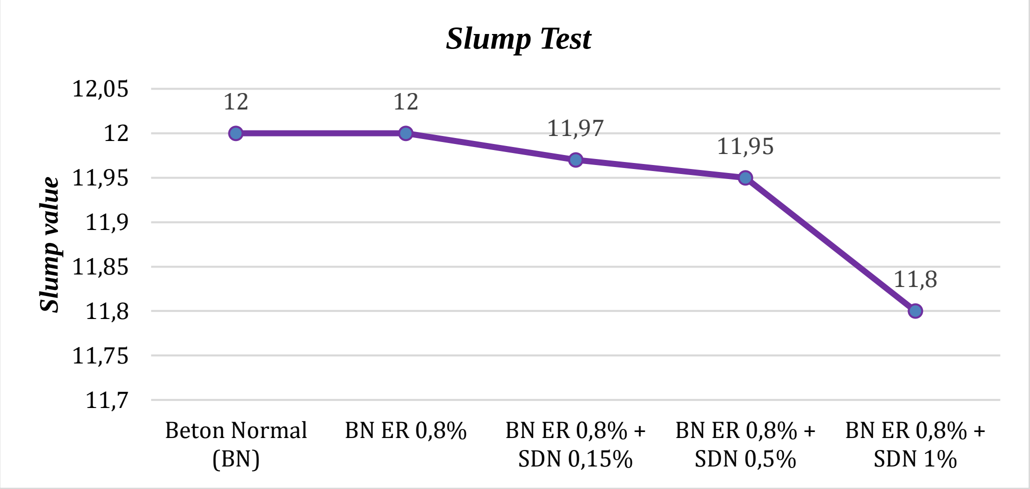

Figure 1. Slump Test

Based on SNI standards, the acceptable slump range value is 8-12 cm. Figure 4.13 shows that the slump value for normal concrete is 12 cm. With the addition of 0.8% epoxy resin, the slump value remains at 12 cm.

However, when 0.8% epoxy resin and pineapple leaf fiber at 0.15%, 0.5%, and 1% are added, the slump values are 11.97 cm, 11.95 cm, and 11.80 cm, respectively. The greater the percentage variation of epoxy resin and pineapple leaf fiber, the more viscous the concrete mixture. The results of the slump test have met the standards and can be used as a concrete mixture.

3.3 Concrete Tensile Strength Test Results

The concrete split tensile strength test in this study was conducted to determine the value of concrete split tensile strength (f't). The research samples made to conduct the test were 9 samples in each variation with a planned age of 7, 14 and 28 days with the aim of getting an overview of the split tensile strength test value of the concrete tested.

Table 4. Recapitulation of Concrete Compressive Strength

Concrete Mix Variations	7 days	14 days	28 days
Normal Concrete	1,78	1,91	2,29
BN ER 0,8%	2,04	2,25	2,87
BN ER 0,8% + SDN 0,15%	1,81	1,94	2,37
BN ER 0,8% + SDN 0,5%	1,88	2,23	2,47
BN ER 0,8% + SDN 1%	1,79	1,93	2,43

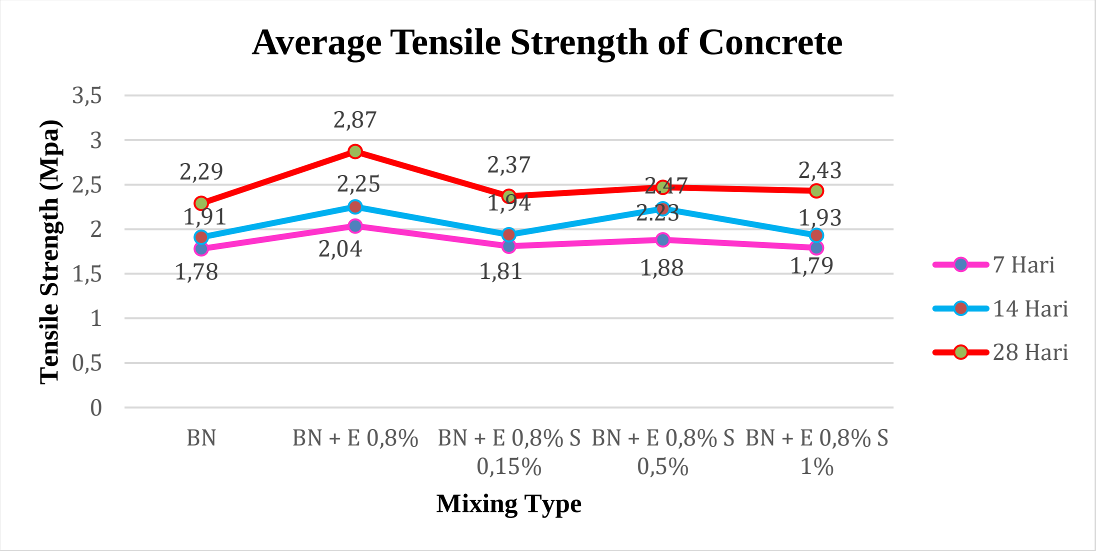

Figure 2. Graph of Recapitulated Tensile Strength of Concrete

Figure 4.20 shows a decrease in tensile strength for the pineapple leaf fiber concrete mixture compared to the concrete with 0.8% epoxy resin. This decrease occurs because the addition of fiber prevents the concrete mixture from binding effectively. The optimum value for the addition of fiber in the stirring process occurs in the addition of fiber with a variation of 0.5% with a resulting tensile strength of 2.47 MPa at the age of 28 days. And the optimum value of the entire variation tested is in concrete with the addition of epoxy resin 0.8% with a split tensile strength value obtained of 2.87 at the age of 28 days. The comparison value between normal concrete and 0.8% epoxy resin concrete has increased. Based on the results of the analysis, it is concluded that the split tensile strength value of concrete epoxy resin 0.8% is greater than normal concrete. The factor that influences the cause of the increase in the value of the split tensile strength of this concrete is the addition of epoxy resin to the volume of concrete. The percentage value of the comparison between 0.8% epoxy concrete and 0.8% epoxy concrete + pineapple leaf fiber variation 0.15% has decreased but still has a higher value than normal concrete. Based on the results of the analysis, it can be concluded that the split tensile strength value of epoxy concrete is greater than 0.15% variation pineapple leaf fiber concrete at the age of 7, 14, and 28 days. The factor that affects the cause of the decrease in 0.15% variation fiber concrete is the addition of pineapple leaf fiber which causes a decrease in the tensile strength of concrete. This is because the fiber addition process is not mixed evenly. The percentage value of the comparison between epoxy concrete with 0.8% + pineapple leaf fiber variation 0.5% and epoxy concrete 0.8% + pineapple leaf fiber variation 0.15% has increased. Based on the results of the analysis, it can be concluded that the split tensile strength value of 0.8% epoxy concrete with 0.5% variation pineapple leaf fiber is greater than 0.15% variation pineapple leaf fiber concrete at the age of 7, 14, and 28 days. The factor that affects the cause of the increase in 0.5% variation fiber concrete is the addition of more pineapple leaf fibers which causes an increase in the split tensile strength of concrete. The percentage value of the comparison between 0.8% epoxy concrete + 0.5% variation pineapple leaf fiber and 0.8% epoxy concrete + 1% variation pineapple leaf fiber has decreased. Based on the results of the analysis, it can be concluded that the split tensile strength value of 0.8% epoxy concrete with 0.5% variation pineapple leaf fiber is greater than 1% variation pineapple leaf fiber concrete at the age of 7, 14, and 28 days. Factors that influence the cause of the decrease in 1% variation fiber concrete are due to the addition of more pineapple leaf fibers which causes the concrete mixing process not to bind together so that there is a decrease in the tensile strength of the concrete.

4. CONCLUSION

Based on the results of research and analysis that have been carried out at the Concrete Laboratory at Indo Global Mandiri University, Palembang, the following conclusions can be drawn:

1. From the research results, concrete using additional materials of epoxy resin and pineapple leaf fiber has an effect on the splitting tensile strength of concrete so that there is an increase compared to the splitting tensile strength of normal concrete. However, the addition of pineapple leaf fiber to epoxy concrete is not of higher value than epoxy concrete. Because the addition of fiber causes a decrease in the split tensile strength value of the concrete, because the added material of pineapple leaf fiber does not bind each other to the concrete mixture.
2. The average split tensile strength test results at 28 days which occurred with the 0.8% epoxy resin variation were 2.87 MPa, the 0.15% variation was 2.37 MPa, the 0.5% variation was 2.47 MPa, the variation of 1% pineapple leaf fiber is 2.43 and in normal concrete it is 2.29 Mpa. So it was found that the optimum percentage level of added pineapple leaf fiber was 0.15% with an average split tensile strength value of 2.47 MPa. The optimum level, among the tested variations, is achieved with normal concrete containing 0.8% epoxy resin, which exhibits the highest splitting tensile strength value of 2.87 MPa.

5. REFERENCES

[1] Puspita. N., Hani, I. A., Fauzi.M. (2019). “The Effect of Ground Granulated Blast Furnace Slag (GGBFS) On Portland Cement Type II to Compressive strength Of High Quality Concrete”. *IOP Conference Series: Materials Science and Engineering.* doi:10.1088/1757-899X/830/2/022068.

[2] Cahyo, Y., Candra, A. I., Siswanto E, & Gunarto, A. (2020). The Effect of Stirring Time and Concrete Compaction on K200 Concrete Press Strength. *Journal of Physics: Conference Series*, 1569 (4).

[3] Puspita. N., Arti. Y., Febryandi. (2020). “Flexural Strength Analysis of Concrete with the Addition B3 Waste as an Additive to Ordinary Portland Cement”. Proceedings of the 4th Forum in Research, Science, and Technology. *Atlantis Press*.

[4] Tamayo, P,m Pacheco, J., Thomas, C., de Brito, J., & Rico, J. (2020). “Mechanical and durability properties of concrete with coarse recycled aggregate produced with electric arc furnace slag concrete”. *Applied Sciences (Switzerland*), vol. 10, no. 1.

[5] Maryanto, M., Winarto, S., & Krisnawati, L. D. (2018). “Studi Eksperimental Pengaruh Penambahan Limbah Kuningan Terhadap Kuat Tekan Beton Mutu K-225”. *Jurnal Manajemen Teknologi & Teknik Sipil*, 1(1), 76-90.

[6] Nisumanti, S. (2016). “Pengaruh Sika Viscocrete 3115 Untuk Memudahkan Pekerjaan (Workability) Beton Mutu Tinggi K.350 dan Kuat Tekan Beton”.*Jurnal um-palembang.* ac. *id*. Vol. 4, no. 3.

[7] Royani, I. F. (2014). Kajian kuat tekan, kuat tarik, kuat lentur, dan redaman bunyi pada panel dinding beton dengan agregat limbah plastik pet dan limbah serbuk kayu.

[8] Van Gemert, D., Czarnecki, L., Maultzsch, M., Schorn, H., Beeldens, A., Łukowski, P., & Knapen, E. (2005). Cement concrete and concrete–polymer composites: Two merging worlds: A report from 11th ICPIC Congress in Berlin, 2004. *Cement and Concrete Composites*, *27*(9-10), 926-933.

[9] Zulkarnain, F., & Nasution, B. I. P. (2022, July). PENGARUH PENAMBAHAN SERAT KULIT PINANG DAN EPOXY RESIN TERHADAP KUAT TARIK BELAH BETON. In *Prosiding Seminar Nasional Teknik UISU (SEMNASTEK)* (Vol. 5, No. 1, pp. 135-139).

[10] Irawan, T., Saloma and Idris, Y. (2019) ‘Mechanical Properties of Foamed Concrete with Additional Pineapple Fiber and Polypropylene Fiber’, Journal of Physics: Conference Series, 1198(8), pp. 1–8. Available at: https://doi.org/10.1088/1742- 6596/1198/8/082018.

[11] Amri, S. (2005). Teknologi Beton AZ. Yayasan John Hi-Tech Idetama, Jakarta.

[12] Era Rizky Hasanah, Agustin Gunawan, & Yuzuar Afrizal. 2017, Pengaruh Penambahan Serat Kulit Pinang Dan Serbuk Kayu Terhadap Kuat Tarik Belah Beton. Jurnal Inersia April 2017, Volume 9,Nomor 1.

[13] Hidayat, P. (2008). Teknologi pemanfaatan serat daun nanas sebagai alternatif bahan baku tekstil. Teknoin, 13(2), 31–35.

[14] SNI 03-2834-2000. (2000). SNI 03-2834-2000: “Tata Cara Pembuatan Rencana Campuran Beton Normal”. Sni 03-2834-2000, 1–34.

[15] Badan Standarisasi Nasional. 2002. SNI 03-2491-2002: Metode Pengujian Kuat Tarik Belah Beton. BSN. Bandung.

[16] Qubro, K. A., Saggaff, A., Saloma. (2021). “The Compressive Strength Of Fly Ash Foamed Concrete With Polypropylene Fiber”. *International Journal of Progressive Sciences Technologies,* vol. 29, no. 1, pp. 435–447.

LOGIC
Journal of Engineering Design and Technology
Vol. 24 No.2 July 2024 ; p. 69 - 78

p-ISSN : 1412-114X
e-ISSN : 2580-5649
http://ojs2.pnb.ac.id/index.php/LOGIC

COMPARATIVE ANALYSIS OF BILL OF QUANTITY STRUCTURE GEDUNG LAYANAN TERPADU RSUD BANGKINANG CITY USING CONVENTIONAL METHOD AND TEKLA STRUCTURE APPLICATION

Bayu Baskoro[1*], Zainuri[2], Shanti Wahyuni Megasari[3]

1) Program Studi Teknik Sipil, Fakultas Teknik, Universitas Lancang Kuning, Jl. Yos Sudarso km. 8 Rumbai, Pekanbaru, Telp. (0761) 52324

Corresponding email *) :
bybskr@gmail.com

Abstract. In accordance with PUPR Ministerial Regulation No. 22 of 2018, the use of Building Information Modeling (BIM) must be applied to non simple state buildings with criteria for a building area of more than 2000 m2 and more than 2 floors. Gedung Layanan Terpadu RSUD Kota Bangkinang has an area of 5,040 m^2 and has 4 floors but the calculations still use conventional methods. The aim of this study was to analyze the comparison of the bill of quantity (BOQ) of the Gedung Layanan Terpadu RSUD Bangkinang City using conventional methods and the Tekla Structure application. The integrated services building consists of 4 floors, starting from the basement floor, 1st floor, 2nd floor, 3rd floor and roof floor. The research method used was to carry out manual calculations using Microsoft Excel based on the working plans and modeling the building structure using the Tekla Structure application. From the results of the study it can be concluded that the volume of concrete using the conventional method was 3,193.5 m^3 while the calculation using the Tekla Structure application was obtained 3,175.5 m^3 where there was a difference of 18 m^3 or in a percentage of 0,56 % less than the conventional method. For iron volume, there is a difference in iron volume of 2,687.23 kg or 0,45 % less using the Tekla Structure application compared to conventional methods. The conclusion from this study is that the calculation of the bill of quantity using the conventional method is greater than using the Tekla Structure application.

Keywords : BIM, BOQ, Conventional, Tekla Structure

1. INTRODUCTION

Building is a physical form created by construction work that blend into place. These buildings are partially or completely above ground or in water, and serve as places where people carry out various activities, such as residential, religious, business, social, and cultural [1]. In the United States, BIM technology began to be used in various industries since 2003, and developed rapidly in the field of construction since 2007. However, in Indonesia, only a few companies implement it across all sectors. After BIM was used in Indonesia for several years, its use was considered not optimal despite the increasing development [2]. Building Information Modeling (BIM) is able to guarantee the integration of data or information such as synchronizing data between various stakeholders, automatic drawing generation, reports, design analysis, scheduling simulations, minimizing data redundancies, data loss and mistranslation of data into information [3].

Tekla BIM software has several benefits including precision and clarity of detail, automation of output and efficient and saving management costs [4]. The conventional calculation method in construction work is a method of calculating the volume of work that uses conventional software in the construction field such as Microsoft Excel for cost calculation, AutoCAD to make working drawings, Microsoft Project to create work schedules and SAP 2000 for structural analysis calculations. Unlike BIM, conventional methods are not integrated between one application and another [5]. Construction project management will generally include physical construction, cost, and time, material management as well as labor management [6]. Bill of quantity or volume of a job is to calculate the amount of volume of work in one unit. Volume is also referred to as cubication of work. The volume of work is calculated based on the bestek drawings of the building to be made. All parts or elements of construction present in the drawing must be calculated completely and meticulously to obtain an accurate and complete calculation of the volume of work [7].

The Ministry of PUPR as the Ministry in charge of Building made PUPR Minister Regulation No. 22 of 2018 concerning the Construction of State Buildings, it is stated that the use of Building Information Modelling (BIM) must be applied to non-simple buildings with criteria for an area above 2000 m² and above 2 floors [8]. One of the applications of Building Information Modelling (BIM) in the field of structure is Tekla Structure. This application can be used in making project structure drawings, structural analysis, project management, project control, and calculating work volume. This application itself can calculate the volume of work with better accuracy compared to conventional methods. The selection of the Integrated Service Building project at Bangkinang City Hospital is because this project still uses conventional methods which should have met the criteria required by PUPR Minister Regulation No. 22 of 2018 to perform calculations using BIM. With these considerations in mind, research is needed with the concept of Building Information Modeling using the Tekla Structure application to recalculate the structural aspect. The purpose of this study is to analyze the comparison of bill of quantity (BOQ) of the Integrated Service Building of Bangkinang City Hospital using conventional methods and Tekla Structure applications. According to Yuska, M. Y. I., (2021), in research comparing the conventional method and Tekla Structure application in calculating the structural cost of a hospital building, the aim was to compare the structural cost calculation of hospital construction. The results showed a 14.24% lower cost compared to the conventional method using Tekla Structure. This is because with BIM, modeling and data are integrated, and human errors or incorrect data input, which often occur in the conventional method, can be reduced [9].

2. METHODS

The research method used is to do manual calculations using Microsoft Excel based on working drawings of plans and modeling building structures using the Tekla Structure application which then the results of the two methods are compared to analyze the comparison of bill of quantity calculations at the Integrated Service Building of Bangkinang City Hospital. The conventional calculation method in construction work is a method of calculating the volume of work that uses conventional software in the construction field such as Microsoft Excel for cost calculation, AutoCAD to make working drawings, Microsoft Project to create work schedules and SAP 2000 for structural analysis calculations. Unlike BIM, conventional methods are not integrated between one application and another [5]. The Tekla Structure method enables the creation of accurate digital virtual models of buildings. Once completed, the resulting model contains the precise data and geometry required to complete the construction, fabrication, and procurement processes necessary to finish the building [3].

2.1.BIM Modeling

Before calculating the volume of structural work, 3D modeling was carried out using the Tekla Structure application, from which data on the volume of work in question was obtained. Here are the steps to find a volume using the Tekla Structure application:

a. Before modeling a Tekla Structure application, the first thing to do is to create a license for the application. The license obtained is in the form of a student version license by creating an account on the official Tekla Campus website and uploading the latest transcript as a condition for obtaining a license.

b. After obtaining the license, download and install the Tekla Structure application. Open the application so that the interface appears.

c. Grid settings are done by specifying the number, type and size of the x and y coordinates and setting them in the property pane on the right side of the application. The figure below shown the grid based on measurement between main structure. After setting up the grid, the interface will appear as shown in figure 1.

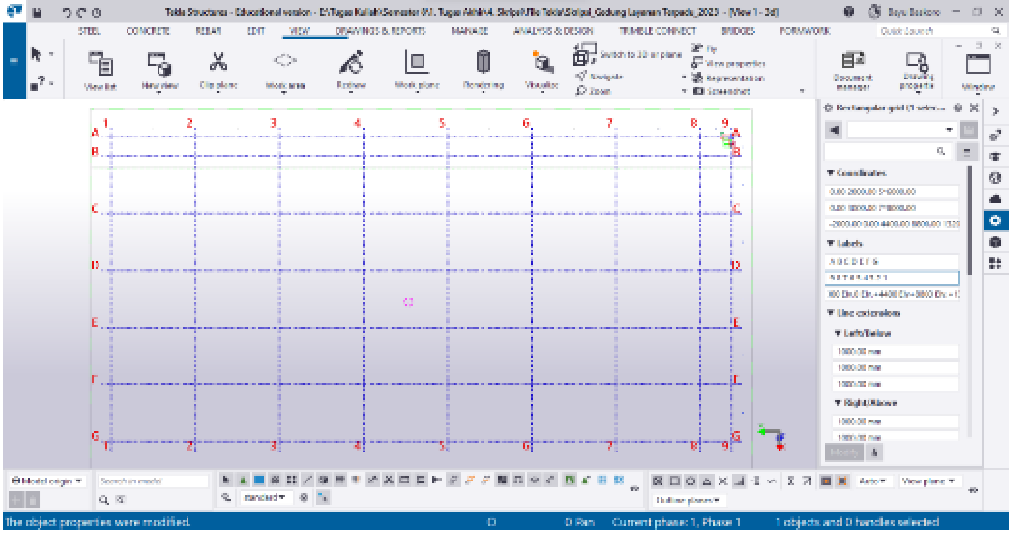

Figure 1. X and Y Axis Interface

d. Create a building axle line in the form of a Z-axis grid line for the vertical side of the building.

e. Create beam, tie beam and column modeling based on specified dimensions. The figure below shown the detail of beam, column and tie beam, by creating one detail work than it can be copied to each grid. It can be seen in figure 2.

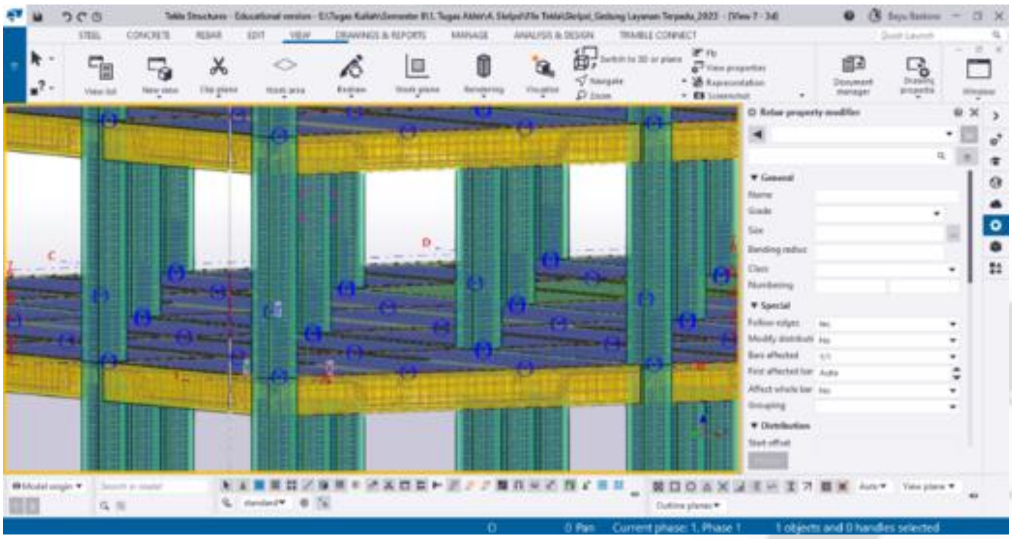

Figure 2. Beam, Tie Beam and Column Modelling View

f. Creating modeling of floor slabs based on specified dimensions. The figure below shown layout of concrete floor slab with the grid. It can be seen in figure 3.

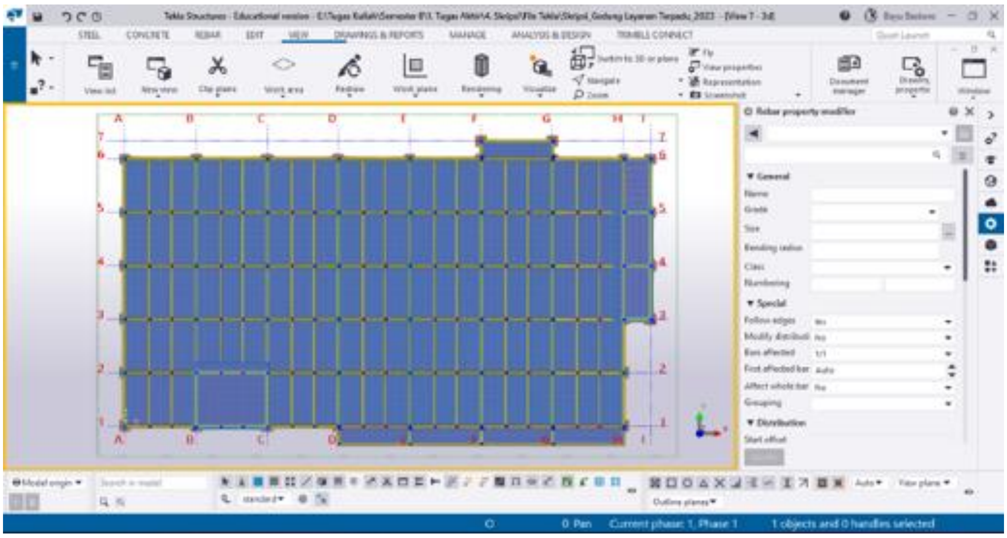

Figure 3. Floor Slab Modeling View

g. Make repeats on each element in detail and according to the reinforcement specified per element. The figure below shown reinforcement detail inside the concrete column, pedestal column, tie beam, pile cap and bored pile. It can be seen in figure 4.

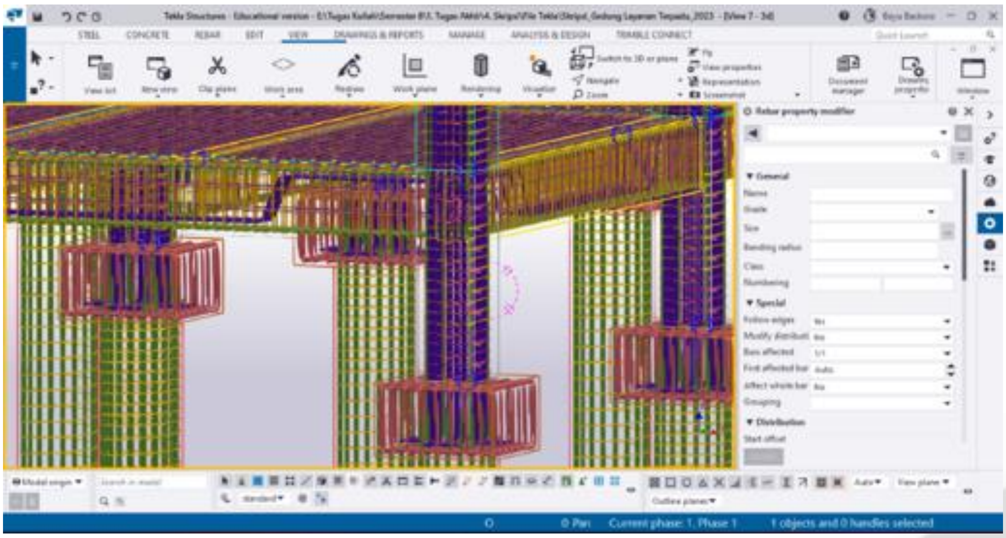

Figure 4. Floor Slab Modeling View

h. Create modeling output on the organizer menu on the manage menu tab of the application.

2.2. Volume Calculation

From the modeling carried out, it can directly calculate the volume using the Tekla Structure application, the results of the calculation will be compared with the bill of quantity using conventional methods. The calculation of the volume of work (bill of quantity) has several ways of calculation that are not the same as each other. One of the formulas for calculating the volume of work items in the conventional method is:

a. Volume for the length of the work item (m')
   (m') = Length
b. Volume for work item area (m^2)
   (m^2) = Length × Width (1)
c. Volume for cubication of work (m^3)

(m^3) = Length × Width × Height (2)

d. Volume for volume (ls, units, pieces)

In accordance with the agreement to Two sides

The flow chart in the study can be seen in figure 5.

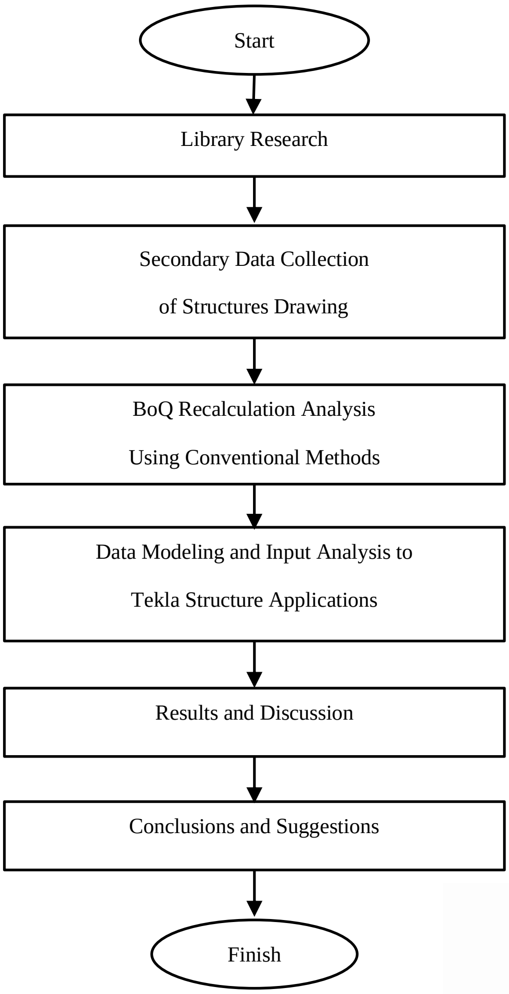

Figure 5. Research Flow Chart

3. RESULTS AND DISCUSSION

3.1 Bill of Quantity Comparison Analysis

After obtaining the bill of quantity results from both calculation methods using conventional methods and BIM methods with the Tekla Structure application, a comparative analysis of bill of quantity against each method will be carried out. The following is the result of the comparison of the bill of quantity of concrete work and ironing work at the Gedung Layanan Terpadu RSUD Bangkinang City.

Table 1. Comparative Analysis of Bill of Quantity Structur of Gedung Layanan Terpadu Basement Floor

No	Description	Unit	Volume		Deviation	Percentage
			Conventional	Tekla Structure		
(1)	(2)	(3)	(4)	(5)	(6) = (4) - (5)	(7) = (6)/(4)×100
I	Structural Work					
1	Basement Structure Work					
	a Bored Pile Foundation Work P1 dia. 80 cm					
	1) Concrete Work F'c = 25 MPa	m³	407,15	405,00	2,15	0,53%
	2) Reinforcement Work	kg	46.033,76	44.744,00	1.289,76	2,80%
	b Foundation Work Pile Cap P1 size 120×120×70 cm					
	1) Concrete Work F'c = 25 MPa	m³	54,43	54,00	0,43	0,79%
	2) Reinforcement Work	kg	7.679,53	7.776,00	-96,47	1,26%
	c Pedestal Column Work size 200×60×60 cm					
	1) Concrete Work F'c = 25 MPa	m³	38,88	37,80	1,08	2,78%
	2) Reinforcement Work	kg	13.227,18	13.480,00	-252,82	1,91%
	d S1 Tie Beam Work Elv. -6.40 size 40×70 cm					
	1) Concrete Work F'c = 25 MPa	m³	181,66	181,60	0,06	0,04%
	2) Reinforcement Work	kg	41.385,70	41.181,00	204,70	0,49%
	e S2 Tie Beam Work Elv. -6.40 size 30×60 cm					
	1) Concrete Work F'c = 25 MPa	m³	70,56	70,60	-0,04	0,06%
	2) Reinforcement Work	kg	13.596,24	13.819,00	-222,76	-1,64%
	f K1 Column Work Elv. -6.40 - ± 0.00 size 60×60 cm					
	1) Concrete Work F'c = 25 MPa	m³	124,42	124,20	0,22	0,17%
	2) Reinforcement Work	kg	32.627,04	31.914,00	713,04	-2,19%
	g Concrete Floor Work Elv. -6.40 thk = 12 cm					
	1) Concrete Work F'c = 25 MPa	m³	117,19	117,90	-0,71	-0,61%
	2) Reinforcement Work	kg	16.468,93	16.600,00	-131,07	0,80%
Total Volume of Basement Floor Concrete		m³	994,29	991,10	3,19	0,32%
Total Volume of Basement Floor Reinforcement		kg	171.018,39	169.514,00	1.504,39	0,88%

The results of the bill of quantity comparison on the basement floor Gedung Layanan Terpadu structural work which can be seen in table 1 show that there is a difference of 3.19 m³ or in percentage of 0.32% in concrete work where conventional calculations obtained results of 994.29 m³ while the volume of concrete using the Tekla structure application obtained results of 991.10 m³. In iron work there is a difference of 0.88% or 1,504.39 kg. There was a significant difference in pile cap iron work where a difference of 2.8% was obtained, while in concrete work the largest difference was in pedestal column work with a difference of 2.78%.

Table 2. Comparative Analysis of Bill of Quantity Structure of Gedung Layanan Terpadu 1st Floor

No	Description	Unit	Volume		Deviation	Percentage
			Conventional	Tekla Structure		
(1)	(2)	(3)	(4)	(5)	(6) = (4) - (5)	(7) = (6)/(4)×100
I	Structural Work					
2	First Floor Structure Work					
	a B1 Beam Work size 40×70 cm					
	1) Concrete Work F'c = 25 MPa	m³	181,66	181,60	0,06	0,04%
	2) Reinforcement Work	kg	41.385,70	41.181,00	204,70	0,49%
	b B2 Beam Work size 30×60 cm					
	1) Concrete Work F'c = 25 MPa	m³	70,56	70,60	-0,04	0,06%
	2) Reinforcement Work	kg	13.596,24	13.819,00	-222,76	-1,64%
	c Concrete Floor Work Elv. ±0.00 thk = 12 cm					
	1) Concrete Work F'c = 25 MPa	m³	208,97	204,90	4,07	1,95%
	2) Reinforcement Work	kg	28.463,56	27.840,00	623,56	2,19%
	d K1 Column Work ± 0.00 - +4.40 size 60×60 cm					
	1) Concrete Work F'c = 25 MPa	m³	85,54	86,40	-0,86	1,01%
	2) Reinforcement Work	kg	23.808,92	24.102,00	-293,08	-1,23%
	e Kp Column Work ± 0.00 - +3.70 size12×12 cm					
	1) Concrete Work F'c = 25 MPa	m³	6,34	5,80	0,54	8,52%
	2) Reinforcement Work	kg	537,14	532,40	4,74	0,88%
Total Volume of First Floor Concrete		m³	553,07	549,30	3,77	0,68%
Total Volume of First Floor Reinforcement		kg	107.791,57	107.474,40	317,17	0,29%

From table 2, it can be seen that the results of the bill of quantity comparison on the structural work of the 1st floor Gedung Layanan Terpadu show that there is a difference of 3.77 m³ or in a percentage of 0.68% smaller using the Tekla Structure application. In the iron work, there was a difference of 0.29% or 317.17 kg smaller using the Tekla Structure application. In the calculation of the 1st floor bill of quantity, there is a significant difference in the floor plate work with a difference of 623.56 kg or in percentage of 2.19%.

Table 3. Comparative Analysis of Bill of Quantity Structure of Gedung Layanan Terpadu 2nd Floor

No	Description	Unit	Volume		Deviation	Percentage
			Conventional	Tekla Structure		
(1)	(2)	(3)	(4)	(5)	(6) = (4) - (5)	(7) = (6)/(4)×100
I	Structural Work					
3	Second Floor Structure Work					
	a B1 Beam Work size 40×70 cm					
	1) Concrete Work F'c = 25 MPa	m^3	181,66	181,60	0,06	0,04%
	2) Reinforcement Work	kg	41.385,70	41.181,00	204,70	0,49%
	b B2 Beam Work size 30×60 cm					
	1) Concrete Work F'c = 25 MPa	m^3	70,56	70,60	-0,04	0,06%
	2) Reinforcement Work	kg	13.596,24	13.819,00	-222,76	-1,64%
	c Concrete Floor Work Elv. +4.40 thk = 12 cm					
	1) Concrete Work F'c = 25 MPa	m^3	208,97	204,90	4,07	1,95%
	2) Reinforcement Work	kg	28.463,56	27.840,00	623,56	2,19%
	d K1 Column Work +4.40 - +8.80 size 60×60 cm					
	1) Concrete Work F'c = 25 MPa	m^3	85,54	86,40	-0,86	1,01%
	2) Reinforcement Work	kg	23.808,92	24.102,00	-293,08	-1,23%
	e Kp Column Work +4.40 - +8.10 size 12×12 cm					
	1) Concrete Work F'c = 25 MPa	m^3	5,43	5,80	-0,37	6,72%
	2) Reinforcement Work	kg	460,40	423,20	37,20	8,08%
	Total Volume of Second Floor Concrete	m^3	552,17	549,30	2,87	0,52%
	Total Volume of Second Floor Reinforcement	kg	107.714,83	107.365,20	349,63	0,32%

The results of the bill of quantity comparison on the 2nd floor of the Gedung Layanan Terpadu structural work which can be seen in table 3 show that there is a difference of 2.87 m^3 or in a percentage of 0.52% smaller using the Tekla Structure application. In the iron work, there was a difference of 0.32% or 349.63 kg smaller using the Tekla Structure application. In the calculation of the 2nd floor bill of quantity, the smallest difference is in the concrete work for B1 blocks with a difference of 0.04%.

Table 4. Comparative Analysis of Bill of Quantity Structure of Gedung Layanan Terpadu 3rd Floor

No	Description	Unit	Volume		Deviation	Percentage
			Conventional	Tekla Structure		
(1)	(2)	(3)	(4)	(5)	(6) = (4) - (5)	(7) = (6)/(4)×100
I	Structural Work					
4	Third Floor Structure Work					
	a B1 Beam Work size 40×70 cm					
	1) Concrete Work F'c = 25 MPa	m^3	192,84	191,40	1,44	0,74%
	2) Reinforcement Work	kg	43.528,31	43.627,00	-98,69	-0,23%
	b B2 Beam Work size 30×60 cm					
	1) Concrete Work F'c = 25 MPa	m^3	70,56	70,60	-0,04	0,06%
	2) Reinforcement Work	kg	13.596,24	13.819,00	-222,76	-1,64%
	c Concrete Floor Work Elv. +8.80 thk = 12 cm					
	1) Concrete Work F'c = 25 MPa	m^3	208,97	204,90	4,07	1,95%
	2) Reinforcement Work	kg	29.252,68	29.082,00	170,68	0,58%
	d K1 Column Work +8.80 - +13.20 size 60×60 cm					
	1) Concrete Work F'c = 25 MPa	m^3	85,54	86,40	-0,86	1,01%
	2) Reinforcement Work	kg	23.808,92	24.102,00	-293,08	-1,23%
	e Kp Column Work +8.80 - +12.50 size 12×12 cm					
	1) Concrete Work F'c = 25 MPa	m^3	5,86	6,20	-0,34	5,79%
	2) Reinforcement Work	kg	496,51	483,40	13,11	2,64%
	Total Volume of Third Floor Concrete	m^3	563,77	559,50	4,27	0,76%
	Total Volume of Third Floor Reinforcement	kg	110.682,66	111. 113,40	-430,74	-0,39%

From table 4, it can be seen that the comparison of bill of quantity on the 3rd floor of the Gedung Layanan Terpadu structure work shows that there is a difference of 4.27 m^3 or in a percentage of 0.76% smaller using the Tekla Structure application. In iron work, there is a difference of 0.39% or 430.74 kg greater using the application of Tekla Structure. The largest difference occurred in the volume of iron work column K1 with a difference of

293.08 kg or in a percentage of 1.23% greater using the application of Tekla Structure compared to conventional methods.

Table 5. Comparative Analysis of Bill of Quantity Structure of Gedung Layanan Terpadu Rooftop Floor

No	Description	Unit	Volume		Deviation	Percentage
			Conventional	Tekla Structure		
(1)	(2)	(3)	(4)	(5)	(6) = (4) - (5)	(7) = (6)/(4)×100
I	Structural Work					
5	Rooftop Floor Structure Work					
	a B1 Beam Work size 40×70 cm					
	1) Concrete Work F'c = 25 MPa	m^3	209,92	208,40	1,52	0,72%
	2) Reinforcement Work	kg	47.383,72	46.572,00	811,72	1,71%
	b B2 Beam Work size 30×60 cm					
	1) Concrete Work F'c = 25 MPa	m^3	70,56	70,60	-0,04	0,06%
	2) Reinforcement Work	kg	13.596,24	13.819,00	-222,76	-1,64%
	c Concrete Floor Work Elv. +13.20 thk = 12 cm					
	1) Concrete Work F'c = 25 MPa	m^3	220,15	219,40	0,75	0,34%
	2) Reinforcement Work	kg	29.548,60	29.227,00	321,60	1,09%
	d Concrete Floor Work Elv. +15.70 thk = 12 cm					
	1) Concrete Work F'c = 25 MPa	m^3	16,62	14,50	2,12	12,76%
	2) Reinforcement Work	kg	1.992,53	2.034,70	-42,17	2,12%
	e K1 Column Work +13.20 - +13.70					
	1) Concrete Work F'c = 25 MPa	m^3	3,96	4,40	-0,44	11,11%
	2) Reinforcement Work	kg	571,54	532,10	39,44	6,90%
	f K1 Column Work +13.20 - +15.70					
	1) Concrete Work F'c = 25 MPa	m^3	9,00	9,00	0 ,00	0,00%
	2) Reinforcement Work	kg	1.529,93	1.491,00	38,93	-2,54%
Total Volume of Rooftop Floor Concrete		m^3	530,20	526,30	3,90	0,74%
Total Volume of Rooftop Floor Reinforcement		kg	94.622,57	93.675,80	946,77	1,00%

The results of the bill of quantity comparison on the structural work of the rooftop floor Integrated Service Building which can be seen in table 4.21 show that there is a difference of 3.9 m^3 or in a percentage of 0.74% smaller using the Tekla Structure application. In the iron work, there was a difference of 0.56% or 946.77 kg smaller using the Tekla Structure application. The following is a recapitulation of the results of the total difference in bill of quantity comparison in the structure of the Gedung Layanan Terpadu RSUD Bangkinang City which can be seen in table 5.

Table 6. Total Difference Analysis Bill of Quantity Comparison of Gedung Layanan Terpadu Structures

Description	Unit	Volume		Deviation	Percentage
		Conventional	Tekla Structure		
Total Volume of Basement Floor Concrete	m^3	994,29	991,10	3,19	0,32%
Total Volume of Basement Floor Reinforcement	kg	171.018,39	169.514,00	1504,39	0,88%
Total Volume of First Floor Concrete	m^3	553,07	549,30	3,77	0,68%
Total Volume of First Floor Reinforcement	kg	107.791,57	107.474,40	317,17	0,29%
Total Volume of Second Floor Concrete	m^3	552,17	549,30	2,87	0,52%
Total Volume of Second Floor Reinforcement	kg	107.714,83	107.365,20	349,63	0,32%
Total Volume of Third Floor Concrete	m^3	563,77	559,50	4,27	0,76%
Total Volume of Third Floor Reinforcement	kg	110.682,66	111.113,40	-430,74	-0,39%
Total Volume of Rooftop Floor Concrete	m^3	530,20	526,30	3,90	0,74%
Total Volume of Rooftop Floor Reinforcement	kg	94.622,57	93.675,80	946,77	1,00%
Total Volume of Concrete	m^3	3.193,50	3.175,50	18,00	0,56%
Total Volume of Reinforcement	kg	591.830,03	589.142,80	2687,23	0,45%

From table 6 it can be seen that for concrete work using conventional methods it produces a concrete volume of 3,193.5 m^3 and calculations using the Tekla Structure application produce a concrete volume of 3,175.5 m^3 obtained the difference for concrete work is 18 m^3 or in percentage of 0.56% greater in conventional calculations compared to using the Tekla Structure application. For the results of ironing work, conventional methods produce iron volumes of 591,830.03 kg while calculations using the Tekla Structure application obtained results of 589,142.8 kg obtained a ratio of 2,687.23 kg or in percentage of 0.45% greater in conventional calculations than using the Tekla Structure application. The largest difference occurred in the calculation of concrete volume on the 3rd floor with a difference of 0.76% while the smallest difference was found in the volume of concrete on the 2nd floor with a difference of 0.52% smaller using the application of Tekla Structure compared to conventional methods.

3.1 Discussion

From the results of the comparison analysis above, there are several work items that have significant differences, this is because in the calculation process using the Tekla structure application, there are some items that do not produce perfect details, for example in bored pile ironing, in conventional calculations, bored pile ironing can be calculated in close detail using the provisions in SNI 03-2847, where the calculation for overlap or bending, can adjust to the applicable provisions, while in the calculation of the tekla structure application, how to apply the iron form is limited to the provisions of the application itself and there are some items that cannot follow the provisions of SNI 03-2847, causing this ironing calculation to be greater than conventional methods.

From table 6 it can be seen that for concrete work at the Gedung Layanan Terpadu RSUD Bangkinang City using conventional methods produces a concrete volume of 3,193.5 m^3 while calculations using the Tekla Structure application produce a concrete volume of 3,175.5 m^3 so that the comparison of the two methods for concrete work is 18 m^3 or in a percentage of 0.56% greater in conventional calculations compared to using applications Tekla structure. This is because calculations using the Tekla structure application produce more detailed volumes than the results of conventional methods whose calculations are still done manually and only based on working drawings [10].

Calculations using the Tekla Structure application can be said to be a shorter calculation process if you understand how to use it compared to conventional methods which require more time in interpreting work drawings and making them units of work volume needed. In addition, the use of BIM applications to calculate the volume of work is said to be very efficient, because the applications have been integrated with each other so that when there is a design change in planning, the calculation of work volume automatically follows the existing changes so that it eliminates the time required to identify differences due to changes [9].

4. CONCLUSION

The comparative analysis of the Bill of Quantity (BoQ) volume for the Gedung Layanan Terpadu RSUD Bangkinang City using conventional methods and the Tekla Structure application reveals several key insights:

1. Efficiency and Accuracy
   The Tekla Structure application demonstrates higher efficiency in terms of calculation speed and the ability to automatically adjust volumes with design changes. This integration reduces the time required for recalculations and enhances the accuracy of the BoQ by minimizing human error inherent in manual calculations.
2. Floor-by-Floor Analysis
   The differences in volume calculations varied across different floors. For example, the largest difference in concrete volume was observed on the 3rd floor, with a 0.76% discrepancy, while the smallest difference was on the 2nd floor at 0.52%. Similarly, reinforcement work volume differences varied, with significant differences observed in specific elements like the pile cap and pedestal column work.
3. Overall Implications
   Despite the differences, the overall volume calculations using both methods are relatively close, suggesting that either method can be reliable depending on the project's requirements. However, the use of the Tekla Structure application is recommended for its higher efficiency, ability to integrate design changes seamlessly, and potential to reduce manual calculation errors.

In conclusion, while conventional methods provide slightly higher volume calculations for both concrete and reinforcement work, the Tekla Structure application offers significant advantages in efficiency and integration, making it a preferable choice for modern construction projects. Further research with multiple case studies is suggested to validate these findings and enhance the robustness of the conclusions

5. REFERENCES

[1] Peraturan Pemerintah Pekerjaan Umum dan Perumahan Rakyat, 2018, Undang - Undang No. 28, Tentang Bangunan Gedung Negara, Jakarta.

[2] Fakhruddin, Parung, H., Tjaronge, M. W., Djamaluddin, R., Irmawaty, R., Amiruddin, A. A., Djamaluddin, A. R., Harianto, T., Muhiddin, A. B., Arsyad, A. and Nur, S. H., 2019, Sosialisasi Aplikasi Teknologi Building Information Modeling (BIM) pada Sektor Konstruksi Indonesia, Jurnal Fakultas Teknik Vol. 2 No.

2, pp. 112–119, ISSN: 2654-2781.
[3] Nugraha, D. B., 2020, Analisis Inventarisasi Pemodelan Komponen Superstructure Jembatan Cikujang Menggunakan BIM Tekla Structure, Journal of Chemical Information and Modeling, Vol. 53 No. 9,
[4] Minawati, R., Chandra, H. P. dan Nugraha, P., 2017, Manfaat Penggunaan Software Tekla Building Information Modeling (BIM) Pada Proyek Design-Build, Dimensi Utama Teknik Sipil, Vol. 4 No. 2, pp. 8–15, ISSN: 2656-3312
[5] Berlian, C. A., Adhi, R. P., Hidayat, A. dan Nugroho, H., 2016, Daya Manusia Antara Metode Building Information Modeling (BIM) dan Konvensional, Jurnal Karya Teknik Sipil, Vol. 5 No. 2, pp. 220-229, ISSN: 2597-2674.ISSN: 1689-1699.
[6] Putri, F. F., 2019, Evaluasi Anggaran Biaya Struktur dan Arsitektur Menggunakan Metode Building Information Modeling (BIM) (Studi Kasus: Gedung Integrated Laboratory For Science Policy And Communication IsDB Uneversitas Jember), Tugas Akhir, Program Studi S1 Teknik Sipil Universitas Jember, Jember.
[7] Siswanto, A. dan Salim, M., 2019, Manajemen Proyek, Pillar Nusantara, Semarang.
[8] Peraturan Pemerintah Pekerjaan Umum dan Perumahan Rakyat, 2018, Undang - Undang No. 22, Tentang Bangunan Gedung Negara, Jakarta.
[9] Yuska, M. Y. I., 2021, Perbandingan Penggunaan Metode Konvensional dan Aplikasi Tekla Structure Pada Perhitungan Anggaran Biaya Struktur Atas Gedung RSUD Selasi Pangkalan Kerinci, Tugas Akhir, Program Studi Teknik Sipil Universitas Lancang Kuning, Pekanbaru.
[10] Arianti, T. P., Sucita, I. K. dan Yanuarini, E., 2022, Perbandingan BoQ Tulangan Antara Metode Konvensional dengan BIM Apartemen "X", Vol. 21 No. 1, pp. 28-35, ISSN: 1412-2782.

LOGIC
Journal of Engineering Design and Technology
Vol. 24 No.2 July 2024 ; p. 79 - 86

p-ISSN : 1412-114X
e-ISSN : 2580-5649
http://ojs2.pnb.ac.id/index.php/LOGIC

SIMULATION OF THE INFLUENCE OF FIBER VOLUME FRACTION AND FIBER ORIENTATION ON THE STRENGTH OF POLYESTER COMPOSITE REINFORCED WITH GLASS FIBER IN BENDING STRENGTH

1. Jurusan Teknik Mesin, Politeknik Negeri Malang, Jl Soekarno Hatta No.09, Malang, Indonesia

Corresponding email [1] :
fakhruddin91@polinema.ac.id

Muhammad Fakhruddin [1*], Imam Mashudi [1], Nurlia Pramita Sari [1], Nicky Suwandhy Widhi Supriyanto [1]

Abstract. Fiber-reinforced composites can be classified into two parts, namely short fiber composites and long fiber composites. Long fibers are generally stronger than short fibers. Long fiber (continuous fiber) is more efficient in laying than short fiber but short fiber is easier to lay than long fiber. Fiber length affects the processability of the fiber composite. Judging from the theory, long fibers can transfer the load and stress from the stress point to the other fiber. In this research, we simulated the effects of volume fraction and fiber orientation in glass fiber-reinforced polyester composites on bending strength to examine the effect of each parameter on the mechanical properties of glass fiber composites. The mechanical properties of the composite were tested using the three-point bending and tensile testing methods. The study expects to find variations in mechanical properties with changes in the glass fiber volume fraction and fiber orientation. In this study, it is planned to function in a relevant environment, the components in this study must be able to operate properly and have been well integrated with prototype manufacturing that has been tested as a test tool function. Notably, the pinnacle of the bending test, measuring 170.41 MPa, was achieved at the specific combination of a 0.5 Fiber Volume Fraction and the 0-90° fiber orientation.
.

Keywords : Volume Fraction, Composite, Fiberglass, Simulation, Three-point Bending

1. INTRODUCTION

Composite is a material that consists of two or more different types of materials combined together to create desired properties that may not be achievable by each individual material separately. When combined, these materials form a new system that often has superior characteristics compared to the individual materials that constitute it. Composites are commonly used in various applications such as the automotive industry, aviation, construction, and others, to combine the strength and other properties of various materials into a stronger or more resilient system against various loads or conditions [1].

Composites exhibit a range of mechanical properties depending on the specific materials utilized and their arrangement within the composite structure [2] [3]. High strength, characteristic of composites, refers to their capacity to endure stress without deformation or fracture. Similarly, their high stiffness makes them resistant to deformation under external forces, maintaining structural integrity and dimensional stability [4]. Designed for toughness, composites can absorb energy and deform before fracturing, offering notable impact resistance and averting catastrophic failure. Moreover, their exceptional fatigue resistance enables them to endure cyclic loading without developing cracks or failures over time. With engineered resistance to creep, composites can withstand long-term exposure to mechanical stress, ensuring prolonged structural stability and durability. Notably, their low density and lightweight nature, in contrast to conventional materials like metals, render composites advantageous in weight-sensitive applications, particularly in aerospace, automotive, marine, and construction industries. Understanding these mechanical properties is essential for the efficient design, engineering, and selection of composite materials tailored to various industrial applications.

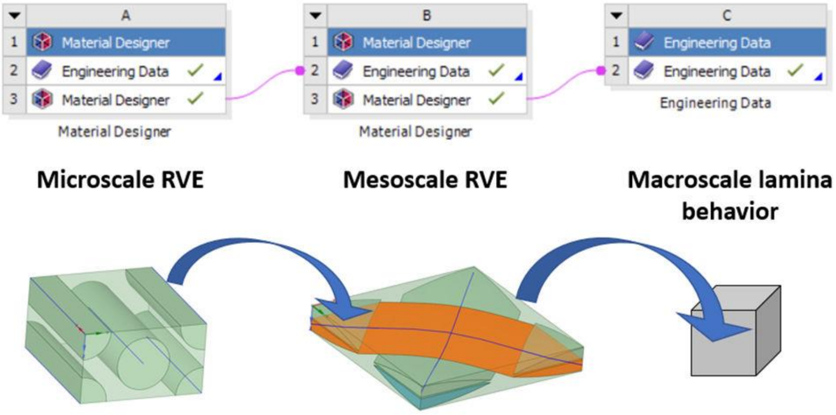

Figure 1. Material designer in simulation process

In composite materials analysis, Representative Volume Elements (RVEs) at different scales characterize material properties. The microscale RVE captures detailed microstructural features such as fibers and the matrix, determining effective properties like stiffness and strength from these interactions, considering fiber arrangement, orientation, and fiber-matrix interfaces. The mesoscale RVE averages these microstructural details into a more homogenized form while retaining some features, bridging the gap between microscale details and macroscale behavior. It considers phenomena like fiber bundles, local variations in fiber volume fraction, and defects, helping to understand the overall mechanical behavior of the composite without detailed modeling of every interaction. At the macroscale, the composite is treated as a continuum with averaged properties derived from microscale or mesoscale analyses, focusing on the behavior of composite laminates under various loading conditions. This scale is used for structural analysis and design, using homogenized properties for effective stiffness, strength, and thermal properties of the composite lamina. Each scale—microscale, mesoscale, and macroscale—provides essential insights for accurately predicting and designing composite materials.

Composite simulation refers to the process of using software or mathematical methods to predict and understand the behavior of composites under various conditions. Such simulations may involve microstructural analysis, the distribution of matrix and fibers, as well as the influence of the environment on the composite performance. The goal of composite simulation is to understand how factors such as fiber volume fraction, fiber orientation, matrix used, and environmental conditions can affect the mechanical and physical properties of the composite material. By utilizing simulations, engineers can optimize composite designs for specific applications, estimate the material's lifespan, and analyze the composite's response to different mechanical loads [5]. Composite simulation is crucial in saving costs and time during the product development process, as it allows for careful evaluation before physical production takes place [6].

Mohammad Alfian Ilmy et al. (2018) conducted research on the Influence of Glass Fiber Volume Fraction on the Mechanical Properties of Glass Fiber/Epoxy Composites Using the Variation Method. The findings from the conducted research revealed that increasing the vacuum pressure enhanced the mechanical properties of the glass fiber mat 300/epoxy AB777 composite. The highest tensile strength of the composite, reinforced with glass fiber mat 300 and epoxy matrix AB777, was observed at a 50% fiber volume fraction with a pressure of 0.5 bar, measuring 138.18 MPa, while the lowest was exhibited by the 30% volume fraction at 0.2 bar, measuring 96.60 MPa. Tensile strength increased with the increment of the fiber volume fraction. The highest impact resistance of the fiberglass mat 300/epoxy AB777 composite was found at the optimal 45% volume fraction with a pressure of 0.5 bar, measuring 0.1913 J/mm², whereas the lowest was observed in the 30% volume fraction at 0.2 bar, measuring 0.0979 J/mm². Impact resistance began to decrease at the 50% fiber volume fraction.

Alamsyah et al. (2020) conducted research on the Influence of Resin and Catalyst Ratio on the Tensile Strength of Fiberglass-Polyester Composites for Shipbuilding Materials. The research findings indicated that fiberglass-polyester composites with a 0.5% catalyst content exhibited a tensile strength of 4.85 kgf/mm², elongation of 2.43%, and an elastic modulus of 2.26 kgf/mm². Composites with a 1% catalyst content demonstrated a tensile strength of 5.02 kgf/mm², elongation of 1.71%, and an elastic modulus of 2.96 kgf/mm². Additionally, composites with a 1.5% catalyst content displayed a tensile strength of 5.49 kgf/mm², elongation of 1.97%, and an elastic modulus of 3.07 kgf/mm². Composites with a 2% catalyst content showed a tensile strength of 4.97

kgf/mm², elongation of 1.62%, and an elastic modulus of 3.11 kgf/mm². The tensile strength of the fiberglass-polyester composite increased from 0.5% to 1.5% catalyst content and decreased at 2% catalyst content. Moreover, the highest tensile strength for the fiberglass-polyester composite was obtained at a resin composition of 100% and a 1.5% catalyst content, with a tensile strength of 5.49 kgf/mm², elongation of 1.97%, and an elastic modulus of 3.07 kgf/mm².

This research distinguishes itself from previous studies by focusing on the detailed simulation of how fiber volume fraction and fiber orientation influence the bending strength of polyester composites reinforced with glass fibers, using ANSYS software. This study systematically examines a wider range of volume fractions, including less commonly explored ones, providing a deeper understanding of the impact of varying fiber content on bending strength and potentially identifying optimal volume fractions that balance strength and material efficiency. It also investigates a broader spectrum of fiber orientations, including off-axis angles often overlooked in earlier works, offering a thorough understanding of the anisotropic nature of composites and their bending performance under different alignments. By employing advanced ANSYS simulation techniques, including detailed finite element models that capture microstructural interactions between fibers and the matrix, the research offers new insights into composite behavior under bending loads. These simulations deliver more reliable predictions of bending strength through refined meshing techniques and enhanced material modeling, improving computational efficiency and accuracy over existing methods. Additionally, this research uniquely integrates the effects of both fiber volume fraction and fiber orientation within the same study, revealing synergistic effects and guiding more effective composite design strategies. Overall, the study advances the understanding of polyester composites with glass fibers by addressing unexplored volume fractions and orientations and utilizing innovative ANSYS simulation methods to enhance design accuracy and efficiency [2], [3], [7].

In this study, the researchers utilized ANSYS software to conduct macro-scale simulations of glass fiber composites reinforced with polyester resin. The investigation involved the deliberate variation of volume fractions, as represented by distinct layers, and the manipulation of fiber orientation. The evaluation of the mechanical properties was achieved through a comprehensive simulation process employing the three-point bending test method, which allowed for a detailed understanding of the material's structural behavior and performance under specific loading conditions.

2. METHODS

The variables utilized in this study are categorized as follows: the independent variable, the dependent variable, and the controlled variables. The independent variable, representing the volume fraction of glass fibers to polyester resin, was set at 25%, 30%, 35%, 45%, and 50%, while the fiber weave orientation was designated as (0^o,90^o) and (45^o,135^o). On the other hand, the dependent variable, specifically the maximum stress during both tensile testing and 3-point bending, was determined based on the variations of the independent variables [8]. Throughout the research, several parameters were meticulously controlled to ensure consistency and reliability. These encompassed maintaining a consistent loading speed for both tensile and bending tests, applying loading precisely at the midpoint of the specimens during bending, ensuring uniform dimensions of the test specimens in accordance with ASTM standards, and utilizing E-glass fibers for the woven fiber components.

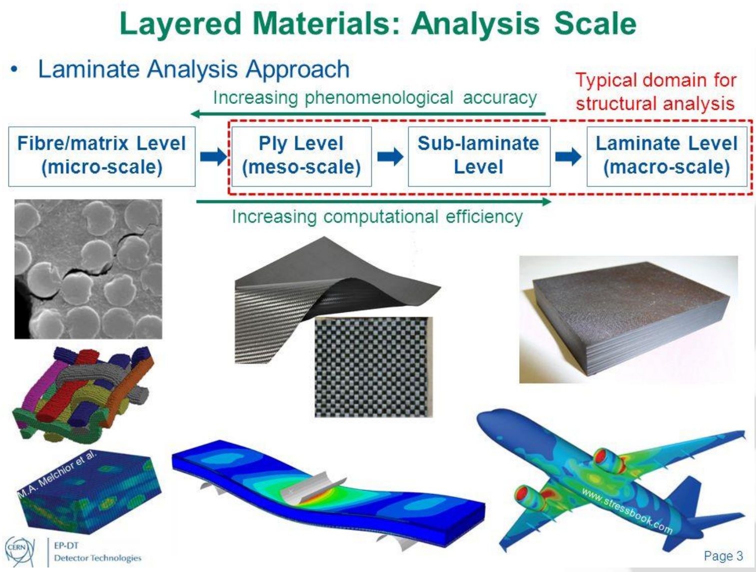

Layered Materials: Analysis Scale

- Laminate Analysis Approach

Typical domain for structural analysis

Increasing phenomenological accuracy

Fibre/matrix Level (micro-scale) → Ply Level (meso-scale) → Sub-laminate Level → Laminate Level (macro-scale)

Increasing computational efficiency

Figure 2. Simulation using ANSYS Software

Three-point bending simulation with ANSYS is a numerical method used to model and analyze the behavior of a test specimen when subjected to loading at three points of contact. This simulation provides an in-depth understanding of how the test specimen will respond under bending forces, applicable to various materials including composites and metals. The process begins with the creation of a geometric model of the test specimen, defining its dimensions and geometry to suit the research requirements [7]. Material properties such as elastic modulus and bending strength are then assigned to the specimen. Boundary conditions are set to specify the loading and support points, typically involving the application of pressure to the specimen's center with support from two contact points. ANSYS is employed to simulate the specimen's behavior, calculating its response to the bending load in terms of stress and strain. Subsequently, the results are evaluated to derive essential data such as maximum stress and strain. Furthermore, the simulation can be optimized and analyzed with variations in parameters, enabling a comprehensive understanding of how different factors influence the bending behavior. Overall, 3-point bending simulation with ANSYS serves as a valuable tool for comprehending and examining the response of test specimens under bending conditions, facilitating applications in material research and structural engineering.

The bending strength of a material is typically described by the bending stress (σ) it can withstand before it yields or breaks. The bending stress in a beam or any other structure under bending can be calculated using the bending strength equation, also known as the flexure formula. For a simple case of a beam with a rectangular cross-section experiencing a three-point bending test, the bending strength equation is:

$$\sigma = 3FL / (2bd)^2 \qquad (1)$$

where:

σ : bending stress
F : tapplied force at the midpoint
L : span length between the supports
b : width of the beam
d : depth of the beam

A meticulous and detailed series of steps are involved. First, the process commences with the precise creation of a geometric model that corresponds to the specimen under analysis. Following this, the accurate selection of appropriate materials and the determination of their mechanical properties become the subsequent crucial steps. The mesh generation also requires careful attention to ensure that the element resolution adequately represents the stress changes occurring within the test specimen during the bending process. The precise establishment of boundary conditions, including the application of loads at specific points in accordance with the 3-point bending test standards, is also a critical aspect of this modeling. Once the simulation is executed, result analysis becomes a pivotal stage in comprehending the test specimen's response to the bending load, encompassing stress, strain, and deformation that occur. The evaluation and interpretation of these simulation results allow for a profound understanding of the mechanical characteristics of the material under investigation, providing better insight into how the material will behave under bending conditions.

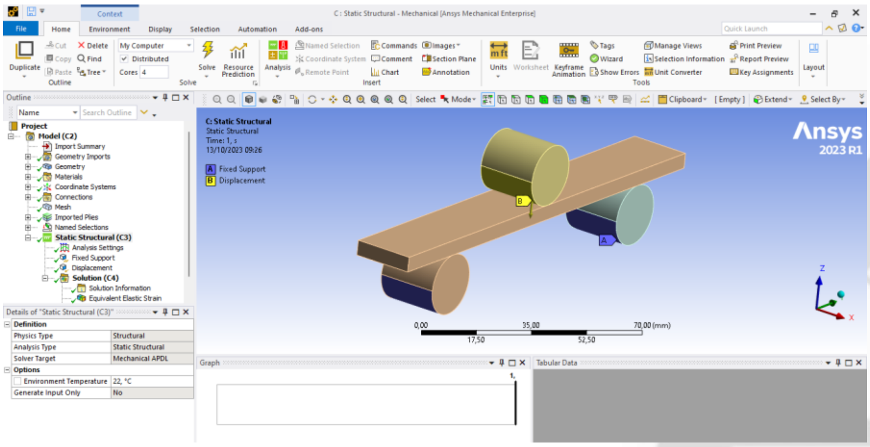

My Computer
☑ Distributed
Cores 4

Details of "Static Structural (C3)"

Definition	
Physics Type	Structural
Analysis Type	Static Structural
Solver Target	Mechanical APDL
Options	
☐ Environment Temperature	22, °C
Generate Input Only	No

Figure 3. ANSYS Simulation Control for 3-point Bending Case using Static Structural Analysis

The parameters in the solver window for the bending test are tailored to specific configurations. The simulation model is intentionally simplified to align with the prescribed requirements of the ASTM D790 test specimen's designated observation length.

3. RESULTS AND DISCUSSION

3.1 Composite with Fiber orientation 45°-135°

This research offers a comprehensive and detailed investigation into critical parameters influencing composite materials' mechanical performance. This study sets itself apart by systematically exploring a wide range of fiber volume fractions (FVF) and fiber orientations, areas often not exhaustively studied in combination. Utilizing advanced ANSYS simulation techniques, it examines the impact of varying FVF, including less commonly explored ranges, to provide a deeper understanding of how fiber content affects bending strength. Additionally, the research investigates a broad spectrum of fiber orientations, including off-axis angles, to uncover nuanced effects on bending performance [9], [10]. This approach offers a thorough understanding of the anisotropic nature of composites and their behavior under different loading conditions. By leveraging refined meshing techniques and detailed finite element models, the ANSYS simulations provide precise predictions of failure mechanisms and mechanical properties, offering new insights and improvements over traditional empirical methods [11], [12]. The findings of this study have significant practical implications, guiding the design of more efficient and stronger composite materials by identifying optimal combinations of FVF and fiber orientation, ultimately contributing to innovations in composite manufacturing and application

The classification of results obtained from the bending tests conducted on composites with a fiber orientation of 45°-135° demonstrates a clear trend. The data from the graph highlights that the maximum tensile strength is achieved at higher ratios of fiber volume fractions. Notably, the highest recorded value from the bending test for the specific 45° -135° fiber orientation is 149.95 MPa.

Table 1. Bending Stress on Fiber Orientation 45° and 90°

Fiber Volume Fraction	Bending Stress (MPa) 45°	Bending Stress (MPa) 90°
0,25	73,968	85,11
0,30	85,927	99,209
0,35	99,025	114,35
0,40	113,57	130,85
0,45	130,08	149,25
0,50	149,95	170,41

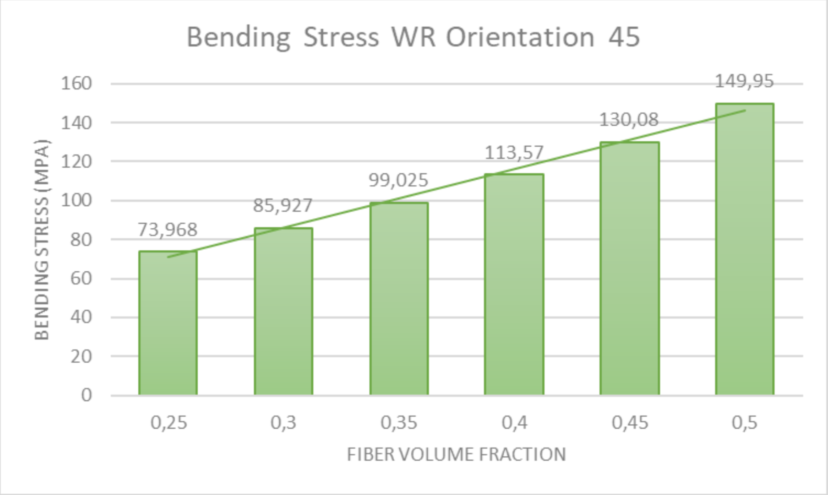

Figure 4. Graph Results of the Bending Test in the 45°-135° fiber orientation

In the results of the 3-point bending test, where the specimen had a configuration of a 50% fiber volume fraction and a 45° fiber orientation, a noteworthy outcome emerged. The test revealed a maximum stress of 149.95 MPa, signifying the point at which the material exhibited its highest resistance to deformation under the applied load. This impressive result was complemented by a corresponding strain value of 1.54%, indicating the extent of deformation or elongation experienced by the material during the bending test. These findings provide valuable insights into the mechanical behavior of the composite in this specific configuration and orientation, shedding light on its strength and flexibility under bending conditions shown in figure 5.

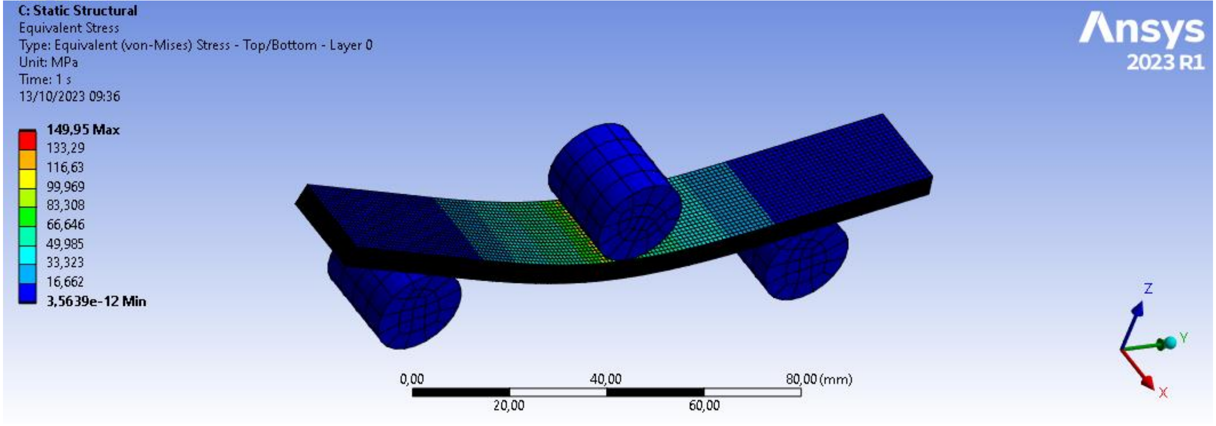

Figure 5. Simulation Results of the Bending Test (0.5-45°)

3.2 Composite with Fiber orientation 0°-90°

The findings represent the outcome of categorizing the results obtained from the bending tests conducted on composites with a fiber orientation of 0°-90°. An analysis of the accompanying graph reveals a clear trend: the highest tensile strength is achieved at higher ratios of fiber volume fractions. Specifically, the bending test for the 0o-90o fiber orientation yielded an impressive value of 170.41 MPa, indicating the material's remarkable resistance to deformation under the applied load. These results provide valuable insights into the mechanical characteristics of the composite in this particular orientation, underscoring its exceptional strength when subjected to bending forces.

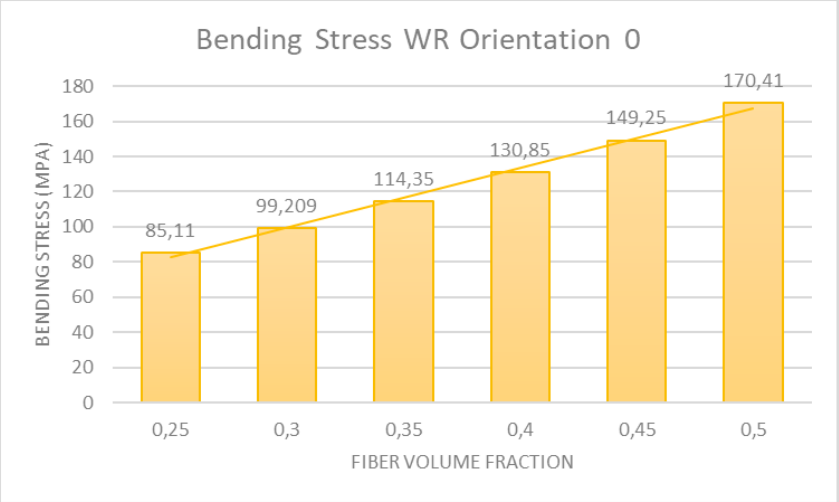

Figure 6. Graph Results of the Bending Test in the 0°-90° fiber orientation.

The 3-point bending test conducted on the specimen with a 50% fiber volume fraction and a 0° fiber orientation demonstrated a significant outcome. It exhibited a notable maximum stress of 170.41 MPa, reflecting the material's impressive ability to withstand bending forces. Additionally, the corresponding strain value of 1.5% indicated the extent of deformation experienced by the material during the bending test. These results provide valuable insights into the specimen's mechanical performance under specific bending conditions, highlighting its robustness and resilience as shown as Figure 7.

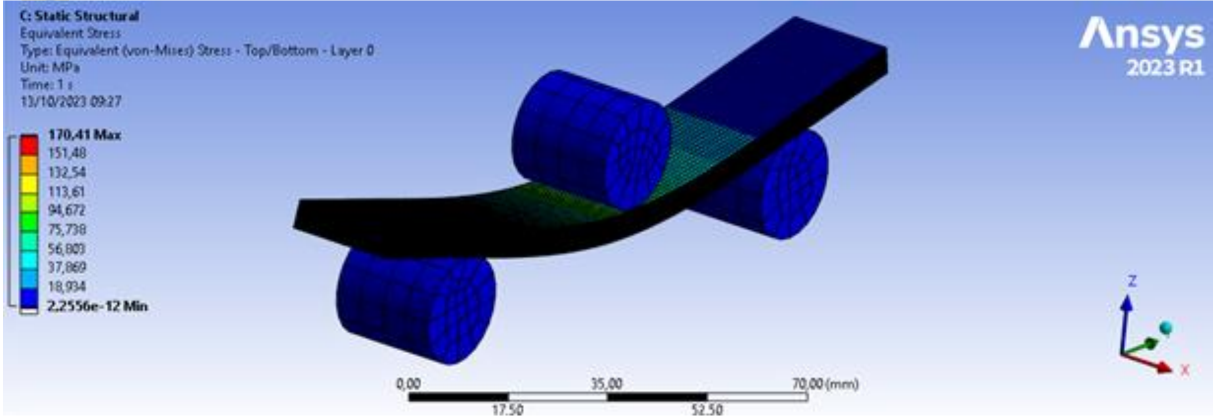

Figure 7. Simulation Results of the Bending Test in the 0°-90° fiber orientation

4. CONCLUSION

The rule of mixtures is a basic principle used to estimate the properties of a composite material based on the properties of its constituents. For composite materials, the rule of mixtures provides a way to predict the overall mechanical properties of the composite based on the properties of the individual components and their volume fractions. The rule assumes that the composite's properties are directly related to the volume fractions and properties of its constituents.

The flexural strength of the E-glass/polyester composite exhibits an upward trend with an increase in the ratio of the fiber volume fraction. Additionally, it is evident that the maximum value recorded during the bending test consistently aligns with the woven fiber orientation in the 0-90° direction. Notably, the pinnacle of the bending test, measuring 170.41 MPa, was achieved at the specific combination of a 0.5 Fiber Volume Fraction and the 0-90° fiber orientation. These observations highlight the significant influence of both fiber volume fraction and fiber orientation on the overall mechanical behavior of the composite, emphasizing their crucial roles in enhancing the composite's resistance to bending forces.

5. ACKNOWLEDGEMENT

Gratitude is extended to the Center for Research and Community Service (P3M) at the State Polytechnic of Malang for their generous funding support derived from the Budget Implementation List (DIPA) Number: SP DIPA-023.18.2.677606/2023, which significantly contributed to the successful execution of this research endeavor and the subsequent publication of this journal.

6. REFERENCES

[1] M. Fakhruddin, M. Maskuri, E. Faizal, B. Pranoto, H. Wicaksono, and H. I. Firmansyah, "Pengaruh Perlakuan Permukaan Pengikatan Terhadap Sifat Mekanik Komposit Serat Kaca Dengan Laminasi Almunium," *Jurnal Energi dan Teknologi Manufaktur (JETM)*, vol. 4, no. 02, pp. 27–32, 2021, doi: 10.33795/jetm.v4i02.79.

[2] N. K. Romli *et al.*, "The behavior of Aluminium Carbon/Epoxy fibre metal laminate under quasi-static loading," *IOP Conf Ser Mater Sci Eng*, vol. 257, no. 1, 2017, doi: 10.1088/1757-899X/257/1/012046.

[3] Hariharan E and Santhanakrishnan R, "Experimental Analysis of Fiber Metal Laminate With Aluminium Alloy for Aircraft Structures," © *International Journal of Engineering Sciences & Research Technology*, no. 5, 2016, doi: 10.5281/zenodo.50999.

[4] M. Chandrasekar, M. R. Ishak, M. Jawaid, Z. Leman, and S. M. Sapuan, "An experimental review on the mechanical properties and hygrothermal behaviour of fibre metal laminates," *Journal of Reinforced Plastics and Composites*, vol. 36, no. 1, pp. 72–82, 2017, doi: 10.1177/0731684416668260.

[5] X. P. Zhang, T. H. Yang, J. Q. Liu, X. F. Luo, and J. T. Wang, "Mechanical properties of an Al/Mg/Al trilaminated composite fabricated by hot rolling," *J Mater Sci*, vol. 45, no. 13, pp. 3457–3464, 2010, doi: 10.1007/s10853-010-4373-z.

[6] D. G. dos Santos, R. J. C. Carbas, E. A. S. Marques, and L. F. M. da Silva, "Reinforcement of CFRP joints with fibre metal laminates and additional adhesive layers," *Compos B Eng*, vol. 165, no. November 2018, pp. 386–396, 2019, doi: 10.1016/j.compositesb.2019.01.096.

[7] R. Kulkarni, A. Mache, and A. Salve, "A Review : Fiber Metal Laminates (FML ' s) - Manufacturing , Test methods and Numerical modeling," *International Journal of Engineering Technology and Sciences (Ijets)*, vol. 6, no. 1, pp. 71–84, 2016.

[8] M. Fakhruddin, I. Mashudi, M. Muzaki, H. Iman Firmansyah, B. Pranoto, and H. Wicaksono, “Pengaruh Fraksi Volume Terhadap Sifat Mekanis Komposit Forged Fiberglass Metode Compression Mould,” vol. 05, no. 02, pp. 35–40, 2022, [Online]. Available: http://jetm.polinema.ac.id/

[9] A. S. Moghadam and F. Omidinasab, “Assessment of hybrid FRSC cementitious composite with emphasis on flexural performance of functionally graded slabs,” *Constr Build Mater*, vol. 250, Jul. 2020, doi: 10.1016/j.conbuildmat.2020.118904.

[10] Q. Tarrés *et al.*, “Flexural properties and mean intrinsic flexural strength of old newspaper reinforced polypropylene composites,” *Polymers (Basel)*, vol. 11, no. 8, 2019, doi: 10.3390/polym11081244.

[11] D. Chen, G. Sun, M. Meng, X. Jin, and Q. Li, “Flexural performance and cost efficiency of carbon/basalt/glass hybrid FRP composite laminates,” *Thin-Walled Structures*, vol. 142, pp. 516–531, Sep. 2019, doi: 10.1016/j.tws.2019.03.056.

[12] U. Lohbauer, T. Von der Horst, R. Frankenberger, N. Krämer, and A. Petschelt, “Flexural fatigue behavior of resin composite dental restoratives,” *Dental Materials*, vol. 19, no. 5, pp. 435–440, Jul. 2003, doi: 10.1016/S0109-5641(02)00088-X.

LOGIC
Journal of Engineering Design and Technology
Vol. 24 No.2 July 2024 ; p. 87 - 92

p-ISSN : 1412-114X
e-ISSN : 2580-5649
http://ojs2.pnb.ac.id/index.php/LOGIC

INVESTIGATION OF TEMPERATURES AND HOLDING TIMES ON HIGH-STRENGTH LOW-ALLOY STEEL FOR TANK TRACK LINKS

Selly Septianissa [1], Komang Widhi Widantha [2], Muhamad Waldi[3]

1) Department of Mechanical Engineering, Widyatama University, Bandung, Indonesia
2) Department of Mechanical Engineering, Politeknik Negeri Bali, Badung, Bali, Indonesia
3) Department of Metallurgical Engineering, Jenderal Achmad Yani University, Bandung, Indonesia

Corresponding email [1] :
selly.septianissa@widyatama.ac.id

Abstract. In Indonesia, the reliance on foreign countries for military components persists, including tank track links which are crucial for combat vehicles. These components require mechanical properties such as wear resistance and toughness to ensure high safety standards. High Strength Low Alloy (HSLA) steel is used, necessitating precise composition and appropriate heat treatment processes. This study varied compositions and heat treatments to achieve desired properties, producing prototypes with five predetermined compositions. The heat treatment process involves initially heating the samples to 860°C for 30 minutes for uniformity, followed by various treatments including quenching in oil, normalizing, and multiple cycles of quenching with tempering at different temperatures and durations to refine microstructure and adjust hardness of the alloy. Results showed optimal mechanical properties in composition no. 4 after normalizing with a blower, achieving a hardness of 31 HRC. This research aimed to optimize mechanical performance during operational conditions through variations in temperatures and holding times.
.

Keywords : Tracklink tank, High Strength Low Alloy, Heat Treatment,

1. INTRODUCTION

The High Strength Low Alloy (HSLA) steel is a specialized alloy designed to enhance mechanical properties and corrosion resistance compared to low-carbon steels [1], [2]. Unlike steels with specific chemical compositions, HSLA steel focuses primarily on optimizing its mechanical characteristics [3]. Typically containing carbon levels ranging from 0.05% to 0.25%, HSLA steel exhibits excellent formability and weldability [4]-[6]. It incorporates additional alloying elements such as manganese (up to 2%), along with trace amounts of copper, nickel, niobium, nitrogen, vanadium, chromium, molybdenum, titanium, aluminum, and calcium. These elements are carefully chosen to achieve a microstructure of ferrite and pearlite, with finely dispersed carbides embedded within the ferritic matrix [7]-[8]. The reduction of pearlite phase through grain refinement enhances the material's strength, with an increase in yield strength ranging from 250 to 590 megapascals (36,000 to 86,000 psi) [9].

Due to its high strength and toughness, HSLA steel requires approximately 25-30% more energy for shaping compared to low-carbon steel [10], [11]. The addition of elements such as copper, silicon, nickel, chromium, and phosphorus aims to improve the alloy's corrosion resistance [12], [13]. Conversely, zirconium and calcium are included to mitigate sulfide impurities, crucial for enhancing formability in this sensitive type of steel [14]. The distinctive properties of formability and impact strength are evident in longitudinal and transverse grain testing, where bending often induces fractures near grain boundaries under tensile stress. Therefore, controlling sulfide content is crucial to maintain the mechanical properties of HSLA steel throughout its service life [15], [16].

HSLA steel represents a significant advancement in metallurgical engineering, leveraging precise alloy design and processing techniques to achieve a balanced combination of strength, formability, and corrosion resistance [17]-[20]. However, despite the well-documented benefits of HSLA steel, there is a gap in understanding how different temperatures, and holding times impact the mechanical properties of HSLA steel, particularly for critical applications such as tank track links. Optimizing these parameters is crucial because tank track links must withstand extreme operational conditions, requiring precise control over the steels hardness. Understanding these properties not only facilitates the development of durable structural components but also underscores the importance of optimizing alloy composition and production methods to meet stringent performance requirements in various industrial applications. This study aims to fill this gap by systematically investigating the effects of temperatures and holding times on the mechanical properties of HSLA steel, thereby enhancing its performance and durability in military applications.

2. METHODS

The research Reverse material analysis involves the systematic evaluation and modification of materials to achieve altered properties while maintaining the base material's structural integrity. The goal of this approach is to enhance specific material properties to meet desired functional requirements. The dimensions of the material are shown in Figure 1. In this study, High Strength Low Alloy (HSLA) steel serves as the base material. Y-block samples, conforming to JIS G5502 standards, are cast and subsequently sectioned into smaller pieces for ease of handling during heat treatment. Samples are specifically taken from the edges, critical for evaluating performance in tank track applications. The composition of the HSLA steel alloy was examined using a spectrometer to ensure accurate determination of the elemental makeup. This analysis allowed for precise measurement of key elements, such as carbon, manganese, chromium, silicon, and others, which are essential for understanding how the alloy's composition affects its properties and performance.

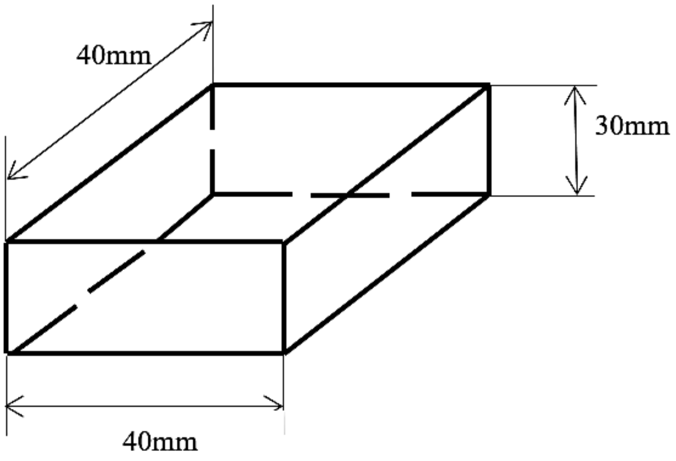

Figure 1. Dimensions of the test specimen

The heat treatment begins with a solution treatment phase at 860°C, with a 30-minute holding period to ensure uniformity. Following this, each of the five compositions undergoes a series of heat treatment processes including quenching (using oil), normalizing, quenching + tempering 600oC 30 minute, quenching + tempering 600°C 60 minute, quenching + tempering 400°C 30 minute, quenching + tempering 400°C 60 minute . Quenching using oil is applied to rapidly cool the material and create a harder microstructure. Normalizing performed to refine the grain structure and relieve internal stresses. Tempering is used to optimize hardness while retaining sufficient toughness for operational durability. These processes are essential for refining the microstructure and adjusting mechanical properties such as hardness and wear resistance. Post-heat treatment, the materials undergo comprehensive laboratory testing, encompassing hardness testing, microstructure analysis, and wear testing to validate the effectiveness of the heat treatment processes and assess the suitability of the materials for tank track applications.This methodological approach ensures systematic evaluation and enhancement of HSLA steel properties through controlled heat treatments and rigorous laboratory testing, aiming to optimize material performance in demanding operational conditions.

3. RESULTS AND DISCUSSION

3.1 Chemical Composition Testing

The chemical composition of the high-strength low-alloy (HSLA) steel samples, obtained through the reverse material process following JIS G 511 standards and induction furnace casting, was meticulously analyzed. Table 1 summarizes the results of the chemical composition testing, showcasing the percentage composition of various key elements crucial for the heat treatment processes and overall material performance.The composition analysis reveals significant levels of carbon (C), manganese (Mn), chromium (Cr), silicon (Si), phosphorus (P), sulfur (S), copper (Cu), nickel (Ni), molybdenum (Mo), and predominantly iron (Fe) as the base element (Table 1). These elements are strategically alloyed to impart specific mechanical properties, such as strength, toughness, and corrosion resistance, essential for the intended application in tank track components.

The observed chemical composition aligns with targeted specifications for HSLA steel, ensuring optimal properties required for heat treatment processes. Carbon content influences hardness and strength, while manganese contributes to toughness and hardenability during quenching. Chromium enhances corrosion resistance and hardenability, crucial for maintaining structural integrity under harsh operational conditions. Silicon improves strength and elasticity, while phosphorus and sulfur levels are controlled to enhance machinability and reduce brittleness.The results underscore the importance of precise alloying and casting processes in achieving desired material properties. Future studies will focus on correlating these compositions with mechanical testing results to further validate the effectiveness of the chosen alloy designs for enhancing the performance and durability of HSLA steel in military applications.

Table 1. Results of Chemical Composition Testing

Chemical Element	C	Mn	Cr	Si	P	S	Cu	Ni	Mo	Fe
Test Result (%)	0.34	0.79	0.969	0.486	0.011	0.022	0.035	0.045	0.328	Balance

3.2 Hardness Testing

Five compositions of hypo eutectoid steel underwent heat treatment processes. Heating was conducted at 860°C, reaching the A3 + 100°C temperature, where austenite phase (γ) is obtained. Heating at the austenite temperature aims to stabilize the phase uniformly as austenite (γ), ensuring comprehensive phase transformation. Following heating to 860°C, a holding time was applied to uniformly form austenite (γ), as the holding time aims to homogenize phases for predictable phase formation during cooling.

Cooling was achieved using oil as the medium, and the cooling medium significantly impacts hardness results. The hardness results for each composition are as follows: the highest average hardness of 43 HRC was achieved in the oil quenching process. The highest hardness average for as-cast material was 24 HRC. Normalizing yielded the highest average hardness of 29 HRC. Tempering at 400°C for 30 minutes resulted in the highest hardness data for composition number 5 at 26 HRC. Tempering at 400°C for 60 minutes showed composition number 4 with the highest hardness at 25 HRC. Tempering at 600°C for 30 minutes resulted in compositions number 4 and 5 achieving the highest hardness of 29 HRC

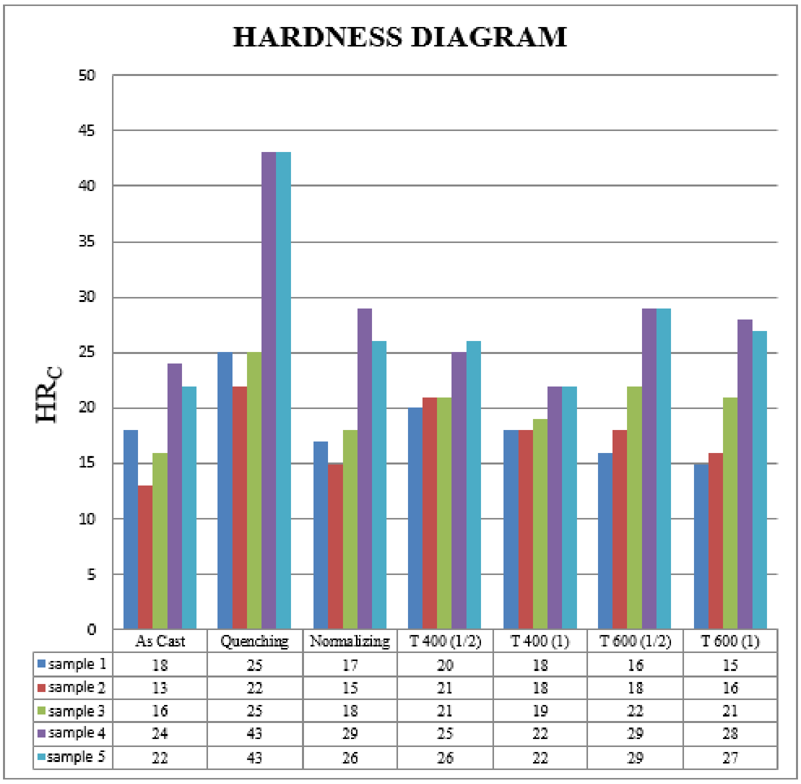

	As Cast	Quenching	Normalizing	T 400 (1/2)	T 400 (1)	T 600 (1/2)	T 600 (1)
sample 1	18	25	17	20	18	16	15
sample 2	13	22	15	21	18	18	16
sample 3	16	25	18	21	19	22	21
sample 4	24	43	29	25	22	29	28
sample 5	22	43	26	26	22	29	27

Figure 2. Hardness Data After Heat Treatment Process

These results highlight the critical role of tempering conditions in influencing the hardness characteristics of the material. Specifically, the tempering process at 600°C for 60 minutes effectively adjusted the hardness of sample 4 to approximate the desired hardness standard of 28 HRC seen in the imported tank tracklink (Figure 2.). This finding underscores the importance of precise heat treatment parameters in achieving optimal mechanical properties for tank components. Further research into the microstructural changes induced by varying tempering durations and temperatures could provide additional insights into enhancing the performance and durability of tank tracklinks

3.3 Metallographic Testing

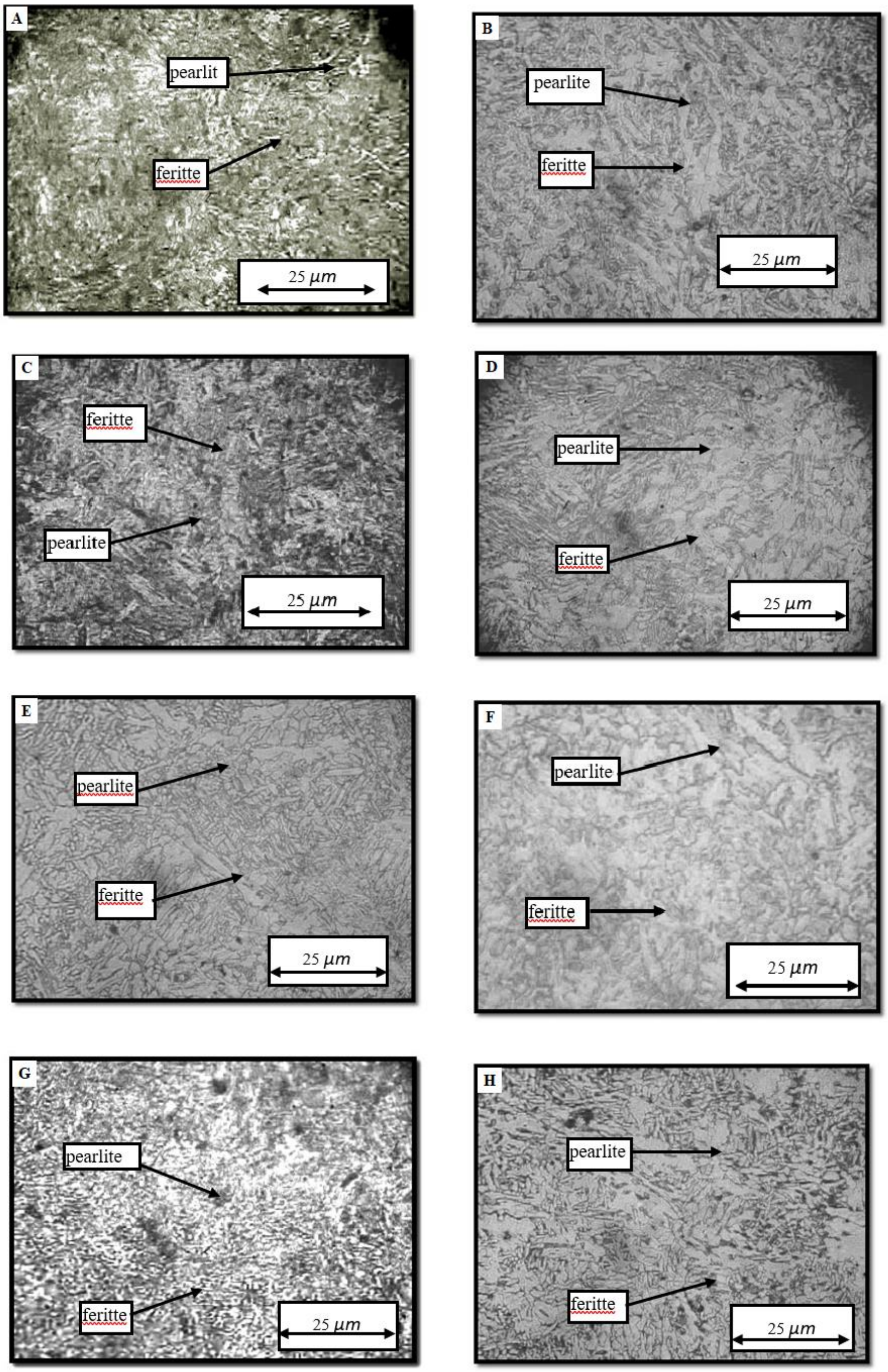

Figure 3. Microstructure with 3% nital etching and 400x magnification under the conditions: (a) as cast, hardness 24 HRC, (b) quenching, hardness 43 HRC, (c) tempering 400°C for 60 minutes, hardness 22 HRC, (d) normalizing, hardness 29 HRC, (e) tempering 400°C for 30 minutes, hardness 25 HRC, (f) tempering 600°C for 60 minutes, hardness 28 HRC, (g) normalizing with blower, hardness 31 HRC, (h) tempering 600°C for 30 minutes, hardness 29 HRC

Analysis of metallographic testing data across the five compositions confirms the presence of ferrite and pearlite phases in all material configurations, differing primarily in their matrix compositions and the granularity of their constituent grains. Materials characterized by a ferrite and pearlite matrix generally exhibit lower hardness values, a consequence of the soft nature inherent to ferrite. Hence, materials featuring a ferrite matrix typically demonstrate lower overall hardness. Conversely, materials featuring a pearlite matrix tend to manifest higher hardness values compared to their ferrite matrix counterparts, due to the inherent hardness of pearlite itself. Notably, materials with finer grain structures demonstrate superior strength characteristics, particularly evident in specimens subjected to the quenching process. This phenomenon is largely attributed to the elevated manganese content, which acts as a catalyst for pearlite formation, thereby promoting the development of finer rains during the pearlite transformation process.

4. CONCLUSION

From the results and discussions of this study, several conclusions can be drawn. Alloying elements play a crucial role in the physical and mechanical properties of HSLA (High Strength Low Alloy) steels, particularly Cr, Mo, C, Mn, Cu, and Ni. Therefore, it is necessary to conduct a composition test to confirm that the steel falls within the JIS G511 standard. The highest average hardness value of 29 HRC was obtained from samples subjected to normalizing, while the lowest average hardness value of 13 HRC was found in as-cast samples. Microstructural observations revealed martensitic and residual austenitic phases in as-cast specimens, whereas bainitic phases were observed after normalizing. Among the samples tested as potential materials for tank track links, sample number 4 showed the most promising hardness improvement trend.Metallographic analysis showed that specimens with the highest hardness values exhibited a pearlitic microstructure. Specimens with the lowest hardness values displayed a ferrite and pearlite matrix microstructure. Future research should focus on detailed microstructural analysis and mechanical testing to further optimize the performance and durability of HSLA steel in military applications.

5. ACKNOWLEDGEMENT

We extend our heartfelt gratitude to UNJANI for generously providing the laboratory facilities crucial for conducting the research presented in this paper. The state-of-the-art equipment and conducive research environment offered by UNJANI played a pivotal role in the meticulous analysis and experimentation conducted throughout this study. Without their support, this research would not have been possible. We also acknowledge Widyatama University for their invaluable financial support, which enabled the realization of this project. Their funding assistance facilitated the acquisition of materials, data analysis, and dissemination of findings, contributing significantly to the advancement of knowledge in this field. We are sincerely grateful for their commitment to academic excellence and research advancement

6. REFERENCES

[1] Olorundaisi, E., T. Jamiru, and A. T. Adegbola. "Mitigating the effect of corrosion and wear in the application of high strength low alloy steels (HSLA) in the petrochemical transportation industry—A review." Materials Research Express 6.12, 1265k9. 2020.
[2] Liang, Guo Fang. "Novel approaches to improve the mechanical properties of a high-strength low-alloy steel." 2023.
[3] Yucel, Berkay, Sezen Yucel, Arunim Ray, Lode Duprez, and Surya R. Kalidindi. "Mining the correlations between optical micrographs and mechanical properties of cold-rolled HSLA steels using machine learning approaches." Integrating Materials and Manufacturing Innovation 9, no. 3 : 240-256. 2020.
[4] Patterson, T., and J. C. Lippold. "Effect of niobium on the microstructure and properties of submerged arc welds in HSLA steel." Welding in the World 64, no. 6 (2020): 1089-1105.
[5] Ikpeseni, S. C. "Review of the applications, properties and processing parameters of dual phase steels." NIPES-Journal of Science and Technology Research 3, no. 2. 2021.
[6] Jorge, J. C. F., L. F. G. De Souza, M. C. Mendes, I. S. Bott, L. S. Araújo, V. R. Dos Santos, J. M. A. Rebello, and G. M. Evans. "Microstructure characterization and its relationship with impact toughness of C–Mn and high strength low alloy steel weld metals–a review." Journal of Materials research and technology 10 : 471-501. 2021.
[7] Schlegel, Joachim. "Alloying Elements and Steel Properties." In The World of Steel: On the History, Production and Use of a Basic Material, pp. 63-103. Wiesbaden: Springer Fachmedien Wiesbaden, 2023.
[8] Raabe, Dierk. "The materials science behind sustainable metals and alloys." Chemical reviews 123, no. 5 : 2436-2608. 2023.
[9] Vairamani, V., N. Mohan, S. K. Karthikeyan, and M. Sakthivel. "Optimization and microstructure analysis of Corten steel joint in mag welding by post heat treatment." Materials Today: Proceedings 21 : 673-680. 2020.
[10] Zavdoveev, Anatoliy, Valeriy Poznyakov, Thierry Baudin, Massimo Rogante, Hyoung Seop Kim, Mark

Heaton, Yuriy Demchenko, Victor Zhukov, and Mykola Skoryk. "Effect of heat treatment on the mechanical properties and microstructure of HSLA steels processed by various technologies." Materials Today Communications 28 : 102598. 2021.

[11] Cheng, Hailong, Xinchun Luo, and Xin Wu. "Recent research progress on additive manufacturing of high-strength low-alloy steels: Focusing on the processing parameters, microstructures and properties." Materials Today Communications : 106616. 2023.

[12] Samvatsar, Kaustubh, and Vandana Rao. "Corrosion aspects of Ni–Cu alloy (UNS N04400) and its surface improvement: A review." Emergent Materials 4, no. 6 : 1785-1801. 2021.

[13] Shozib, Imtiaz Ahmed, Azlan Ahmad, Ahmad Majdi Abdul-Rani, Mohammadali Beheshti, and Abdul’Azeez Abdu Aliyu. "A review on the corrosion resistance of electroless Ni-P based composite coatings and electrochemical corrosion testing methods." Corrosion Reviews 40, no. 1 : 1-37. 2022.

[14] Kimura, Yuuji, and Tadanobu Inoue. "Mechanical property of ultrafine elongated grain structure steel processed by warm tempforming and its application to ultra-high-strength bolt." ISIJ International 60, no. 6 : 1108-1126. 2020.

[15] Frómeta, D., Antoni Lara, Laura Grifé, Thomas Dieudonné, Pascal Dietsch, Johannes Rehrl, Clemens Suppan, Daniel Casellas, and J. Calvo. "Fracture resistance of advanced high-strength steel sheets for automotive applications." Metallurgical and materials transactions A 52 : 840-856. 2021

[16] Wang, Xin. "Integrated Computational Materials Design for Alloy Additive Manufacturing: Introducing Data-Driven Approach to Physical Metallurgy." PhD diss., University of Pittsburgh, 2023.

[17] Tan, Chaolin, Fei Weng, Shang Sui, Youxiang Chew, and Guijun Bi. "Progress and perspectives in laser additive manufacturing of key aeroengine materials." International Journal of Machine Tools and Manufacture 170 : 103804. 2021.

[18] Raabe, Dierk, Matic Jovičević-Klug, Dirk Ponge, Alexander Gramlich, Alisson Kwiatkowski da Silva, A. Nicholas Grundy, Hauke Springer, Isnaldi Souza Filho, and Yan Ma. "Circular Steel for Fast Decarbonization: Thermodynamics, Kinetics, and Microstructure Behind Upcycling Scrap into High-Performance Sheet Steel." Annual Review of Materials Research 54. 2024.

[19] Marivani, Parisa. "Investigation and comparison of S700E steel grade weldability in shipbuilding: numerical analysis on S700E steel grade." 2024.

LOGIC
Journal of Engineering Design and Technology
Vol. 24 No.2 July 2024 ; p. 93 - 100

p-ISSN : 1412-114X
e-ISSN : 2580-5649
http://ojs2.pnb.ac.id/index.php/LOGIC

APPLICATION OF MODE SHAPE DATA BASE INDICATOR (MSDBI) FOR DAMAGE DETECTION OF STEEL FRAME BRIDGE STRUCTURE BASED ON MODAL ASSURANCE CRITERION (MAC)

1) Civil Engineering Department, Parahyangan Catholic University, Bandung, West Jawa, Indonesia

Correponding email [1] :
8102001009@student.unpar.ac.id

Prima Adhiyasa [1]

Abstract. The substantial expansion of the global economy and the extensive urbanization witnessed in recent decades have rendered bridge infrastructure as a vital component of transportation systems. Conducting structural damage detection is a vital strategy to prevent structural failures and avert bridge collapse. One popular approach for detecting damage is to use mode shapes as characteristics in structural dynamics analysis. In this study, the identification of the mode shapes in the damaged condition will utilize the Modal Assurance Criterion (MAC), while the location of the damage within the simulation will be identified using the Mode Shape Data Base Indicator (MSDBI). The study was carried out with the help of a finite element model using Midas Civil software with a case study of a steel frame bridge. Referring to the report studied, damage identification focused on damage caused by loose bolts. The results of the analysis show that the MAC analysis has consistent values on mode shapes in each damage simulation with the mode shapes produced by the healthy condition model. Meanwhile, damage location is detected by the MSDBI index value in each damage simulation. It can be seen that the MSDBI index changes according to the location of the damage
.

Keywords : Damage detection, steel bridge, MAC, MSDBI.

1. INTRODUCTION

The substantial expansion of the global economy and extensive urbanization in recent decades have rendered bridge infrastructure as a vital component of infrastructure aspect. Damaged or inadequate performance of bridges, leading to potential collapses, presents significant challenges within infrastructure networks and results in measurable losses [1], [2]. A significant portion of bridges in Japan, approximately 9%, have reached the end of their designed lifespan. Projections indicate that this percentage will rise up to 53% within the next 20 years, as most bridges were constructed following World War II [3], [4], [5]. It is estimated that around 5,000 bridges in the United States require some of restorative work, such as repairs, reinforcements, or complete replacements, on an annual basis to maintain their structural integrity and functionality [5]. The failure of the Kutai Kartanegara bridge in 2011 emphasized the critical need for routine inspections of infrastructure to mitigate the risk of structural collapses [6]. Conducting bridge structural damage detection has become important to identify and to prevent structural failures. Furthermore, identified damage on bridge also necessary to repair the bridge and to maintain bridges in good condition to become a reliable infrastructure to support rapid economic growth. However, due to financial limitations, bridge replacement is often not a feasible solution [3], [7], [8].

One popular approach for detecting damage is to use mode shapes as characteristics in structural dynamics. Conceptually, damage modifies the mechanical characteristics of a bridge, including stiffness and mass, resulting in alterations to the dynamic response and damage detection method that utilizes mode shapes is the Modal Assurance Criterion (MAC) [9] [10]. MAC is a scalar value that quantifies the consistency between two sets of modal data, enabling a direct comparison of mode shapes in healthy and damaged structural conditions. While this method cannot precisely identify the specific location of damage due to its insensitivity to minor changes in mode shapes; however, it can still serve as a valuable diagnostic tool, providing an overall indication of structural damage. The Mode Shape Data Base Indicator (MSDBI) is utilized to detect localized damage in bridge structures, with a simple beam structure as a case study [11]. MSDBI study findings demonstrate the sensitivity of this index to reductions in beam cross-sectional stiffness. Increases the index value correspond well with the locations of damage along the beam elements, providing reliable damage detection results [11].

The main objective in this study is to damage detection in steel bridges by comparing the mode shapes of the structure in both healthy and damaged conditions by creating a simulation model of damage due to loose bolts. The identification of the mode shapes in the damaged condition will be using Modal Assurance Criterion (MAC), while the location of the damage within the simulation will be identified by Mode Shape Data Base Indicator (MSDBI).

2. METHODS

The research method utilizes mode shapes as the one dynamic response characteristic of structure to detect the presence and location of damage. Changes in the observed mode shapes between before and after the occurrence of damage are analyzed as an indicator to identify structural damage. [11].

2.1. Modal Assurance Criterion (MAC)

MAC is a popular method that uses a comparison of two mode shapes in the identification of damage to bridges. MAC compares two mode shapes such as mode shapes with different conditions. In this study, a mode shapes of healthy and damaged conditions were used from the analysis results. The value of MAC is a scalar value limited between zero and one, representing a linear relationship between two mode shape data sets [12]. In practice, MAC serves to assess the identification of variance conducted or to approximate the results from testing different variances. The MAC value is calculated based on two data of mode shape vectors using Equation (1) [13].

$$\mathrm{MAC}(r,q)=\frac{\left|\{\phi_A\}_r^T\{\phi_X\}_q\right|^2}{\left(\{\phi_A\}_r^T\{\phi_A\}_r\right)\left(\{\phi_X\}_q^T\{\phi_X\}_q\right)} \tag{1}$$

Where $\{\phi_X\}_q$ is mode shape vector healthy condition, mode q, $\{\phi_A\}_r$ is mode shape vector damage condition, mode r, $\{\phi_X\}_q^T$ is transpose of $\{\phi_X\}_q$, and $\{\phi_A\}_r^T$ is transpose of $\{\phi_A\}_r$.

MAC is primarily employed to evaluate the consistency among mode shape vectors, rather than to assess their validity or orthogonality [14]. However, the MAC has notable limitations in its ability to identify potential issues, as it cannot effectively capture the presence of consistent random or systematic errors across the variance estimation vectors. [13]. In addition, MAC is unable to distinguish between systematic errors and localized differences. This limitation is often attributable to the underlying assumptions or estimation techniques used for the variance parameters being invalid. Furthermore, MAC may be susceptible to the effects of measurement uncertainty, which can impact its reliability and usefulness [15]. Consequently, MAC is frequently utilized as a preliminary check prior to further analysis and only to identify which mode shape have consistent value of healthy condition or close to a value of one.

2.2. Mode Shape Data Based Indicator (MSDBI)

The MSDBI will be use to detects structural damage by analyzing changes in the mode shape data before and after the occurrence of damage in curvature plot. MSDBI utilizes the first and second derivatives from two mode shape data sets to identify the presence and location of structural damage. [11]. Equation (2) represents the modal data extracted from the structural model, which includes the nodal coordinates and mode shapes.

$$\left[x_{q,}\Phi_{(q,i)}=\left[x_{q,}\Phi_{(1,i)},x_{q,}\Phi_{(2,i)},\dots,x_{q,}\Phi_{(n+1,i)}\right]\right] \tag{2}$$

Where nodal coordinates, $x_{q,}\ q=1,2,\dots,n+1$ and mode shapes, $\Phi_{(q,i)},q=1,2,\dots,n+1$. The first and second derivatives of equation (2) are approximated using Equation (3) and Equation (4).

$$\boldsymbol{\Phi'_{q,i}=\frac{\Phi_{q+1,i}-\Phi_{q-1,i}}{2l_e}} \tag{3}$$

$$\boldsymbol{\Phi''_{q,i}=\frac{\Phi_{q-1,i}-2\Phi_{q,i}+\Phi_{q+1,i}}{l_e^2}} \tag{4}$$

Where $\Phi_{q,i}$ is mode shape of the qth node in the ith mode shape and l_e is constant distance separating two consecutive nodes. From Equations (3) and (4) the MSDBI value is obtained using the Equation (5).

$$\mathbf{MSDBI_q} = \frac{\sum_{i=1}^{nm}\left|\left[\left|\boldsymbol{\Phi}''_{d(q,i)} - \boldsymbol{\Phi}''_{h(q,i)}\right| \times \left(\boldsymbol{\Phi}_{d(q,i)}\right)^2\right] - \left[\left(\left|\boldsymbol{\Phi}'_{d(q,i)}\right| - \left|\boldsymbol{\Phi}'_{h(q,i)}\right|\right)^2 \times \boldsymbol{\Phi}_{h(q,i)}\right]\right|}{\mathbf{nm}} \tag{5}$$

Where $\Phi_{h(q,i)}$ is mode shape of healthy condition, $\Phi_{d(q,i)}$ is mode shape of damage condition and nm is number of mode shapes. With the assumption that MSDBI values are obtained from all nodal from the model, $\left(\mathrm{MSDBI_q}, q = 1,2, \ldots, n+1\right)$ which represents a normally distributed sample, then the MSDBI form can be normalized as in equation (6).

$$\mathbf{nMSDBI_q} = \mathbf{max}\left[\mathbf{0}, \left(\frac{\mathbf{MSDBI_q - mean\ (MSDBI)}}{\mathbf{std\ (MSDBI)}}\right)\right] \tag{6}$$

Where, $\mathrm{MSDBI_q}$ is defined by Equation (5), mean (MSDBI) and std (MSDBI) is mean and standard deviation of MSDBI.

2.3. Case Study

The case study will be remodel of the existing steel frame bridge structure, with data sourced from laporan Uji Respons 1 Jembatan Citarum issued by Pusat Litbang Jalan dan Jembatan (PUSJATAN). The case study is conducted through modeling using the Midas Civil software as shown in Figure 1.

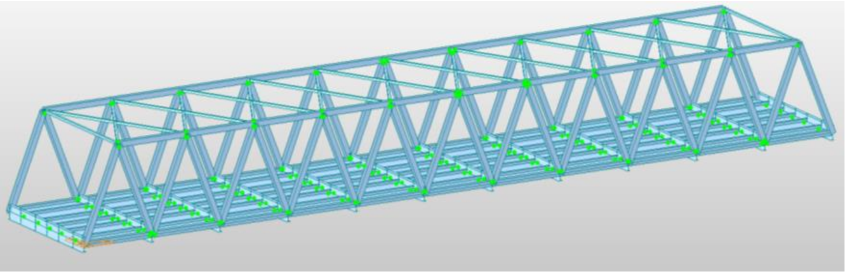

Figure 1. Steel bridge Structural Modeling in 3 Dimensions

The identified damage of the steel frame bridge structure is due to loose bolts, which reduce the stiffness of the steel bridge connections. The location for loose bolts connections to be considered are the downstream direction at upper and bottom chord sections as shown in Figure 2.

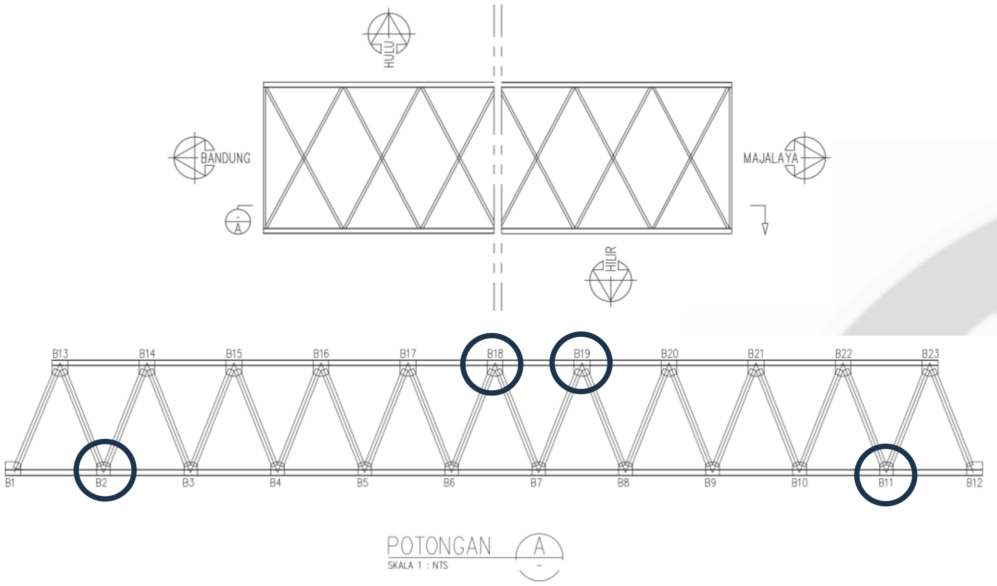

Figure 2. Location of loose bolts at downstream direction

From Figure 2, the locations of loose bolts are at bolt node (B), B2, B11, B18, and B19 in downstream and upstream directions. The percentconsage value of tight bolts included in the model is the smallest percentage value. Imperfections in bolt installation on the diagonal elements in this study are not modeled and some part of steel structural element in upper and bottom chord sections will designed as frame. The percentage of loose bolts in upstream and downstream directions is presented in Table 1. The damage that occurs at nodal points in bridge connections is characterized by a reduction in axial stiffness in the Z direction and lateral stiffness in the X direction, with the smallest percentage value identified. A simulation of the damage was conducted to obtain the mode shape data of damaged condition, which are presented in the Table 2.

Table 1. Percentage of stiffness reduction

Downstream direction				
Node	B2	B11	B18	B19
Number of loose bolts/total bolts	3/10	2/20	8/20	12/20
Percent reduction (%)	70%	90%	60%	40%
Upstream direction				
Node	B2	B11	B18	B19
Number of loose bolts/total bolts	-	-	6/20	9/20
Percent reduction (%)	-	-	70%	55%

Table 2. Damage Simulation

Simulation	Damage description
Healthy	Healthy condition
Damage 1	B2 and B11 at downstream direction
Damage 2	B18 and B19 at downstream direction
Damage 3	B18 and B19 at upstream direction
Damage 4	B2, B11, B18 and B19 at downstream direction
Damage 5	B2 and B11 at downstream position; B18 and B19 at upstream direction
Damage 6	B2 and B11 at downstream direction; B18 and B19 at downstream and upstream direction

3. RESULTS AND DISCUSSION

The output from the model are natural frequencies and mode shapes, within Figure 3 illustrate the mode shape from mode 1 to mode 3. Table 3 presents the mode shapes data for healthy condition.

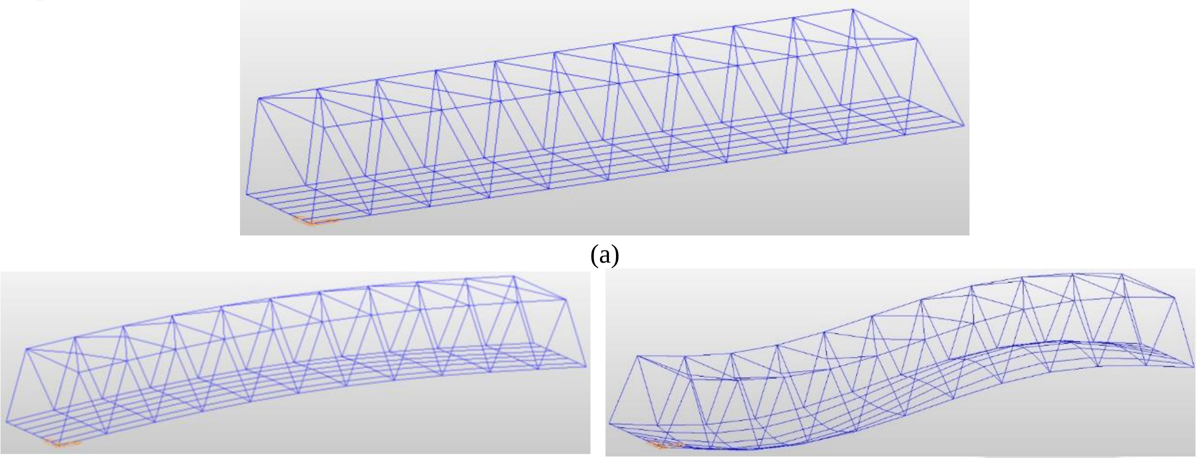
(a)
(b)
(c)

Figure 3. Bridge Structure on (a) Mode shape 1; (b) Mode shape 2; (c) Mode shape 3

Table 3. Natural frequency and mode shape healthy condition

Mode Shapes	Direction	Frequency (Hertz)
1	Y Dir.	1.427863
2	Z Dir.	2.020688
3	Z Dir.	2.783113

3.1. MAC Analysis

The condition of the bridge is assessed using equation (1) to obtain data on damage based on the MAC method by analyzing the mode shape of the bridge structure. The analysis results can determine the MAC value for each simulation on Table 4.

Table 4 MAC Analysis for All Damage Simulation

Simulation	X Dir.		Y Dir.		Z Dir.	
	Mode	Value	Mode	Value	Mode	Value
Damage 1	1	0.997	1	0.887	2	0.585
Damage 2	1	0.783	1	0.888	2	0.725
Damage 3	1	0.806	1	0.888	2	0.562
Damage 4	1	0.776	1	0.888	2	0.725
Damage 5	1	0.803	1	0.888	2	0.562
Damage 6	1	0.943	1	0.888	2	0.589

From Table 4 it is observed that mode shape 1 have consistent values or close to 1 in Damage 1 to Damage 6 simulations under the healthy condition of the bridge structure in both the X and Y directions. The MAC analysis in the Z direction indicates that mode shape 2 is closest to a healthy condition. Damage 2 and Damage 4 simulations share the same MAC value of 0.725, reflecting similar damage characteristics. Similarly, Damage 3 and Damage 5 simulations also have identical MAC values due to comparable damage patterns. The values for Damage 1 and Damage 6 simulations are also similar, as both involve damage to the bottom chord section.

3.2. MSDBI Analysis

Detecting bridge structural damage of MSDBI relies on the mode shape values of the bridge structure from the damaged simulation, with the mode shape analyzed through the dominant modes produced by the MAC method. In Damage 1 Simulation, the MSDBI graph indicates an increase in MSDBI values on both the left and right sides where the damage location are, as shown in Figure 4. The MSDBI values are also present at the nodes that experienced damage, consistent with the assumptions in the simulation and across all examined directions.

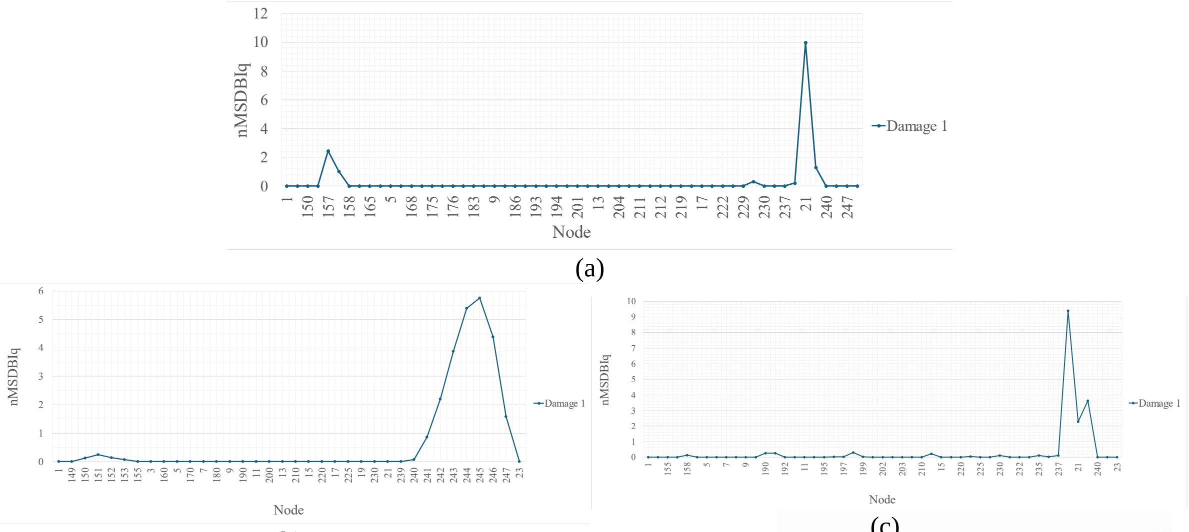

(a)

(b)

(c)

Figure 4. MSDBI Damage 1 simulation at (a) X direction; (b) Y direction; (c) Z direction

A comparison Damage 2 and Damage 3 simulations resulted in damage occurring in the middle of the span and having a tendency graph with a sharp shape in the middle of the span indicating that the damage occurred in the middle. However, Damage 3 displays more damage index than Damage 2 that lead to the MSDBI curve has numerous values along upstream direction. In Z direction, simulation 2 shows a sharp graphical trend at the mid-span, while simulation 3 has a fluctuating pattern. The differences in these damage patterns indicate that the shape of the curve varies depending on the downstream direction which is presented in Figure 5.

Damage 2 and Damage 4 simulations show a similar damage pattern in the X direction, much like the comparison Damage 2 and Damage 3 simulations. The Y direction also has the same pattern where the MSDBI value makes the damage graph in the middle of the span. Likewise, in the Z direction, the damage value has similar values in both simulations as in the curve in Figure 6.

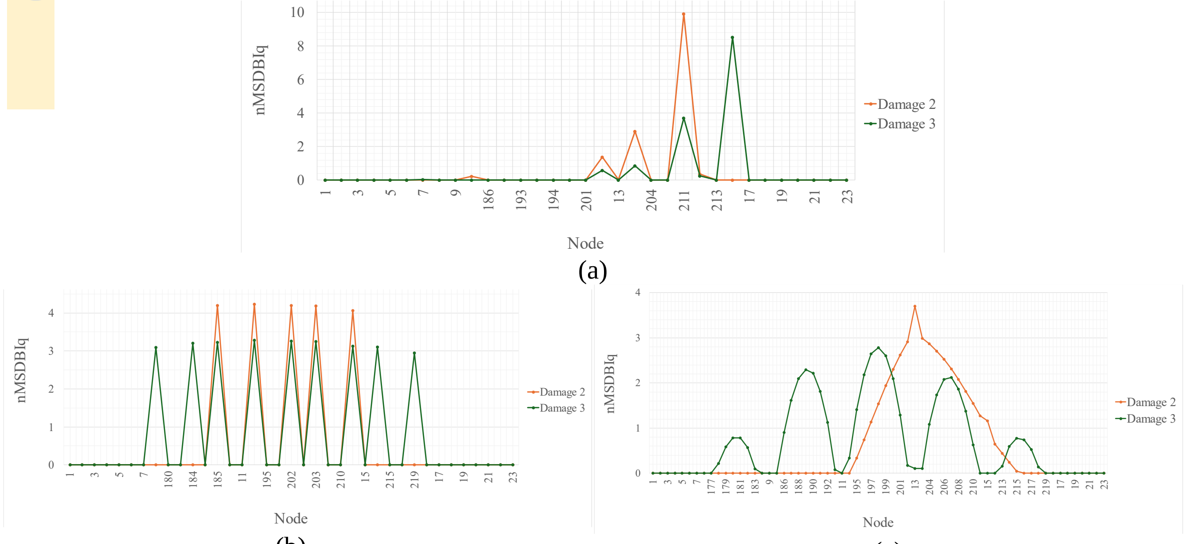

(a)

(b)

(c)

Figure 5. Comparison of MSDBI Damage 2 and Damage 3 simulations at (a) X direction; (b) Y direction; (c) Z direction

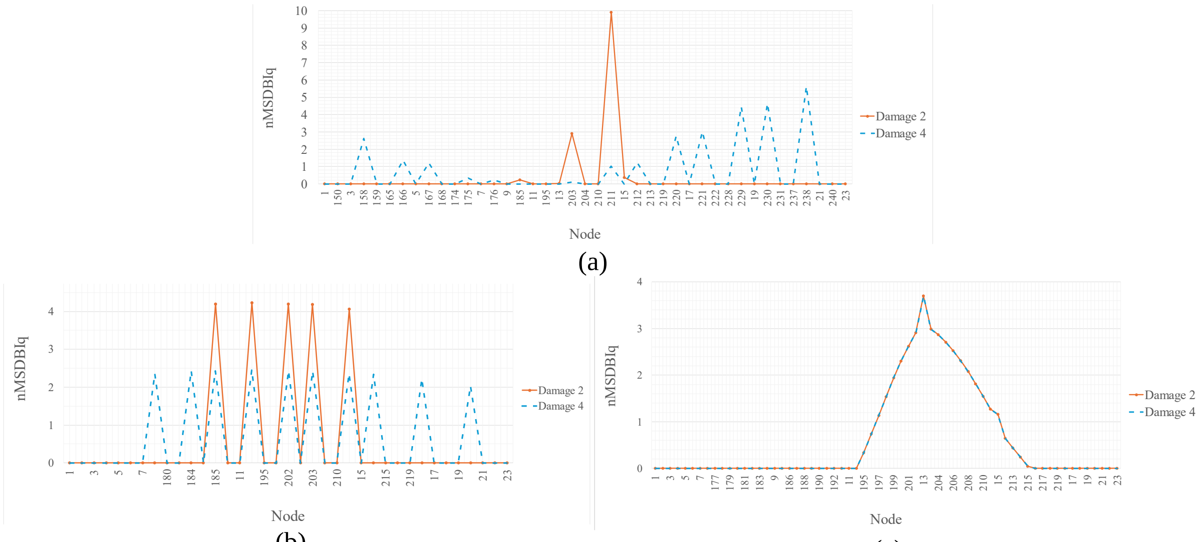

(a)

(b)

(c)

Figure 6. Comparison of MSDBI Damage 2 and Damage 4 simulations at (a) X direction; (b) Y direction; (c) Z direction

The comparison of the Damage 3 and Damage 5 simulations also has the same pattern as in the comparison of Damage 2 and Damage 4 simulations where the MSDBI index value shows an increase at the node simulated damage that illustrated in Figure 7. The key difference between the comparison Damage 3 and Damage 5 simulations and comparison Damage 2 and Damage 4 simulations, is the shape of the curve in the Z direction, as comparison Damage 3 and Damage 5 simulations are assessed in upstream direction.

Figure 8 shows a similar graphic shape in the Damage 4, 5 and 6 simulations in the X direction simulations where the graphs of all three simulations have the same pattern. This indicates that the damage on the left and right sides is more dominant compared to the damage in the center. Comparison in Y direction also reveals a similar MSDBI graph shape across the three simulations, as well as in the previously described in MAC analysis, where the MAC values for all three simulations are the same at 0.888, making the Y direction graphs tends to be similar. In the Z direction, it is observed that the graph for simulation Damage 6 takes the shape of the two previous simulations, leading to the conclusion that simulation Damage 6 is a combination of the graph from the two prior simulations and has the highest MSDBI value among the three simulations.

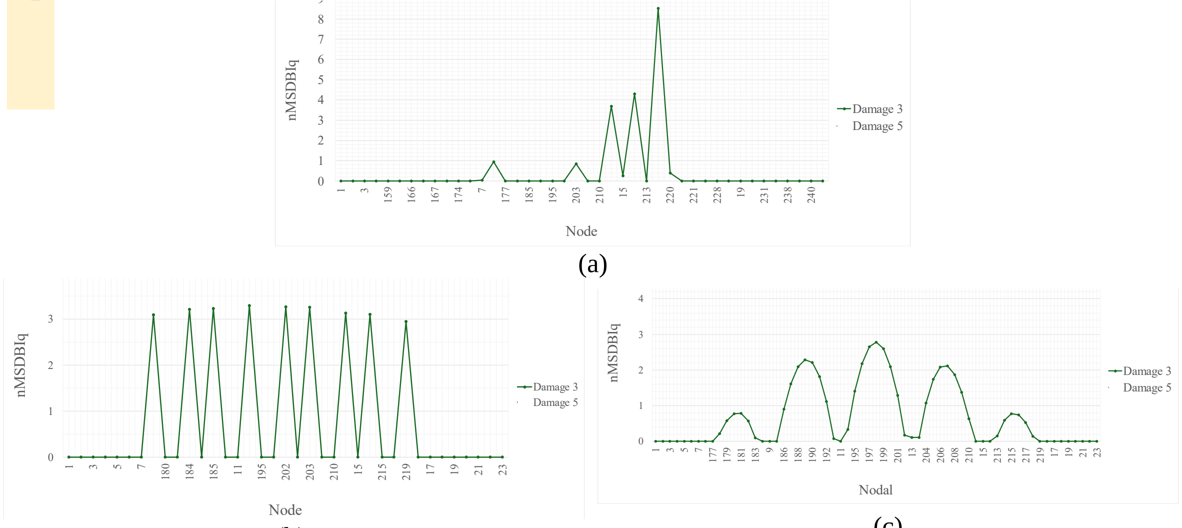

(a)

(b)

(c)

Figure 7. Comparison of MSDBI Damage 3 and Damage 5 simulations at (a) X direction; (b) Y direction; (c) Z direction

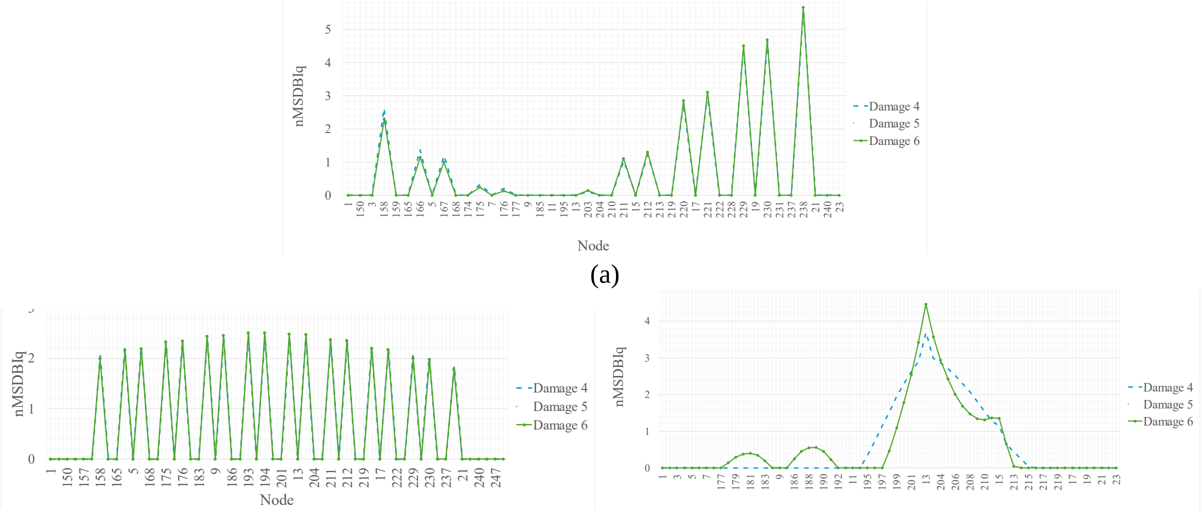

(a)

(b)

(c)

Figure 8. Comparison of MSDBI Damage 4, Damage 5 and Damage 6 simulations at (a) X direction; (b) Y direction; (c) Z direction

From the results obtained, MAC analysis can determine the mode shapes in damage conditions that are close to healthy conditions more accurately. With MAC analysis, it is hoped that the data of mode shapes from test result in the field can be faster to identifying a consistent mode shapes that will be used for the next analysis. From the results of the MSDBI analysis, it was found that the MSDBI analysis could provide a damage curve that was in accordance with the simulated damage with a consistent mode shape from MAC analysis so that the location of the damage could be known more quickly in the test field.

4. CONCLUSION

Based on the analysis and comparison of the two previous methods, several conclusions were obtained as follows:

1. The Modal Assurance Criterion analysis indicates that the dominant modes correspond to the healthy condition, which are mode 1 in the Y direction and mode 2 in the Z direction. The MAC results in the Y direction are the most consistent, with values around 0.88 or 0.9, suggesting a strong correlation throughout the damage simulation. Simulations with similar damage locations exhibit comparable MAC values in each direction, such as Damage 2 and Damage 4, as well as Damage 3 and Damage 5, where the simulations with greater damage have slightly smaller MAC values.
2. The comparison of the MSDBI curves indicates that the MSDBI curve in the X direction exhibits a shape consistent with the specified damage locations across the simulations. However, the upstream direction of the

curve shows greater curvature than the downstream side, as evidenced by the alignment of the MSDBI values with the designated damage points, such as in the comparison of Damage 2 and Damage 4 simulations. The MSDBI curve in the Y direction also corresponds to the specified damage location, displaying a sharper curve but with a more distinct pattern compared to the X direction across all simulations. The MSDBI curve pattern in the Z direction varies between directions, with sharp curvatures observed in the downstream direction for Damage 1, Damage 2, and Damage 4 simulations, while the upstream direction exhibits a fluctuating curve, as seen in simulations 3 and 5. In simulation 6, a combination of curves from Damage 4 and Damage 5 is observed, which corresponds with the assumption that damage occurs on both sides.

3. Identifying the mode shapes from damage condition will more accurately using MAC analysis and the results of the MSDBI analysis for each damage simulation show a change in the curve value according to the damage simulation, which conlcude that the MSDBI analysis can identify the location of damage more accurately.

5. ACKNOWLEDGEMENT

The author would like to thank the Civil Engineering Department of Parahyangan Catholic University and PT Midasindo Teknik Utama for support of MIDAS CIVIL software steel bridge modeling.

6. REFERENCES

[1] Y. Xu and Y. Xia, “Structural Health Monitoring of Long-Span Suspension Bridges,” 2012.

[2] Liang Wang and T.H.T. Chan, “Review of vibration-based damage detection and condition assessment of bridge structures using structural health monitoring,” Proceedings of The Second Infrastructure Theme Postgraduate Conference: Rethinking Sustainable Development - Planning, Infrastructure Engineering, Design and Managing Urban Infrastructure., pp. 35–47, 2009.

[3] K. C. Chang and C. W. Kim, “Modal-parameter identification and vibration-based damage detection of a damaged steel truss bridge,” Eng Struct, vol. 122, pp. 156–173, Sep. 2016, doi: 10.1016/j.engstruct.2016.04.057.

[4] P. L. Shrive, “Evaluating GFRP and SHM in the Centre Street Bridge Project,” Library and Archives Canada = Bibliothèque et Archives Canada, 2005.

[5] Yufeng. Wang, Vibration-based damage detection on a multi-girder bridge superstructure. Library and Archives Canada = Bibliothèque et Archives Canada, 2013.

[6] A. A. Pramudya, A. Wibowo, and A. Soekiman, “Tren, Biaya, Dan Tantangan Structural Health Monitoring Jembatan,” 2022.

[7] P. C. Chang, A. Flatau, and S. C. Liu, “Review paper: Health monitoring of civil infrastructure,” 2003, SAGE Publications Ltd. doi: 10.1177/1475921703036169.

[8] B. T. Svendsen, G. T. Frøseth, O. Øiseth, and A. Rønnquist, “A data-based structural health monitoring approach for damage detection in steel bridges using experimental data,” J Civ Struct Health Monit, vol. 12, no. 1, pp. 101–115, Feb. 2022, doi: 10.1007/s13349-021-00530-8.

[9] J. R. Casas and F. Rodrigues, “Bridge Condition and Safety Based On Measured Vibration Level,” 2015.

[10] C. R. Farrar and K. Worden, “An introduction to structural health monitoring,” Philosophical Transactions of the Royal Society A: Mathematical, Physical and Engineering Sciences, vol. 365, no. 1851, pp. 303–315, Feb. 2007, doi: 10.1098/rsta.2006.1928.

[11] O. Yazdanpanah, S. M. Seyedpoor, and H. Akbarzadeh Bengar, “A new damage detection indicator for beams based on mode shape data,” Structural Engineering and Mechanics, vol. 53, no. 4, pp. 725–744, Feb. 2015, doi: 10.12989/sem.2015.53.4.725.

[12] R. J. Allemang, “The Modal Assurance Criterion – Twenty Years of Use and Abuse,” Sound and vibration, vol. 37, no. 8, pp. 14–23, 2003.

[13] M. Pastor, M. Binda, and T. Harčarik, “Modal assurance criterion,” in Procedia Engineering, Elsevier Ltd, 2012, pp. 543–548. doi: 10.1016/j.proeng.2012.09.551.

[14] Pranjal Makarand Vinze, Y. Feng Xu, and A. W. Phillips, “Developing a correlation criterion (spaceMAC) for repeated and pseudo-repeated modes,” 2014.

[15] S. Gres et al., “Variance computation of the Modal Assurance Criterion,” 2018. [Online]. Available: https://inria.hal.science/hal-01886642